Development and evaluation of targeted therapies for glioblastomas treatment

Dissertation

Presented in Partial Fulfillment of the Requirements for the Degree Doctor of Philosophy in the Graduate School of The Ohio State University

By

Kai Chen

Graduate Program in Biomedical Science

The Ohio State University

2024

Dissertation Committee

Xiaoguang “Margaret” Liu, Advisor

Amanda Toland, Committee Member

Xun Ai, Committee Member

Daniel Gallego-Perez, Committee Member

Abstract

Glioblastomas (GBM), constituting around 50% of gliomas, represent the most aggressive and malignant form of brain tumors, characterized by significant heterogeneity. Owing to intrinsic factors such as stem-like cells, the blood-brain barrier (BBB), and hypoxia, GBMs often exhibit resistance to standard treatment modalities including surgery, chemotherapy, and radiation therapy, leading to frequent recurrence. This dissertation describes our work aimed to develop, produce, and assess novel targeted therapies for GBM treatment. Specifically, we focused on the potent natural compound verrucarin A (Ver-A) in conjunction with monoclonal antibody-directed extracellular vesicles (mAb-EV) and the employment of therapeutic genes targeting cancer mitochondria delivered *via* adeno-associated virus (AAV). In the first phase, mAb-EV-Ver-A was engineered by encapsulating Ver-A and attaching anti-EGFR mAb onto EV derived from HEK293F culture. Utilizing advanced imaging techniques, including confocal microscopy and the In Vivo Imaging System (IVIS), we demonstrated the ability of mAb-EV to penetrate the BBB, localize to intracranial glioblastoma xenografts, and deliver drugs intracellularly. *In vitro* cytotoxicity studies revealed promising IC_{50} values for Ver-A ranging from 2 to 12 nM. Tolerated dose studies indicated minimal systemic toxicity associated with mAb-EV-Ver-A. Subsequent *in vivo* anti-tumor efficacy assessments in intracranial xenograft models highlighted the inhibitory effects of EGFR mAb-EV-Ver-A on glioblastoma growth, emphasizing the potential of mAb-EV as a drug delivery platform and the

therapeutic promise of natural Ver-A. In the second phase, recognizing the therapeutic potential of targeting cancer cell mitochondria, we developed and evaluated mLumiOpto, a novel mitochondrial-targeted luminoptogenetics gene therapy. mLumiOpto was designed to disrupt the inner mitochondrial membrane (IMM) potential and induce cancer cell death. This involved synthesizing a blue light-gated channelrhodopsin (CoChR) within the IMM and co-expressing a blue bioluminescence-emitting Nanoluciferase (NLuc) in the cytosol of the same cells. Selective delivery of mLumiOpto genes to cancer cells *in vivo* was achieved using AAV carrying a cancer-specific c-fos promoter. A robust AAV production process was developed and optimized, along with a purification protocol to enhance recovery rates. Activation with NLuc luciferin elicited robust endogenous bioluminescence, activating mitochondrial CoChR and leading to cancer cell IMM permeability disruption, mitochondrial damage, and subsequent cell death. Importantly, mLumiOpto demonstrated significant efficacy in reducing tumor burden and killing if not eliminating tumor cells in glioblastomas xenograft models, establishing it as a promising therapeutic strategy for targeting cancer cell mitochondria *in vivo*. In summary, this study showcases the development of innovative therapeutic approaches for glioblastoma treatment, highlighting the efficacy of monoclonal antibody-directed extracellular vesicles encapsulating verrucarin A and the promising potential of mitochondrial-targeted luminoptogenetics gene therapy in preclinical models.

Dedication

This dissertation is dedicated to my parents, whose boundless encouragement and steadfast support have been the cornerstone of this achievement.

Acknowledgments

I would like to express my deepest gratitude to my advisors, Dr. Xiaoguang Liu and Dr. Lufang Zhou, for their invaluable guidance, unwavering support, and insightful feedback throughout the entire process of this dissertation. Their expertise, encouragement, and patience have played an indispensable role in finishing this work.

I also would like to thank my committee members, Dr. Amanda Toland, Dr. Xun Ai and Dr. Daniel Gallego-Perez for their valuable insights and constructive criticism, which have significantly enriched the quality of this research.

I am thankful for all former and current laboratory members who have assisted me in my research including Dr. Patrick Ernst, Dr. Yingnan Si, Dr. Seulhee Kim, Zhuoxin Zhou, Jia-Shiung Guan, Taehyun Kim, Siying Yang, Tanvi Varadkar, Jiashuai Zhang and Hailey Baker.

This dissertation would not have been possible without the collective support and encouragement of all those mentioned above. I am truly grateful for everyone's help.

Finally, I want to thank The Ohio State University for providing me the opportunity to peruse Ph.D. in Biomedical Science Graduate Program.

Vita

2013-2017	B.S. Plant Quarantine, Shandong Agricultural University, China
2017-2019	M.S. Biotechnology, University of Alabama at Birmingham
2020-2024	Ph.D. The Ohio State University

Publications

1. **Chen K**, Ernst P, Kim S, Si Y, Varadkar T, Ringel M, Liu XM, Zhou L. An innovative mitochondria-targeted gene therapy for cancer treatment. 2024. *BioRxiv.* doi.org/10.1101/2024.03.24.584499.
2. **Chen K**, Kim S, Yang S, et al. Advanced biomanufacturing and evaluation of adeno-associated virus. *J Biol Eng.* 2024;18(1):15
3. **Chen K**, Si Y, Guan J-S, et al. Targeted extracellular vesicles delivered verrucarin A to treat glioblastoma. *Biomedicines.* 2022;10(1):130.
4. **Chen K**, Ernst P, Liu XM, Zhou L. Optogenetic Studies of Mitochondria. *Methods Mol Biol*. 2022; 2501:311-324.
5. **Chen K**, Si Y, Ou J, et al. Antibody–Drug Conjugate to Treat Meningiomas. *Pharmaceuticals.* 2021;14(5):427.

6. Zhang J, Zhou Z, **Chen K**, Kim S, Cho I, Varadkar T, Baker H, Co J, Zhou L, Liu XM*. A CD276-targeted antibody-drug conjugate to treat non-small lung cancer (NSCLC). *Cells (MDPI).* 12(9): 2393-2406. 2023.
7. Si Y, **Chen K**, Ngo HG, Guan JS, Totoro A, Zhou Z, Kim S, Kim T, Zhou L, Liu X. Targeted EV to Deliver Chemotherapy to Treat Triple-Negative Breast Cancers. *Pharmaceutics*. 2022; 14(1):146.
8. Guan J-S, **Chen K**, Si Y, et al. Process improvement of adeno-associated virus production. *Frontiers in chemical engineering.* 2022;4:1.
9. Si Y, Zhang Y, Guan JS, Ngo HG, Totoro A, Singh AP, **Chen K**, Xu Y, Yang ES, Zhou L, Liu R, Liu XM. Anti-CD47 monoclonal antibody-drug conjugate: a targeted therapy to treat triple-negative breast cancers. *Vaccines.* 2021. 9: 882-895.
10. Ernst P, **Chen K**, Tang Y, et al. Investigation into the difference in mitochondrial-cytosolic calcium coupling between adult cardiomyocyte and hiPSC-CM using a novel multifunctional genetic probe. *Pflugers Arch*. 2021;473(3):447-459.
11. Si Y, Zhang Y, Ngo HG, Guan JS, **Chen Kai**, Wang Q, Singh AP, Xu Y, Zhou L, Yang ES, Liu XM. Targeted liposomal chemotherapies to treat triple-negative breast cancer. *Cancers.* 2021. 13(15): 3749-3763.
12. Si Y, Guan J, Xu Y, **Chen K**, Kim S, Zhou L, Jaskula-Sztul R, Liu XM. Dual-targeted exosomes to facilitate combined therapies for neuroendocrine cancer treatment. *Pharmaceutics.* 2020. 12:1079-1091.
13. Si Y, Xu Y, Guan J, **Chen K**, Kim S, Yang E, Zhou L, Liu XM. Anti-EGFR Antibody-drug Conjugate for Triple Negative Breast Cancer Therapy. *Engineering in Life Sciences.*

14. Si Y, Kim S, Ou J, Lu Y, Ernst P, **Chen K**, Whitt J, Carter A, Bibb J, Markert J, Bibb J, Chen H, Zhou L, Jaskula-Sztul R, Liu XM. Anti-SSTR2 Antibody-drug Conjugate for Neuroendocrine Tumor Therapy. *Cancer Gene Therapy.* 2020. 28: 799-812.

Fields of Study

Major Field: Biomedical Science Graduate Program

Table of Contents

List of Tables

List of Figures

Chapter 1. Introduction

Glioblastomas (GBM)

Glioblastoma multiform (WHO grade IV) is the most prevalent and aggressive primary malignant brain tumor, accounting for approximately 50% of gliomas in adults [1,2]. The incidence of GBM is less than 10 in 100,000 persons, but the median survival of 14.6 months for GBM patients from time of diagnosis and the 2-year survival rate of 6.5% makes it a considerable public health issue [3]. Even though therapeutic agents against GBM have been developing for years, it remains a highly lethal disease with poor prognosis. Numerous treatments are under investigation, but few have been successful [4]. Over the years, the clinical treatment strategy for newly diagnosed GBM has been surgery followed by radiation therapy and temozolomide chemotherapy [4]. However, therapeutic resistance and GBM recurrence usually develop after conventional therapies due in part to pathways involving stem-like cells, the blood-brain barrier (BBB), and/or hypoxia [5,6]. Thus, developing new treatment strategies to extend the survival of GBM patients is critical.

Extracellular vesicles in drug delivery

Recent investigations have underscored the considerable potential of extracellular vesicles (EVs), intrinsic nanoscale entities within the body, for precise drug delivery. The use of EVs for therapy offer a range of benefits including immune system compatibility, sustained circulation, ability to traverse the BBB, and specific targeting of tumors via surface-

modified GBM-targeting agents [7,8]. Building upon our earlier work, we have established robust methodologies for the biomanufacturing of EVs and their surface modification [9]. Notably, we've validated their efficacy in delivering tailored combination therapies [10]. Additionally, our studies have substantiated the effectiveness of monoclonal antibodies (mAbs) *in vivo* [11-14] for tumor targeting, as well as their utility in guiding drug delivery systems such as liposomes and EVs to tumor sites [12]. Considering these findings, we have engineered mAb-EVs as a novel approach for delivering therapeutic payloads in the treatment of GBM.

Adeno-associated virus (AAV) in gene delivery

AAV-based gene therapy has been extensively investigated in both preclinical and clinical trials, displaying a robust safety profile and consistent therapeutic efficacy[15]. Over 130 AAV-delivered gene therapies have been evaluated in clinical trials during the last two decades, and hundreds of clinical trials are on-going for Alzheimer, Parkinson, and other diseases[16]. Furthermore, AAV-based gene therapy exhibits the capacity to efficiently transduce numerous cancer cells and cancer stromal cells. Moreover, it enables stable expression of diverse cancer therapeutic genes, including suicide genes, immunostimulatory genes, cytotoxic genes, small interference RNA (siRNA), and anti-angiogenesis genes[17,18]. These therapeutic genes collectively contribute to the inhibition of cancer formation and progression.

Mitochondrial-targeting gene therapy

To address the challenges in GBM treatment, the AAV mediated mitochondrial-targeting gene therapy (mLumiOpto) was developed. This technology holds significant promise as a novel strategy for the effective treatment of GBMs. Unlike traditional gene therapy approaches (e.g., *TP53,* miRNA), chemotherapy, and biotherapy, mLumiOpto directly targets the inner mitochondrial membrane potential to induce cell death in GBMs through the introduction of heterologous genes. This unique approach does not rely on subtype-specific endogenous proteins or signaling transduction pathways, which are often impaired in cancers treated with other therapies. As a result, mLumiOpto therapy exhibits reduced susceptibility to cancer resistance development and greater efficacy in treating heterogeneous GBMs.

In summary, this dissertation aims to develop, produce, and evaluate novel targeted therapies for the treatment of GBM, with a specific focus on monoclonal antibody-directed extracellular vesicles (mAb-EVs) and mitochondrial-targeting gene therapies. The subsequent chapters will detail the engineering and validation of mAb-EVs, the development of AAV-mediated mLumiOpto, and the comprehensive preclinical evaluations of these therapeutic approaches. Through these investigations, this research aims to elucidate the potential of these innovative therapeutic strategies to address existing treatment limitations and improve clinical outcomes for patients with GBM.

Chapter 2. Targeted Extracellular Vesicle to Deliver Verrucarin A to Treat Glioblastoma

Kai Chen, Yingnan Si, Jia-Shiung Guan, Zhuoxin Zhou, Seulhee Kim, Taehyun Kim, Liang Shan, Christopher D. Willey, Lufang Zhou, and Xiaoguang Liu

Biomedicines 2022, *10*(1), 130

Format adapted for dissertation

Abstract

Glioblastomas, accounting for approximately 50% of gliomas, comprise the most aggressive, highly heterogeneous, and malignant brain tumors. The objective of this study was to develop and evaluate a new targeted therapy, i.e., highly potent natural compound verrucarin A (Ver-A), delivered with monoclonal antibody-directed extracellular vesicle (mAb-EV). First, the high surface expression of epidermal growth factor receptor (EGFR) in glioblastoma patient tissue and cell lines was confirmed using immunohistochemistry staining, flow cytometry, and Western blotting. mAb-EV-Ver-A was constructed by packing Ver-A and tagging anti-EGFR mAb to EV generated from HEK293F culture. Confocal microscopy and the In Vivo Imaging System demonstrated that mAb-EV could penetrate the blood–brain barrier, target intracranial glioblastoma xenografts, and deliver drug intracellularly. The *in vitro* cytotoxicity study showed IC50 values of 2–12 nM of Ver-A. The hematoxylin and eosin staining of major organs in the tolerated dose study indicated minimal systemic toxicity of mAb-EV-Ver-A. Finally, the *in vivo* anti-tumor efficacy study in intracranial xenograft models demonstrated that EGFR mAb-EV-Ver-A effectively inhibited glioblastoma growth, but the combination with VEGF mAb did not improve the therapeutic efficacy. This study suggested that mAb-EV is an effective drug delivery vehicle and natural Ver-A has great potential to treat glioblastoma.

Keywords: glioblastoma; targeted delivery; monoclonal antibody-directed extracellular vesicle; natural compound verrucarin A

2.1. Introduction

Gliomas are the most prevalent primary intracranial cancer, including the highly malignant, aggressive, heterogeneous, and angiogenetic glioblastomas (GBM, WHO grade IV), which account for the majority of gliomas [19]. Surgery followed by the combination of involved-field radiation therapy and the DNA alkylating agent chemotherapy temozolomide (TMZ) is the current standard treatment strategy for newly diagnosed GBM in clinics [20,21]. Due to the stem-like cells, blood–brain barrier (BBB), or hypoxia, GBMs are usually resistant to conventional therapies with a high recurrence rate. The United States Food and Drug Administration has approved bevacizumab, an anti-vascular endothelial growth factor (VEGF) monoclonal antibody (mAb), to treat recurrent GBM. Despite the progress, the current standard care only provides a median survival of 14.6 months for GBM patients [22].

As reviewed before, multiple therapies have been developed to target the core signaling pathways that play important roles in GBM development [23]. For example, epidermal growth factor receptor (EGFR) inhibitors (TK1, neratinib, cetuximab, rindopepimut) [23-26] anaplastic lymphoma kinase inhibitors (imatinib and crizotinib) [27-29], vascular endothelial growth factor (VEGF) inhibitors (bevacizumab, vatalanib, tivozanib, cediranib) [30-32], platelet-derived growth factor receptor (PDGFR) inhibitors (Sunitinib and Nintedanib) [33,34], phosphoinositide 3-kinase (PI3K)/protein kinase B (AKT)/mammalian target of rapamycin (mTOR) inhibitors (Sonolisib, Temsirolimus, Sirolimus, Everolimus, Vextalisib) [35,36], p53 restoration gene therapy (miRNA) [37], and retinoblastoma tumor suppressor (RB) pathway CDK4/6 inhibitors (Palboclib) [38] have been developed and/or evaluated in clinical trials. Many of these therapies have failed in clinical trials due to the

challenges of poor anti-tumor efficacy, development of drug resistance, and BBB. Therefore, new therapeutics and an efficient drug delivery vehicle are highly desired for GBM treatment.

The natural compound verrucarin A (Ver-A, a type D macrocyclic trichothecene), which is isolated from the metabolites secreted by Myrothecium verrucaria [39], has been reported as a highly potent therapy to treat cancers. For instance, previous studies demonstrated that Ver-A had strong antiproliferative and proapoptotic effect on renal [40], hepatocellular [41], leukemia [42,43], and breast [44] carcinoma by blocking cell cycle progression via inhibiting cell cycle regulatory proteins cyclin D1/E, cyclin-dependent kinases inhibitor WAF1/21, or protein kinase B (AKT)/nuclear factor kappa B (NF-κB)/mammalian target of rapamycin (mTOR) prosurvival signaling, or by inducing apoptosis [45]. Moreover, our previous study showed that Ver-A can effectively inhibit neuroendocrine tumor growth [10]. The anti-GBM efficacy of Ver-A has not been investigated in GBM treatment so far.

As reviewed by Samec et al., targeted nanoparticles have been developed to deliver therapies to treat GBM [46], including liposomes carrying doxorubicin or irinotecan [47], polymeric nanoparticles delivering paclitaxel or miRNA mimics [48,49], solid lipid nanoparticles loaded with temozolomide and vincristine [50], polymeric micelles delivering doxorubicin and curcumin [51], and dendrimers bearing doxorubicin and siRNA [52]. These delivery vehicles have been limited in clinic application due to the poor stability, limited loading capacity, toxicity or reduced efficacy because of BBB. Recent studies showed that extracellular vesicle (EV), a natural endogenous nanoparticle, has great potential for

targeted delivery of highly potent drugs with the advantages of immune tolerance, circulation stability, capability to cross BBB, and tumor targeting via surface-tagged GBM-targeted reagents [53,54]. Our previous studies have established the platform of EV biomanufacturing and surface tagging [9] and demonstrated its capability of targeted delivery of combined therapies [10]. Furthermore, we have demonstrated and reported that the monoclonal antibody (mAb) is effective to target tumor *in vivo* [11-14] or direct drug delivery vehicles such as liposomes and EVs to target tumors [12,47]. Therefore, mAb-EV was constructed to deliver payload to GBM.

The literature has reported multiple growth factors or cytokines surface receptors overexpressed in GBM [55,56], including EGFR, PDGFR, VEGFR, transforming growth factor-βR, hepatocyte growth factor/scatter factor receptor, G protein-coupled receptor, interleukin-4, 13, or Urokinase-type plasminogen activator receptor. As an important signal in the receptor tyrosine kinase (RTK) pathway, EGFR or variant III (EGFRvIII) is overexpressed in over 40% of GBM patients [57] and is an attractive target for the development of targeted therapies, such as geftinib, neratinib, and CAR-T cells [23]. The chimeric anti-EGFR mAb (cetuximab) showed strong binding to EGFR and EGFRvIII, which was tagged on the surface of EV to target GBM in this study.

This study aimed to develop and evaluate a new targeted therapy, i.e., mAb-EV-delivered Ver-A, to treat the malignant EGFR-positive GBMs. The high surface expression of EGFR in GBM patient tissues and cell lines was confirmed. The mAb-EV-Ver-A was constructed and characterized. The GBM targeting, drug delivery, toxicity, and anti-tumor efficacy of

the developed therapy were evaluated using cell lines and intracranial xenograft mouse models. Our study showed that the anti-EGFR mAb-EV-Ver-A can effectively target GBM and inhibit the tumor growth with minimal toxicity.

2.2. Results

2.2.1. EGFR surface expression in GBM

To assess the surface receptor expression of EGFR, GBM tissue microarray slides (35 GBM cases and 70 cores) were performed with IHC staining (Figure 1A). The relative expression level of receptor was analyzed with ImageJ and quantitated using the score of ratios of DAB intensity: nuclei intensity. The IHC staining showed that 54% (38 of 70) of patient tissue samples had high (score of >10) or medium (score of 5–10) expression with cell membrane localization, 34% (24 of 70) of samples had low expression (score of 1–5), and 8% (8 of 70) of samples had no or minimal expression (score < 1). The representative images of IHC staining with high (C1), medium (E3), and low/no (G1) expression are presented in Figure 1A. The IHC staining of the adjacent normal brain tissues has low or minimal expression, indicating that EGFR is a good target of GBM. These data indicated that the EGFR-targeted EV-drug could cover >53% patients with malignant GBM. For the EGFR-GBM patients, we can consider targeting an alternative receptor, such as CXCR4 or CD276, which was reported to overexpress in GBM patient tissues [58,59].

Furthermore, the surface expression of EGFR in malignant GBM cell lines was evaluated by staining U87 and U251 cells with an antibody at room temperature. As presented in Figure 1B, flow cytometry analysis showed that the U87 and U251 cells had high EGFR

expression with a binding rate of 97.1% and 74.6%, respectively (Figure 1B). The VEGF expression in these cell lines was low with a binding rate of 4.3%–7.0%. Finally, the EGFR expression was confirmed using Western blotting (Figure 1C). Although the predicted size of human EGFR was 134 kDa, two bands were detected by Abcam primary anti-human EGFR antibody with observed sizes of ~130 kDa and ~170 kDa in U87 and U251 cells, respectively. The possible root cause of changed molecular weight was high post-translational modifications or alternative splice variants of EGFR. The calculated relative expression (i.e., receptor intensity/β-tubulin intensity) of U87 and U251 was 1.43 and 1.05, respectively.

2.2.2. Construction of targeted mAb-EV-Drug

The EGFR mAb-EV-Ver-A (Figure 2A) was constructed following our previously established platforms of EV production, surface labeling, and drug packing [9,10]. The size distribution of the targeted vehicle (mAb-EV-Ver-A) was analyzed using NanoSight assay, demonstrating a homogenous distribution with an average diameter of 117.7 ± 1.4 nm (Figure 2B). The vehicle was further confirmed with transmission electron microscopy (TEM) image (Figure 2C). The purified EV was confirmed with Western blotting by analyzing the biomarkers of surface tetraspanins (CD63 and CD81), heat shock protein 70 (HSP70), and glyceraldehyde 3-phosphate dehydrogenase (GAPDH), as presented in Figure 2D. The constructed mAb-EV-drug was further evaluated by testing the GBM targeting, toxicity, and anti-tumor cytotoxicity or efficacy in the following studies.

2.2.3. GBM targeting by mAb-EV

The confocal laser scanning microscopy (CLSM) imaging was used to test the *in vitro* targeted delivery capability of EGFR mAb-EV. As shown in Figure 3A, the mAb-EV-Liss Rhod can internalize into the cytoplasm of U87 cells and deliver the packed fluorescent dye (displayed as red color) or drugs intracellularly. The *in vivo* GBM specificity and biodistribution of EGFR mAb-Cy5.5 and mAb-EV-Cy7 were evaluated in U87-FLuc intracranially xenografted mouse model via i.v. injection. As described in Figure 3B, the live-animal IVIS imaging at 24 h demonstrated that the bioluminescent FLuc (tumor) and fluorescent Cy5.5 (mAb) overlapped in the brain, which suggested that the EGFR mAb penetrated the BBB and accumulated in the GBM xenograft. The ex vivo imaging of the important organs, such as the heart, lung, liver, spleen, kidney, and brain, confirmed the tumor targeting of the mAb, but also showed distribution of Cy7 in the liver. Furthermore, the capability of GBM targeting of mAb-EV-Cy7 was assessed and confirmed in the same animal model using IVIS imaging (Figure 3C). The ex vivo images also indicated the distribution of mAb-EV-Cy7 in the liver and kidney, probably due to the metabolism of Cy7 dye, which needs further investigation. These data showed that both mAb and mAb-EV can penetrate the BBB, target the GBM xenograft, and deliver the packed cargos.

2.2.4. *In vitro* anti-cancer cytotoxicity

First, the *in vitro* anti-GBM cytotoxicity of eight dosages of free drugs, i.e., TMZ (control, standard chemotherapy in clinics) and Ver-A (Figure 4A) were tested with U87 and U251 cells in 96-well plates. The relative cell viabilities were 100%–0.0% for U251 cells and 100%–0.0% for U87 cells post treatment with 0, 10, 25, 50, 75, 100, 150, and 200 μM of

free TMZ in the end of cytotoxicity assay. The relative cell viabilities were 100%–0.0% for U251 cells and 100%–3.6% for U87 cells post treatment with 0, 5, 10, 15, 20, 30, 40, and 50 nM of free Ver-A in the end of the assay. The calculated IC50 values were 49.2 μM for U251 and 17.5 μM for U87 cells that were treated with TMZ, and 2.1 nM for U251 and U87 cells that were treated with Ver-A. These results indicated that the Ver-A reduced GBM cell growth at low, single-digit nanomolar concentrations in a dose-dependent manner, which was more toxic to GBM cells than TMZ.

Second, to investigate the synergism of standard chemotherapy TMZ and the highly potent Ver-A, we also tested multiple dosages of combined TMZ and Ver-A (Figure 4A). The combined TMZ/Ver-A showed similar cytotoxicity to both U251 and U87 cells as Ver-A only in the tested dosages. The possible reason is that the high potency of Ver-A masked the cytotoxicity of TMZ at low dosages. Since TMZ is the standard chemotherapy for newly diagnosed GBM, we applied TMZ to treat GBM first to mimic clinical application, followed by mAb-EV-Ver-A treatment to evaluate the *in vivo* anti-GBM efficacy.

Finally, we further investigated the possible anti-tumor mechanism of Ver-A by analyzing the proliferation markers in GBM cell lines (U251 and U87) using Western blotting analysis. The results showed that 2 nM of Ver-A reduced the expression of oncogenic anti-proliferation protein cyclin D1 and increased the expression of cyclin-dependent kinase inhibitors (p21 and p27) at 48 h after treatment (Figure 4B1). These results are consistent with the literature reported anti-cancer mechanism of Ver-A in pancreatic adenocarcinoma and prostate cancer [45,60] and our previous results in neuroendocrine cancer [10]. This study

indicated that Ver-A impacts the regulation of proliferation of GBM cells, although the mechanisms need further investigation. As reported in literature [20,21], TMZ is a DNA alkylating agent to induce cell cycle arrest at G2/M and eventually lead to apoptosis, which has different anti-tumor mechanisms from Ver-A. The Western blot analysis of cyclin D1, p21 and p27 in U251 and U87 cells that were treated with 20 μM of TMZ, and 2 nM of Ver-A is presented in Figure 4B2. The analysis of cell cycle phase distribution could further reveal the anti-GBM mechanism of combined TMZ and Ver-A, which will be performed in future. Altogether, the *in vitro* cytotoxicity study demonstrated that Ver-A is a highly potent payload to GBM.

2.2.5. Tolerated dosages (TD)

To investigate the possible toxicity of mAb-EV-Ver-A, 5 different doses of mAb-EV-Ver-A, including 0, 0.5, 1, 2, 3, 4, and 5 mg/kg doses, were injected into BALB/cJ via the tail vein (n = 2). During the 14 days post injection, the changes of body weight were in the range of 4.3–22.7% for all the groups (Figure 5A). The H&E staining of the sections of important organs (brain, heart, lung, liver, kidney, and spleen) did not reveal any morphology change or necrosis after mAb-EV-Ver-A treatment, indicating minimal or no toxicity of the targeting delivered Ver-A (Figure 5B). Two dosages of mAb-EV-Ver-A (1 and 3 mg/kg), which did not show toxicity, were used in the following *in vivo* anti-tumor efficacy study. The low n value was used in this study and one mouse was lost by accident from a dosage of 5 mg/kg, so further toxicology studies are needed to make a statistically significant conclusion in the future.

2.2.6. *In vivo* anti-GBM efficacy in intracranial xenograft model

To evaluate the *in vivo* treatment efficacy of the targeted delivery of Ver-A by mAb-EV, we generated U87-FLuc intracranial xenograft models using 6-week NSG mice. When tumor volume reached bioluminescent intensity of over 20,000 on day 7 as detected by IVIS imaging, the xenografted mice were treated with 1 mg/kg of TMZ daily on days 7–9 to mimic the clinical treatment. Then, the mice were further treated with PBS (negative control), 1.0 mg/kg mAb-EV-Ver-A, 3.0 mg/kg mAb-EV-Ver-A, and 3.0 mg/kg mAb-EV-Ver-A in combination with VEGF mAb (positive control) via i.v. injection on days 9, 12, 16, 23, 30, and 34 post cell implantations. The tumor volume was monitored by measuring fluorescent flux with IVIS. The representative IVIS images captured pre- and post-mAb-EV-Ver-A injection are presented in Figure 6A. Both absolute tumor flux and relative tumor volume fold change are described in Figure 6B. Specifically, the GBM tumor growth was significantly inhibited in the 1 mg/kg and 3 mg/kg of mAb-EV-Ver-A treatment groups as compared to the control group ($p \leq 0.005$) during the treatment period. The combination with anti-VEGF mAb did not improve the treatment efficacy. In addition, there was no obvious body weight difference among all the four groups (Figure 6B), indicating minimal side toxicity. The treatment was terminated when the control group showed obvious slow locomotion and body weight loss (>20%). The harvested brain tumor tissues were sectioned to perform H&E staining to further confirm the anti-GBM efficacy. The H&E images demonstrated an obvious reduction of the tumor burden with the treatment of mAb-EV-Ver-A (Figure 6C). These findings support the hypothesis that mAb-EV-Ver-A can effectively target the GBM xenograft and successfully deliver drugs for GBM treatment.

2.3. Discussion

The combination of surgery, radiotherapy, and chemotherapy is still the standard care to treat GBM in clinics. Targeted therapies driven by the tumor or immune biomarkers have been demonstrated promise in preclinical GBM models. However, as reviewed in literature [23,61], an extensive number of targeted therapies have failed in clinical trials because of the insufficient inhibition of signaling pathway, poor drug delivery efficiency, or tumor heterogeneity. Our research identified and evaluated a new drug candidate (Ver-A) as an adjuvant therapy post primary treatment and established a targeted delivery vehicle (mAb-EV) that could penetrate the BBB, target GBM cells, and effectively inhibit tumor growth as well as minimize systemic toxicities. To better capture the GBM tumor microenvironment, we are developing the patient-derived xenograft model, which could be used to further evaluate the new therapy in future studies.

This study demonstrated that Ver-A can kill ~100% cells of multiple GBM lines and inhibit tumor growth and reduce tumor volume in a GBM intracranial xenograft model post TMZ treatment (mimicking clinic treatment). Ver-A has multiple anti-tumor mechanisms, such as inhibition of proliferation, block of cell cycle in the S phase, depolarization of mitochondria, and induction of apoptosis, so it could be an ideal drug candidate or an adjuvant of standard chemotherapy of DNA alkylating TMZ in GBM treatment. In addition to the high potency, these integrated anti-tumor mechanisms of Ver-A could reduce the possibility of drug resistance development during long-term treatment. In the future, we will further investigate the anti-GBM mechanisms of Ver-A. Moreover, Ver-A is a natural compound and has low systemic toxicity.

Although multiple drug delivery vehicles (liposome, polymeric nanoparticle, solid lipid, and polymeric micelle) have been developed in cancer therapy, it is very challengeable to use these synthesized nanoparticles in GBM treatment due to the issues of stability and/or the BBB [46]. As a natural vesicle, EV has multiple advantages over the synthesized particles, including low immune toxicity, high stability, and efficient penetration of the BBB [53,54]. This study used our established biomanufacturing platform [9,10] to generate EV from human cell line, surface-tagged mAb, and the packed drug Ver-A, which demonstrated the capabilities of high GBM targeting and effective drug delivery. Importantly, different mAbs (single or multiple) can be easily conjugated to the surface of EV to target the well-known or newly identified receptors in GBM or angiogenesis to cross the BBB.

The literature [57,62-64] and our immunohistochemistry staining of GBM patient tissue microarray show that EGFR or EGFRvIII is overexpressed in more than 40% GBM patients. The chimeric anti-EGFR mAb, Cetuximab, has been approved by the U.S FDA and used to treat head and neck cancer [65,66] and colorectal cancer [67,68]. The therapies to target EGFR signaling pathways have limited clinical benefits in GBM treatment [69-71], but EGFR has been demonstrated as a good surface target, and the anti-EGFR mAb or peptide can direct the targeted delivery of therapies to GBM [57,72-75]. The anti-EGFR mAb-EV-Ver-A constructed in this study showed high anti-GBM efficacy, indicating EGFR as a good surface receptor to target GBM. To treat the EGFR-GBM, we can tag the mAbs to target other surface receptors overexpressed in GBM, such as PDGFR, TGF-βR, CXCR4, uPAR, and others as reported in the literature [55,56].

The anti-VEGF mAb, Bevacizumab, remains the only U.S FDA-approved molecular therapy to treat recurrent GBM. The clinical data showed that Bevacizumab can improve the progression-free survival but has no benefit to improve overall survival [76]. In this study, we tested the combined mAb-EV-Ver-A and anti-VEGF mAb but observed no benefit of VEGF mAb in GBM treatment.

In addition to chemotherapy, immunotherapies, such as CAR-T [77-80] and immune checkpoint inhibitors of cytotoxic T lymphocyte-associated protein 4 (CTLA-4), programmed cell death protein 1 (PD-1), and programmed cell death protein 1 ligand (PD-L1) [81-83], have been recently investigated for GBM treatment. Moreover, induced pluripotent stem cell-based regenerative medicine [84] and gene therapies (adenovirus, herpes simplex virus-1, retrovirus, shRNA, siRNA, non-viral vectors) have been developed and evaluated [85-88]. We will evaluate the combination of our mAb-EV-Ver-A and immunotherapy or gene therapy for GBM treatment in the future.

The targeted mAb-EV has great potential to deliver chemotherapy to treat the highly aggressive glioblastoma because of the capability to cross the blood–brain barrier, specificity of tumor targeting, and advantage to deliver combined therapies such as chemotherapy, gene therapy, and others. The natural compound, verrucarin A, has a high potency and low systemic toxicity in glioblastoma treatment, which could provide a new therapy for patients. Despite these promising results, the developed mAb-EV-Ver-A needs further pre-clinical evaluations such as pharmacokinetics, pharmacodynamics, and immune modulatory responses in the future.

2.4. Materials and methods

2.4.1 Cell lines, seed cultures, and media

The human GBM cell lines, including malignant U251 (MilliporeSigma, Manassas, VA, USA), U87 (ATCC, Manassas, VA, USA), and U87-FLuc (ATCC), were used to evaluate the developed targeted therapy. The U251 cells were maintained in EMEM (Gibco, Grand Island, NY, USA) supplemented with 2 mM L-glutamine, 1% non-essential amino acids (NEAA), 1 mM sodium pyruvate, 10% fetal bovine serum (FBS), and 1% penicillin/streptomycin (P/S) in T25 or T75 flasks (Fisher Scientific, Waltham, MA, USA). The U87 and U87-FLuc cells were maintained in EMEM supplemented with 10% FBS and 8 µg/mL Blasticidin. The normal human astrocyte cell line NHA (Lonza, Greenwood, SC, USA) and the negative control of GBM were maintained in DMEM (Gibco) containing 10% FBS. All cell cultures were maintained in CO2 incubator (Caron, Marietta, OH). The cell growth was monitored by analyzing viable cell density (VCD) and viability.

2.4.2. Intracranial xenograft model

The five-week-old NSG (NOD.Cg-Prkdc<scid> Il2rg<tm1Wjl>/SzJ) mice were purchased from Jackson Laboratory (Bar Harbor, ME, USA) to generate a GBM intracranial xenograft model. A total of 5 × 105 of U87-FLuc cells were stereotactically injected into mice using the Stereotaxic Instrument (Fisher Scientific) following our reported protocol [11].

2.4.3. Construction of mAb-EV-drug

As detailed in our previously published platform [9], EV was produced by HEK293 cells in a FreeStyleTM 293 expression medium (Gibco). Briefly, the 250 mL of basal medium supplemented with 6 g/L glucose, 6 mM L-glutamine, and 3.5 g/L Cell Boost 6 was inoculated with HEK293 cells with a seeding density of 0.3 × 106 cells/mL in 1 L shaker flasks. The EV production culture was incubated at 37 °C and an agitation of 80 rpm. The spent medium was collected when cell viability dropped <80%. The harvested EV was purified with the size exclusion column of Vivaspin 300 kDa MWCO or the fast flow affinity purification column packed with NHS-activated Sepharose (Cyvita, Marlborough, MA, USA), which was coupled with an anti-CD63 antibody (BioLegend, San Diego, CA, USA). The EV purity isolated with size exclusion purification is enough to deliver drugs *in vivo*, as validated in our previous study [9]. The generated EV was titrated with NanoSight (Malvern Panalytical, Malvern, UK) and characterized with Western blotting. Then, the mAb-EV was constructed by tagging anti-EGFR mAb to EV via DSPE-PEG-NHS linker and modified with mPEG-DSPE to improve its circulation stability following our established procedure [9]. The literature also reported that the PEG tagged on the surface of EV could provide stealth property to "evade" the immune response [9], reduce the clearance rate, and extend the circulatory half-life [7] of the engineered EV. The untagged mAb, linker, and stabilizer were removed using a Vivaspin 300 kDa MWCO column. Finally, the mAb-Exo-drug was generated by incubating a 10 × 1010 particle (ptc) of EV with 0.101 mg (200 nanomole) of Ver-A in 8 mL of PBS overnight at room temperature, and the unpacked free drug was removed with the Vivaspin 100 kDa column. The mAb-EV (1 × 1012 ptc) was labeled with Liss Rhod or Cy7 fluorescent dye (16.7 nmol) via mPEG-1, 2-Distearoyl-sn-

glycero-3-phosphoethanolamine (DSPE, 2 μmol) to monitor the *in vitro* drug uptake or *in vivo* drug biodistribution, respectively.

2.4.4. *In vitro* anti-GBM cytotoxicity

To test *in vitro* anti-GBM cytotoxicity [8], the U251 or U87 cells were seeded in 96-well plates with a density of 5×10^4 cells/mL in 200 μL of growth medium and incubated for 24 h. The 5-day treatment was performed by adding free TMZ (0, 10, 25, 50, 75, 100, 150, or 200 μM), free Ver-A (0, 5, 10, 15, 20, 30, 40, or 50 nM), or combined TMZ (0–50 μM) and EV-Ver-A (0–10 nM). The treated cells were washed using PBS, and 100 μL fresh culture medium was added to the wells after wash. Then TACS 2,5-diphenyl-2H-tetrazolium bromide (MTT) Cell Proliferation Assay (R&D Systems, Minneapolis, MN, USA) was performed to test the relative cell viability by adding 10 μL of MTT reagent to each well to develop a purple color, adding 100 μL of detergent reagent, and reading OD values at 570 nm, which is proportional to the viable cell number. The IC50 values were calculated using ED50V10 Excel add-in.

2.4.5. Patient tissue array (TMA) and immunohistochemistry (IHC) staining

The brain GBM tissue arrays, including 35 cases and 70 cores, were purchased from US Biomax (Derwood, MD, USA). IHC staining was performed to identify the surface receptor in patient tissues as we described before [12,89]. The TMA slides were stained with rabbit anti-human EGFR mAb (Abcam, Waltham, MA, USA) and counterstained with hematoxylin.

2.4.6. Western blotting

Western blotting analysis was performed to analyze EGFR expression and the proliferation markers, such as Cyclin D1, p21, and p27, and post mAb-EV-Ver-A treatment in U87 and U251 cell lines was performed following previously established protocols [9,10].

2.4.7. Flow cytometry analysis

The GBM surface binding rate of anti-human EGFR mAb in U87 and U251 cells was evaluated and quantitated using a BD LSRII flow cytometer (BD Biosciences, San Jose, CA, USA) following our published methods [41]. Briefly, the mAb was labeled with Alexa Fluor™ 647 labeling kit. The 1×10^6 of GBM cells were collected, washed, and re-suspended in 100 µL of PBS containing 1% FBS, and incubated/stained with 1 µg of AF647-EGFR mAb at room temperature for 30 min. The stained cells were washed three times with PBS and analyzed with a flow cytometer. The absolute cutline of negative staining, i.e., glioblastoma cells without antibody staining, was used in gating.

2.4.8. Transmission electron microscope (TEM)

The TEM image was taken to confirm the isolated EVs. First, the EV sample was solved in 10 mM Tris buffer and concentrated with 300 kDa column. Second, the formvar-carbon-coated grid was discharged through K100X Glow Discharge with parameters of 50 mA and 20 s. Third, the EV sample was applied to grid for 1 min and negatively stained with 1% filtered uranyl acetate. Fourth, the sample on the grids was imaged with a Tecnai T12 transmission electron microscope (FEI, Hillsboro, OR, USA) equipped with AMT CCD camera.

2.4.9. Confocal imaging

The *in vitro* uptake of mAb-EV by GBM cell lines was confirmed with two-color confocal microscopy imaging [10]. Briefly, the mAb-EV was stained with Liss Rhod fluorescent dye (red) with mAb-EV:Liss Rhod:mPEG-DSPE molar ratio of 1:10,000:300,000 at room temperature with overnight horizontal shaking in the dark. The free dye was removed by a 100 kDa MWCO concentrator. The U251 cells were seeded in a chambered glass coverslip with viable cell density of 1×10^5 cells/mL, and the cytoplasm and nucleus of cells were infected and stained with BacMam GFP Transduction Control (Green) at MOI of 50 for overnight. Then, mAb-EV-Liss Rhod was mixed and incubated with GBM cells overnight. After washing with the fresh cell growth medium, the live-cell images were collected using Nikon A1R-HD25 confocal microscope with a high-speed resonance scanner (Nikon USA, Melville, NY, USA).

2.4.10. In Vivo Imaging System (IVIS) imaging

The tumor growth of U87-FLuc cell line-derived intracranial xenografted NSG mouse model was monitored by measuring bioluminescent signal (FLuc) with IVIS Lumina Series III (PerkinElmer, Waltham, MA, USA) every three to four days post tumor cell implantation. To confirm the *in vivo* GBM targeting and the capability to penetrate the BBB of the mAb-EV-drug, 3×10^{11} particles (ptc) of Cy7-labeled mAb-EV or 50 μg of Cy5.5-labeled mAb was intravenously (i.v.) injected into mice via the tail vein. Then, the xenograft mice were imaged under IVIS to capture the tumor bioluminescence (FLuc) at a wavelength of 550 nm and the targeted delivered fluorescence (Cy7) at a wavelength of 750 nm of xenograft binding at 24 h post injection. The *in vivo* biodistribution and GBM-

targeting of mAb or mAb-EV was analyzed by detecting the co-localization of FLuc and Cy7 signals. Furthermore, the important organs, such as the brain, heart, lung, kidney, and spleen, were also extracted to collect ex vivo images to check the possible off-target binding.

2.4.11. Tolerated dosage (TD) study

To investigate the tolerated dosages of targeting delivered Ver-A and its potential toxicity, six doses of mAb-EV-Ver-A (i.e., 0, 1, 2, 3, 4, and 5 mg/kg) were i.v. injected into the non-tumor bearing BALB/cJ mice (Jackson Laboratory) via the tail vein (n = 2). The body weight of mice was monitored every 2 days for a total of 14 days. All mice showed no overt changes in general health and body weights (>20%). At the end of the study, the mice were sacrificed to collect the major organs, including the brain, heart, lung, liver, kidney, and spleen, for hematoxylin and eosin (H&E) staining to analyze the potential toxicity of mAb-EV-Ver-A.

2.4.12. *In vivo* anti-GBM efficacy study

The U87-FLuc intracranially xenografted NSG mice were randomized into 4 groups (n = 5) when the FLuc bioluminescence intensity was higher than 20,000 in IVIS imaging on day 7 post transplantation. To mimic clinical treatment, all xenograft mice were treated with 1 mg/kg of free TMZ via i.p. injected daily on days 7–9. Then the mice were treated with mAb-EV (negative control), 1.0 mg/kg of mAb-EV-Ver-A, 3.0 mg/kg of mAb-EV-Ver-A, and 3.0 mg/kg of mAb-EV-Ver-A in combination with 5 mg/kg of anti-VEGF mAb via tail vein injection on a Q3/7Dx6 schedule (3/7-day interval for 6 injections). The body

weight and tumor volume were monitored every 3–4 days. The mice were sacrificed when we observed slow locomotion and obvious body weight drop in the control group.

2.4.13. Hematoxylin and eosin (H&E) staining

The sections of major organs harvested from the *in vivo* treatment with mAb-EV-Ver-A were stained with H&E. The detailed staining procedure has been reported in our previous publications [12,89].

2.4.14. Statistical analysis

The experimental data were presented as mean ± standard error of the mean (SEM). Two group comparisons were performed using unpaired Student's t test to determine the probability of significance. Comparison was performed using a one-way ANOVA followed by post-hoc (Dunnett's) analysis. The sample size in animal study was determined following our previous therapy study [13]. Statistical significance with ** p value of <0.005 was considered for all tests.

Founding

This research was funded by the USA National Institute of Health (NIH) 1R01CA238273-01A1 and R21CA226491-01A1.

Figures

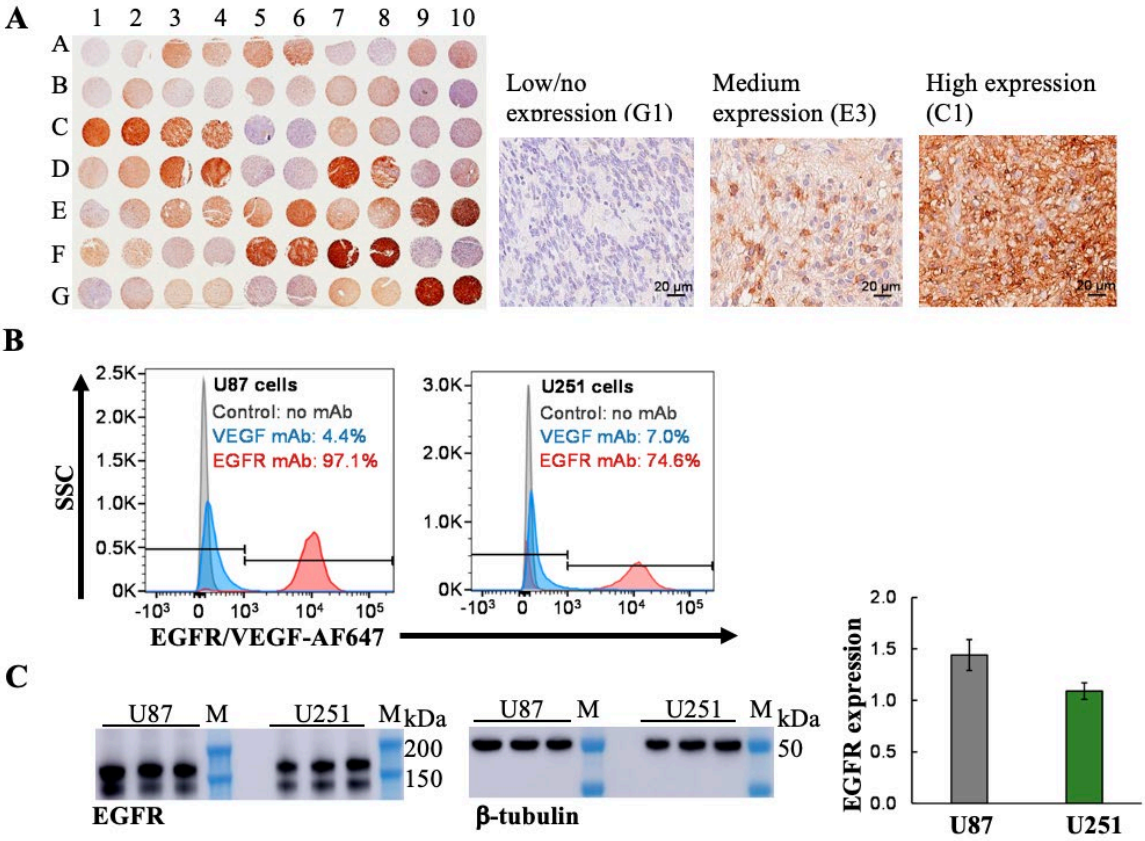

Figure 1. EGFR expression in GBM

(A) IHC staining of patient tissue microarray (TMA) to analyze EGFR surface expression in GBM (35 cases, 70 cores). Scale bar equals 20 μm. (B) Evaluation of surface binding rate of VEGF mAb-AF647 (blue) or EGFR mAb-AF647 (red) in GBM U87 and U251 cells by flow cytometry analysis. One million cells were stained with 1 μg of mAb-AF647 at room temperature for 30 min. (C) Western blotting analysis of EGFR in two GBM cell lines. 1: U87; 2: U251; and 3: marker.

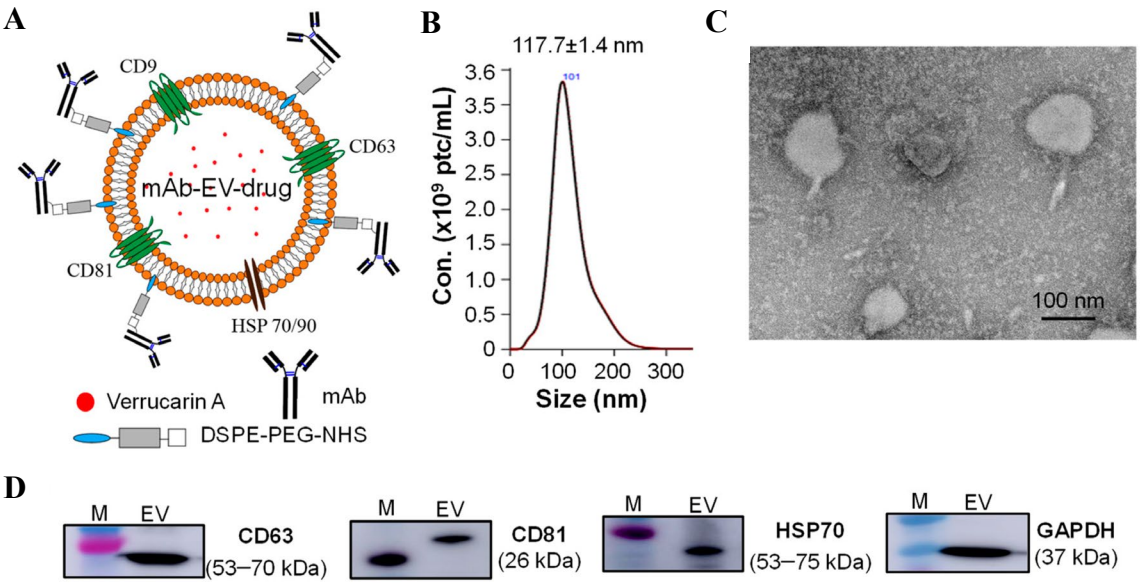

Figure 2. Characterization of mAb-EV-drug.

(A) Construction and structure of mAb-EV-Ver-A: mAb was surface tagged on EV via DSPE-PEG-NHS and payload Ver-A was packed in EV. **(B)** Size distribution by NanoSight assay. **(C)** TEM image of mAb-EV-Ver-A. Scale bar equals 100 nm. **(D)** Western blotting analysis of EV biomarkers (CD63, CD81, HSP70, and GAPDH).

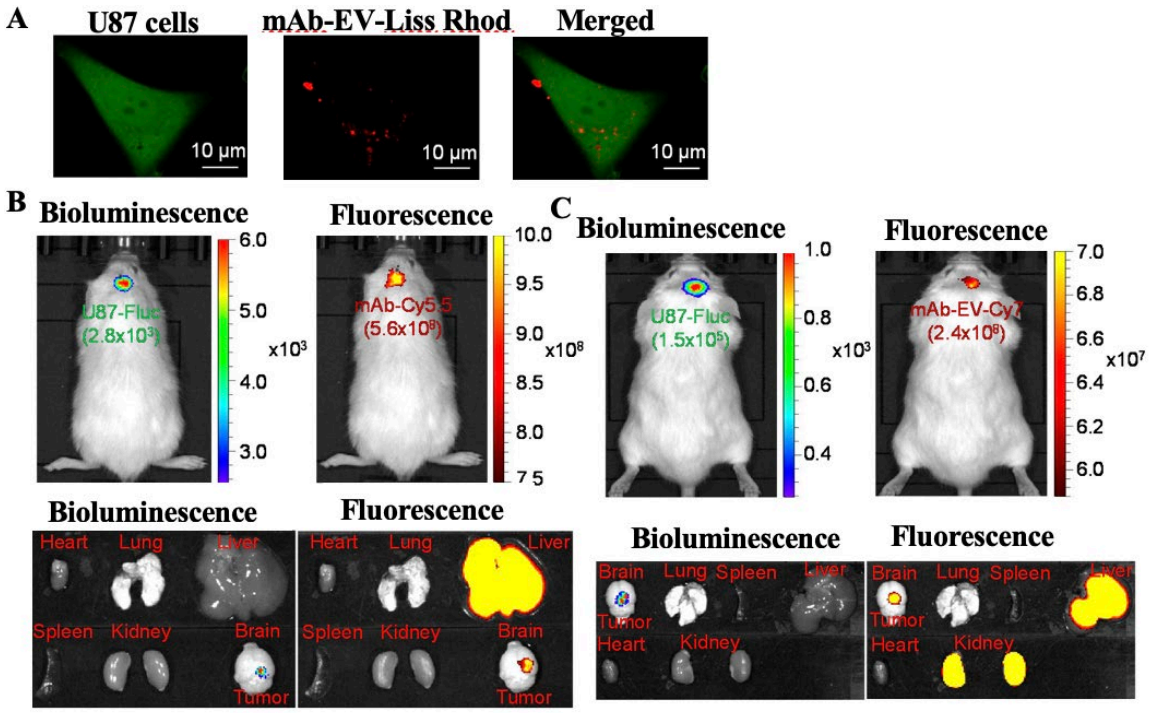

Figure 3. Evaluation of GBM targeting of mAb-EV.

(A) Live-cell CLSM imaging of mAb-EV-Liss Rhod internalization in U87 cells. Two-color CLSM: whole cell labeled with GFP (displayed as green) and mAb-EV labeled with Liss Rhod (displayed as red). Scale bar equals 10 μm. **(B)** *In vivo* live animal and ex vivo IVIS imaging of tumor and important organs to analyze tumor targeting and biodistribution of mAb-Cy5.5 at 24 h post i.v. injection in U-87-FLuc intracranial xenograft mouse model (n = 3). **(C)** IVIS imaging of the live animal and tumor and organs to analyze tumor targeting and biodistribution of mAb-EV-Cy7 at 24 h post i.v. injection (n = 3).

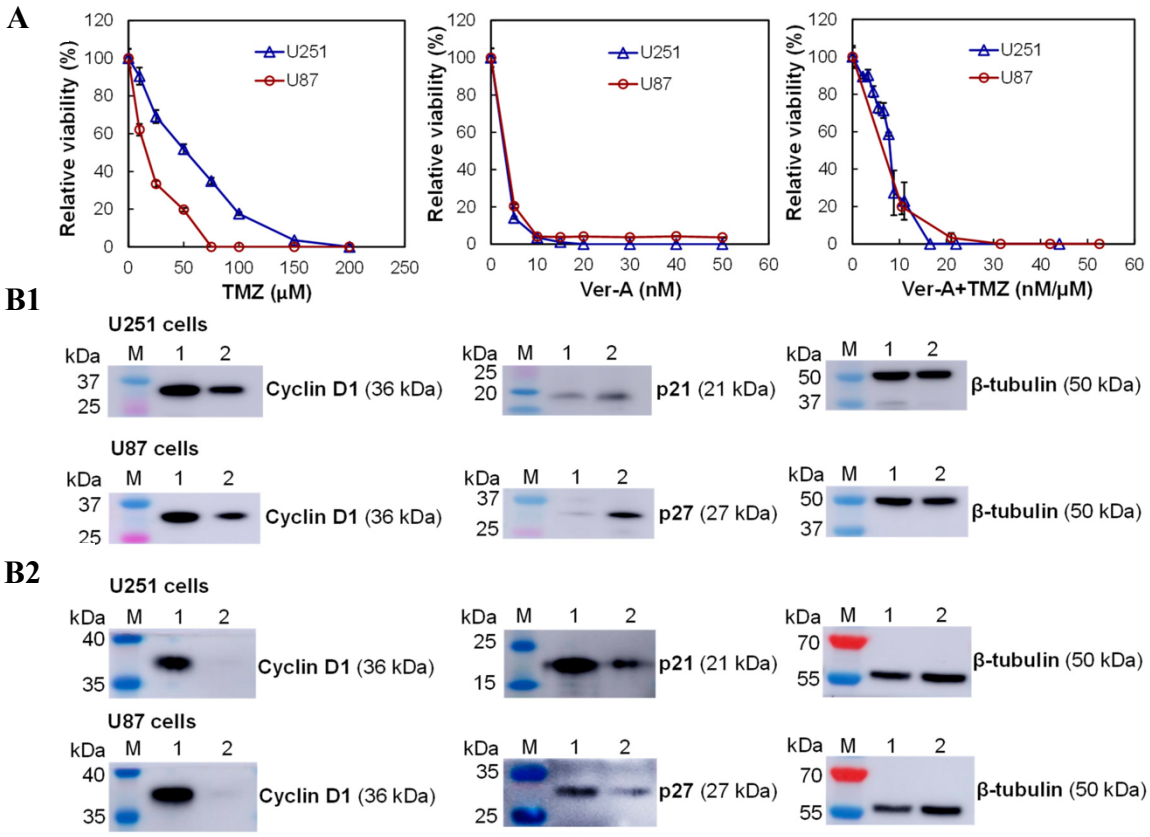

Figure 4. In vitro anti-GBM cytotoxicity of free drugs.

(**A**) Evaluation of TMZ, Ver-A, and combined TMZ and Ver-A using U87 and U251 cells. Δ: U251 and ○: U87. Data represent mean ± SEM, $n = 3$. (**B**) Western blotting analysis of proliferation and apoptosis biomarkers in U87 cells and U251 cells treated with (**B1**) Ver-A or (**B2**) TMZ in combination with Ver-A. M: marker; 1: GBM cells without treatment; 2: GBM cells treated with 2 nM Ver-A or 20 μM TMZ and 2 nM Ver-A.

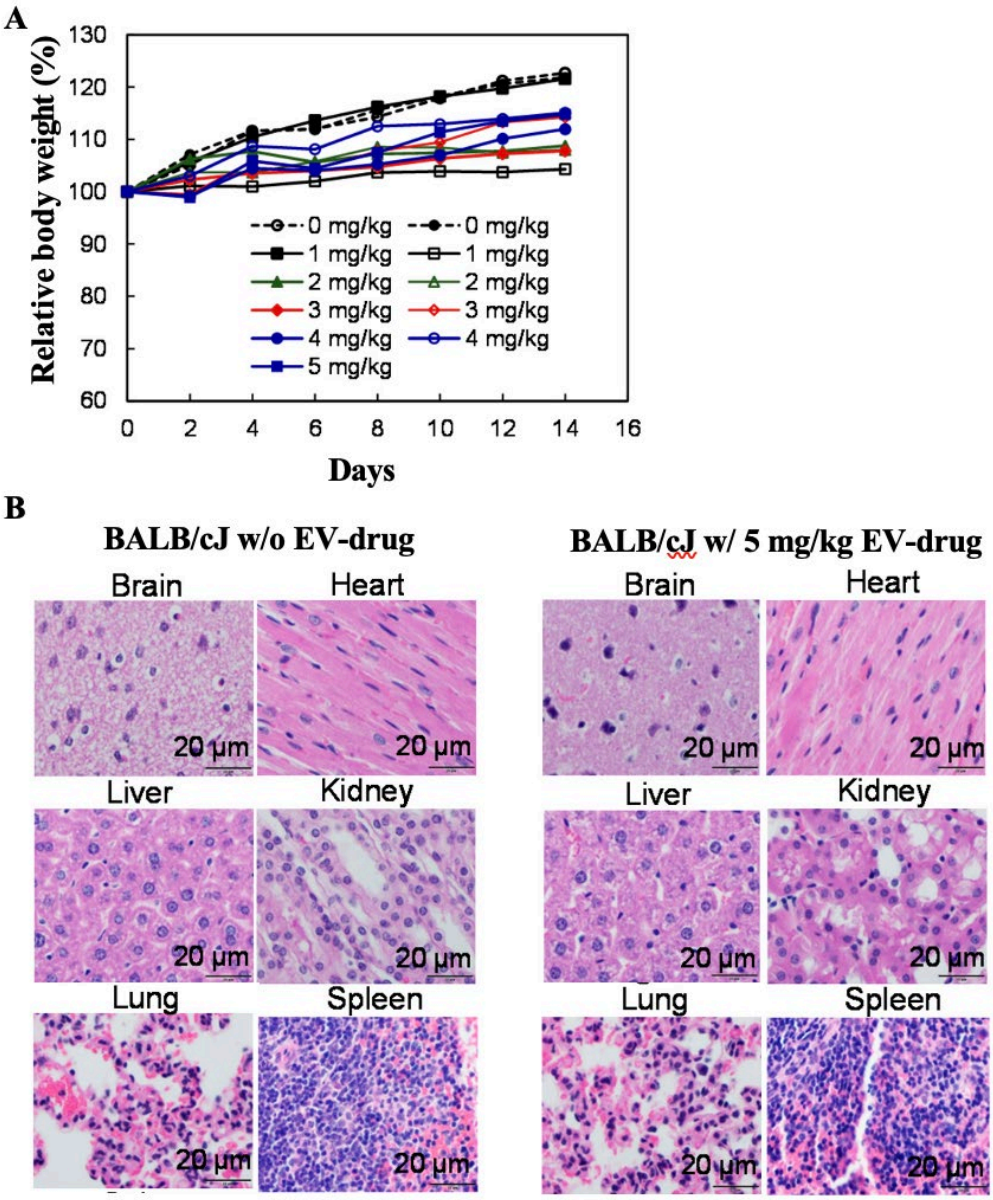

Figure 5. Tolerated dosage (TD) and toxicity analysis of mAb-EV-Ver-A.

(**A**) Body weight change of non-GBM carrying BALB/cJ mice after treatment with five dosages of mAb-EV-Ver-A, including 0 (●, ○), 1 (■, □), 2 (▲, Δ), 3 (♦, ◊), 4 (●, ○), and 5 (■) mg/kg (*n* = 2). (**B**) H&E staining of main organs, including the brain, heart, lung, liver, kidney, and spleen. Scale bar equals 20 μm.

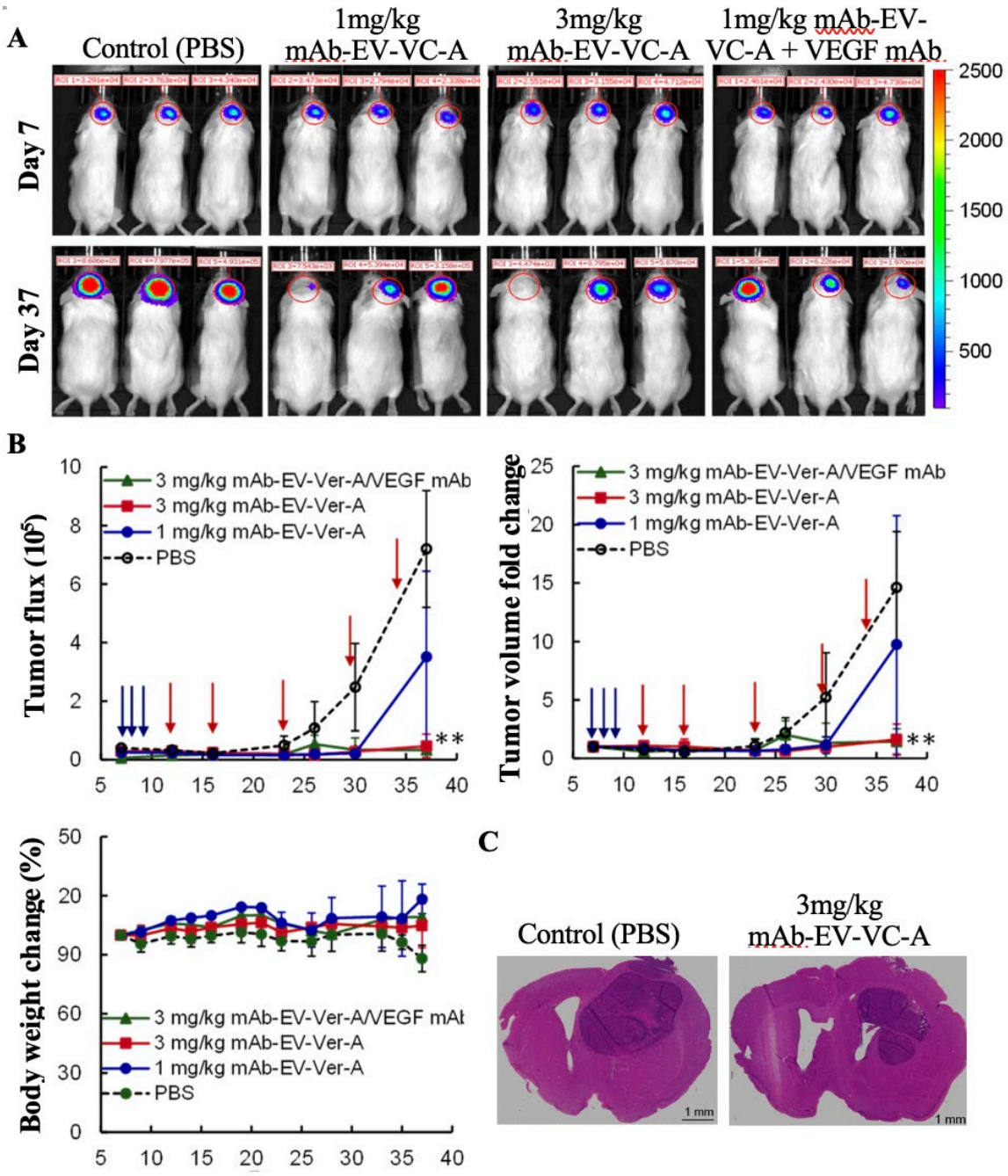

Figure 6. *In vivo* evaluation of the anti-GBM efficacy of mAb-EV-Ver-A

All mice were treated with 1 mg/kg TMZ daily on days 7–12. (**A**) Representative IVIS images of GBM intracranial xenograft mice treated with EGFR mAb-EV-Ver-A on days 12, 16, 23, 30, and 34. (**B**) Tumor flux, volume fold change, and body weight profiles.

Tumor growth was monitored by measuring the FLuc bioluminescence using IVIS, and body weight was measured every 3–4 days. The blue arrows indicate the I.P. administration of TMZ. The red arrows indicate the I.V. administration of mAb-EV-Ver-A. ○: PBS (control); ●: 1.0 mg/kg mAb-EV-Ver-A; ■: 3.0 mg/kg mAb-EV-Ver-A; and ▲: 3.0 mg/kg mAb-EV-Ver-A in combination with VEGF mAb injection on Q3/7Dx7. ** $p < 0.005$ vs. control using ANOVA followed by Dunnett's *t*-test. Data represent mean ± SEM, $n = 5$. (**C**) Representative H&E staining of brain tissue section. Scale bar: 1 mm.

Chapter 3. Advanced biomanufacturing and evaluation of adeno-associated virus

Kai Chen, Seulhee Kim, Siying Yang, Tanvi Varadkar, Zhuoxin Zora Zhou, Jiashuai Zhang, Lufang Zhou & Xiaoguang Margaret Liu

Journal of Biological Engineering 2024, 18(1):15

Format adapted for dissertation

Abstract

Recombinant adeno-associated virus (rAAV) has been developed as a safe and effective gene delivery vehicle to treat rare genetic diseases and recently expanded to treat heart failure, cancers, and organ dysfunction. This study aimed to establish a novel biomanufacturing process to achieve high production and purification of various AAV serotypes (AAV2, 5, DJ, DJ8). First, a robust suspensive production process was developed and optimized using Gibco Viral Production Cell 2.0 in 30-60 mL shaker flask cultures by evaluating host cells, cell density at the time of transfection and plasmid amount, adapted to 60-100 mL spinner flask production, and scaled up to 1.2-2.0-L stirred-tank bioreactor production at 37 ºC, pH 7.0, 210 rpm and DO 40 %. The optimal process was scaled up and generated AAV with volumetric titer of $7.52x10^{10}$ vg/mL. Second, a new AAV purification using liquid chromatography was developed and optimized to reach recovery rate of 85-95 % and good purity of all four serotypes. Different post-purification desalting and concentration procedures were also investigated. Then the generated AAVs were evaluated *in vitro* using Western blotting, transmission electron microscope, confocal microscope, and bioluminescence detection. Finally, the *in vivo* infection capability and functional gene expression of AAV were confirmed in tumor xenografted mouse model. In conclusion, this study reported an advanced robust, scalable, and universal biomanufacturing platform of AAV production, clarification, and purification.

Keywords: Adeno-associated virus (AAV), biomanufacturing, bioproduction, purification

3.1. Introduction

Since adeno-associated virus (AAV) was first identified in 1965, hundreds of variants have been isolated from adenovirus stocks or primate tissues [90]. Different serotypes of AAV1-10 could preferentially transduce or induce specific types of cells or tissues, enabling organ-based gene delivery [91-93]. Various recombinant AAVs (rAAVs) have been constructed to transduce a wide range of living cells (dividing and non-dividing) and deliver genes of interests [94,95]. rAAV constitutes 20–25-nm non-envelop protein capsid (virion protein 1 [VP1], VP2 and VP3) and < 4.9-kb genome of single-stranded DNA (ssDNA), including the gene of interest, flanked by inverted terminal repeats [96,97]. Novel engineered chimeric AAV capsids, such as AAV-DJ, -DJ8 and others, have been constructed by Kay [98], Samulski [99] and Schaffer [100] Laboratories to escape AAV neutralization by pre-existing serum antibodies, increase *in vivo* infection efficiency, and enhance circulation stability.

Several AAV-mediated gene therapies [101,102], including Glybera (AAV1 delivering S447X, withdrawn from market) for lipoprotein lipase deficiency treatment, Roctavian (AAV5 carrying clotting factor VIII) for adults with severe hemophilia A, Hemgenix (AAV5 delivering clotting factor IX) for hemophilia B, Luxturna (AAV2 carrying functional RPE65 gene) to treat inherited retinal disease, Zolgensma (AAV9 carrying SMN1) for children below two years old with spinal muscular atrophy, and Elevidys (AAV delivering micro-dystrophin protein) for ambulatory pediatric patients, have been approved so far. As compared to conventional nanoparticle-mediated gene delivery vehicles, rAAV has advantages of high infection rate, long-term transgene expression, low immunogenicity,

and minimal toxicity in clinical applications [90,103,104]. Over 130 AAV-delivered gene therapies have been evaluated in clinical trials during last two decades [105] and hundreds of clinical trials are on-going to treat Alzheimer, Parkinson, and other diseases [106-109]. Due to the promising clinical and pre-clinical achievements of these gene therapies, an advanced AAV biomanufacturing procedure with high productivity, quality and recovery rate for multiple serotypes is highly needed.

Literature has reported several suspensive bioproduction processes of AAV expression vectors using HEK cells and triple-plasmid transfection [110]. For instance, Daniel et al. have reported a polyethylenimine (PEI)-mediated transfection of suspensive HEK 293 cells to produce AAV2/8 and AAV2/9 carrying green fluorescent protein (GFP) with titer of 2×10^8 vg/mL at 10–30 mL scale [111]. The purification procedure using iodixanol gradient ultracentrifugation and immunoaffinity chromatography with POROS CaptureSelect resin has generated recovery rate of 35.6% and 17.9%, respectively. Grieger et al. have well adapted HEK 293 cell in suspension culture, transfected with three plasmids and PEI Max, and produced AAV serotypes 1–6, 8 and 9 in 30-mL shaker flask culture and 2 or 4-L WAVE bioreactor culture with titer of $0.9–3.5 \times 10^{10}$ vg/mL [112]. The ion exchange purification using 5-mL HiTrap Q HP column generated rAAV with purification recovery of 39–49%. In another study, the suspensive HEK 293 T cells have been transfected with PEI Max and three plasmids to generate AAV serotypes of 1, 2, 5, 8 and 9 in 30-mL or 1-L shaker flask cultures, which achieved final titer of $> 1 \times 10^{11}$ vg/mL [113]. The affinity purification using AVB-Sepharose with POROS CaptureSelect has yielded an estimated recovery of 27.9–76.9%. In our previously developed AAV biomanufacturing process,

suspensive HEK 293F cells and PEI transfection reagent or liposomes produced up to 7.86 × 109 vg/mL of chimeric AAV-DJ8 in 30–450 mL of shaker flask or spinner flask cultures [114]. To meet the increasing demand of clinical materials, a more advanced biomanufacturing platform with high AAV productivity and recovery rate is needed.

This study aimed to develop a robust and scalable biomanufacturing platform to produce AAVs in stirred-tank bioreactor, purify various AAV serotypes using liquid chromatography, and improve overall recovery rate in the procedures of clarification, purification and post-purification operations. The effects of host cell, key transfection parameters (e.g., viable cell density, transfection reagent, ratio of plasmid DNA: cell), production scale, clarification strategy, purification column with different loading and elution conditions, and desalting and concentration method were evaluated and compared. Importantly, this study evaluated the scale-up robustness of our developed bioproduction and purification processes, which is essential to adapt it from Good Laboratory Practice (GLP) to future Good Manufacturing Practice (GMP) production. The generated AAVs were fully evaluated in terms of capsid protein expression, morphology, transduction capability, tissue-specific infection, and functional expression of delivered gene. The advanced AAV biomanufacturing reported in this study could benefit the future GMP production of multiple AAV serotypes and their further pre-clinical and clinical evaluations.

3.2. Results and discussion

3.2.1. Advanced biomanufacturing of AAV

The process flow diagram (PFD) of an advanced AAV biomanufacturing was developed in this study, including suspensive production, bioproduction scale up, clarification, liquid chromatography purification and scale up, post-purification process, storage and evaluations (Fig. 7). The AAV production process development was performed in shaker flasks at scale of 30–100 mL and in spinner flasks with 60–100 mL of cultures. The production process in 1.2–2.0 L of stirred-tank bioreactors with process parameter control could be applied to pilot plant production and possible large-scale manufacturing production. As detailed later, the key production parameters identified in this study include host cell selection, transfection condition, and agitation speed. Two-step universal separation process using anionic exchange chromatography and ultrafiltration has been developed to purify multiple AAV serotypes. The post-purification desalting and concentration procedures have also been investigated. This study reported an advanced generic AAV biomanufacturing process of production, clarification and purification. Importantly, the developed platform is robust, scalable, and applicable to cover multiple (if not all) serotypes.

3.2.2. Development of suspensive AAV production and clarification

We first compared two suspensive host cells, i.e. HEK 293F and VPC, in shaker flask production at 37 °C, 8% CO2 and 125 rpm. Both seed and production cultures showed that VPC cells had significantly lower cell clumping than HEK 293F. The VCD of VPC reached > 4.0 × 106 cells/mL on Day 1 post transfection, followed with VCD and viability

dropping to ~ 3.4 × 106 cells/mL and 82% and AAV-DJ8 titer increased significantly from Day 2 (Fig. 8). AAV was harvested at 72 h post transfection with VCD of 2.8×10^6 cells/mL and cell viability of 70–80% in shaker flask. The dynamic production profile revealed a significant increase of AAV titer from Day 2 to Day 3. Similar cell growth and AAV productivity were observed in the productions of AAV2, AAV5 and AAV-DJ (cell culture profiles not shown). As summarized in Table 1, the volumetric productivity of AAV-DJ8 using the same triple plasmids, pAAV-NLuc-GOI (~ 3.9 kb), pAAV Rep-Cap and pHelper, was $0.50–0.53 \pm 0.08 \times 10^{10}$ vg/mL by HEK 293F and $2.40 \pm 0.06 \times 10^{10}$ vg/mL by VPC cells under respective optimal transfection conditions. It is obvious that VPC produced about 5-fold higher AAV in shaker flask than HEK 293F. Therefore, the process development and scale up in this study used VPC.

Our previous study showed that the cell density at the time of transfection and amount of plasmid DNA are other two key transfection parameters to improve AAV production [114]. Therefore, we evaluated the effects of cell density at the time of transfection (2.0, 3.0, and 4.0×10^6 cells/mL) and ratio of total plasmid DNA/VPC cells (0.4, 0.5, and 0.6 μg/million cells) in shaker flask productions. As presented in Fig. 8A and B, the optimal transfection VCD is 3.0×10^6 cells/mL and plasmid DNA: VPC ratio is 0.5 μg: 10^6 cells, which generated final AAV titer of $5.6–10.0 \times 10^{10}$ vg/mL. Therefore, our scaling up evaluation and purification development studies used the optimal transfection VCD and plasmid DNA amount identified here.

Then the optimal suspensive production process was validated with four AAV serotypes, using pAAV2, 5, DJ and DJ8 Rep-Cap, expression vector with ~ 3.9 kb of inserted genes and pHelper, in shaker flask and/or bioreactor cultures at the developed conditions. The optimal transfection formulation, i.e. pAAV expression: pAAV Rep-Cap: pHelper ratio of 1:3:1, DNA: cell ratio of 0.5 μg:1 million cells, 10% viral-plex buffer and 0.6% AAV-MAX transfection reagent, and supplement of 0.3% booster and 1% enhancer, was applied. The qPCR titration of intracellular AAV showed similar range of productivity of 7.88 ± 0.39, 2.97 ± 0.13, 2.40 ± 0.06, and $5.60 \pm 5.14 \times 10^{10}$ vg/mL for AAV2, AAV5, AAV-DJ8, and AAV-DJ, respectively (Table 1). These results demonstrated that the suspensive AAV production process can be used to generate multiple serotypes.

Furthermore, we investigated and compared several raw AAV clarification strategies, including direct lysis of cell culture broth and lysis of cell pellets after centrifugation. The direct lysis by adding AAV-MAX lysis buffer and other supplements (MgCl2 and benzonase) and incubating the lysis mixture at 37 °C was time-consuming (2–6 h), and also had poor cell lysis efficiency in some batches which could be caused by culture variations. Then we tested the strategy of centrifugation to collect cell pellets followed with two lysis options as detailed in Section “AAV clarification”. Our results demonstrated that both strategies, i.e. incubation at 37 °C and repeated freeze–thaw cycles, achieved 95–100% VPC lysis. The lysis of culture broth enables direct collection of raw AAV from most productions tested in this study, but cell pellet lysis could achieve high AAV release efficiency (as confirmed with cell lysis rate), reduce lysis reagent amount and simplify clarification operation in bioreactor-based production.

3.2.3. Bioproduction scale-up

Before scaling up shaker flask production process to stirred-tank bioreactor, AAV production was evaluated in 250-mL spinner flask with working volume of 60–100 mL. The agitation speeds of 75, 100, 125 and 150 rpm were tested. The low agitation speed caused significant cell aggregation and shortened culture longevity. The AAV productions in spinner flask presented in Table 1 were performed at 37 °C, 210 rpm and 8% CO2. As compared to shaker flask, spinner flask production reached maximal VCD of 4.3–4.6 × 106 cells/mL on Day 2 and VPC cells containing AAV were harvested at viability of 70–80% (Fig. 9). Similar to shaker flask cultures, AAV titer was significantly increased from Day 2 to Day 3 in spinner flask. It was observed that spinner flask production was less than 20% of that in shaker flask, i.e., 0.41 vs 2.40×10^{10} vg/mL. These results suggested that the suspensive transfection and AAV production in stirred tank is feasible, but the process parameters need further optimization for high productivity.

Next, we investigated the process scale up to stirred-tank bioreactor using seed cultures from shaker flask or spinner flask. Both strategies showed similar cell growth and AAV production, so all bioreactor productions presented in this study used shaker flask seed cultures. As shown in Fig. 10, the maximal VCD reached 6.15×10^6 cells/mL (AAV-DJ8) or 7.60×10^6 cells/mL (AAV-DJ) and harvest viability was about 90–95% (AAV-DJ8) or 80–85% (AAV-DJ) at 72 h post triple-plasmid transfection, which had different cell growth kinetic profile from those in shaker flask and spinner flask. The production titers of $8.14 \pm 1.91 \times 10^{10}$ vg/mL for AAV-DJ and $7.52 \pm 0.49 \times 10^{10}$ vg/mL for AAV-DJ8 were obtained on Day 3 in 1.2–2-L bioreactor production at 37 °C, pH 7.0, 210 rpm and DO

40%. It is clear that VPC cell growth was enhanced by ~ 50% and AAV titer was improved by > 100% in stirred-tank bioreactor as compared to shaker flask (Table 1). These process-scaling up data demonstrated that our AAV production process was robust and scalable in bioreactors, which is important to future industrial productions to support clinical trials or potential clinical applications.

3.2.4. Purification development and scale-up

Multiple commercial columns for AAV purification have been evaluated in this study (Table 1), including Cytiva HiTrap Q Sepharose XL strong anion exchange column, Cytiva Sepharose Fast Flow anion exchange column, Cytiva HiTrap AVB Sepharose column, Bio-Rad Foresight Nuvia HPQ column, and Bio-Rad EconoFit Nuria aPrime 4A. The primary purification method using NGC liquid chromatography equipped with these columns were developed.

As shown in Fig. 11, aPrime 4A column achieved purification recovery of > 85% using equilibration buffer A (25 mM Tris–HCl, 20 mM NaCl, pH 9.0) and elution buffers of A and B (25 mM Tris–HCl, 1 M NaCl, pH 9.0). Linear elution (0 ➔ 100% increase of buffer B) in aPrime 4A column did not well separate AAV from other peaks (data not shown). The stepwise elution (0, 15, 25, 70, 85 and 100% of buffer B) at flow rate of 1.0 mL/min well separated AAV peak from other impurities, with high binding rate of 85–95% and elution rate of ~ 100%, using 1-mL aPrime 4A column and pellet lysate from 20-mL culture (Fig. 11A). The binding rate was calculated by titrating raw AAV samples and flow through collection. We further increased the loading amount of raw AAV by using pellet

lysate from 100-mL culture in 1-mL aPrime 4A column, which showed that the AAV binding rate was reduced to < 80% although the binding amount was significantly increased (Fig. 11B). The representative chromatography profile of AAV-DJ8 was described in Fig. 11, but four serotypes of AAV2, 5, DJ and DJ8 were tested using the same column, loading and elution conditions, which did not show obvious difference in binding and elution. These results confirmed the robustness and scalability of our primary AAV purification using IEX. Small amount of AAV was detected in flow through and other elution peaks from aPrime 4A column. Further optimization of sample loading and elution conditions (e.g. flow rate and stepwise strategy of buffer B) might be able to increase the overall purification recovery rate.

The stepwise elution (0, 50, 65 and 100% of buffer B) of raw AAV lysis from 20-mL pellet using 1-mL HPQ column showed lower binding and overall recovery rate of 40–60% (Fig. 11C) than aPrime 4A. Furthermore, we scaled up the purification process to a 5-mL pre-packed commercial HPQ column, loaded with AAV lysis from 50-mL pellet (Fig. 11D), and to an in house packed 25-mL column using the same Nuvia HPQ media. The similar binding rate, elution profile and recovery rate were observed in both 5-mL and 25-mL HPQ columns while significant (~ 50%) amount of AAV was detected in flow through and other elution peaks using HPQ column.

The evaluations of other commercial columns showed that the Q Sepharose IEX column had low AAV binding rate (< 5%) and AVB Sepharose affinity column showed weak binding rate (< 5%) of AAV2 and DJ8 using the manufacturer provided purification

parameters as detailed in Section “AAV purification”. Taken together, the IEX purification using aPrime 4A column with stepwise elution was identified as the optimal primary purification in this study although further development and optimization is needed in future. The secondary purification using ultrafiltration and other strategy such as G25 column or dialysis was tested to concentrate and desalt (i.e. buffer exchange) the purified AAV. The AAV2, 5 and DJ8, which were filtered, concentrated and washed with PBS using 100 kDa MWCO PES column following manufacture procedure, showed high recovery rate (> 90%). However, the AAV-DJ elute from IEX column blocked PES column, and 100 kDa MWCO regenerated cellulose column was identified as a suitable column to ultrafiltrate AAV-DJ with high recovery rate of 90%. The alternative strategies are to combine desalting operation using HiTrap G25 column equipped in liquid chromatography system following the manufacture protocol or 20 kDa dialysis cassette with additional ultrafiltration concentration or refrigerated vacuum concentrator. The purified AAVs were aliquoted in formulation buffer of 1 × PBS, 5% Sorbitol and 350 mmol/L NaCl, and stored at -80 °C for long term.

3.2.5. Quality evaluations of produced AAV

Although the developed biomanufacturing process was validated using four serotypes of AAV, the AAV-DJ8 was applied in the following characterizations or evaluations. To characterize the AAV-DJ8 produced from our developed bioprocess, SDS-PAGE was performed with silver staining and detected three capsid proteins, 87-kDa VP1, 73-kDa VP2 and 62-kDa VP3 (Fig. 12A). Western blotting was carried out to analyze the purified AAV, which confirmed the integrity and expression of all three capsid proteins (Fig. 12B).

Moreover, TEM image confirmed the right size and morphology of AAV (Fig. 12C). In addition to high productivity and recovery, transduction capability of functional AAV was also evaluated using live-cell imaging. As described in Fig. 13, glioblastoma U251 cells (green color, GFP labelled) were transduced with Cy5.5-labelled AAV-DJ8 (red color), and confocal microscope imaging demonstrated that AAV accumulated around the DAPI-stained nucleaus (blue color) within 24 h post incubation. These images revealed that our AAV could effectively transduce cells *in vitro*.

The *in vivo* AAV induction and functional expression of AAV-delivered gene were tested by intracranially injecting 1×10^{10} vg of AAV-DJ8 into the glioblastoma U251 xenograft NSG mouse models. As described in Fig. 14A, the NLuc gene was delivered to glioblastoma tumor and functionally expressed to generate bioluminescence *in vivo* with induction of ViviRen (37 μg, intravenous injection), as detected by live-animal IVIS imaging. This result also confirmed the gene expression in tumor only facilitated with the tumor-specific promoter in AAV expression vector [114]. It was observed that the *in vivo* NLuc bioluminecence lasted 1–2 h post injection of substrate ViviRen.

Furthermore, we transduced 5×10^4 cells of U251 that were seeded in 96-well plates with AAV-DJ8 at MOIs of 0, 1,000, 2,500, 5,000, and 7,500. Neither MOI of 0 (25 μM of ViviRen only) nor 1,000 generated bioluminescence signals while MOIs of 5,000 and 7,500 had strong bioluminescence (Fig. 14B). Higher MOI of AAV generated stronger bioluminescence than lower MOI in 6-well plate cultures. The dynamic SpectraMax iD3 profiles showed that the bioluminescence signal decreased to minimal levels within 25 min

post induction *in vitro* (Fig. 14C). All these characterization and evaluation data demonstrated that our new biomanfuacturing process generated high-quality AAVs.

3.2.6. Advantages of our AAV biomanufacturing process

This study developed a novel AAV biomanufacturing procedure with multiple advantages as compared to previously reported production processes. First, high productivity can be achieved in the stirred-tank bioreactor-based production. Second, the developed process is robust and scalable to large-scale biomanufacturing for future pre-clinical and clinical trials. Third, good-purity AAV was generated using the identified ion-exchange columns and developed purification protocols. Fourth, the good-quality AAV produced from the developed process can be used *in vitro* and *in vivo* without detected side effects such as fever or immune toxicity. Most importantly, the developed universal biomanufacturing process can be applied to produce and purify different serotypes of AAV (AAV2, 5, DJ and DJ8 in this study).

3.2.7. Prospective AAV biomanufacturing

This study developed a scalable suspensive AAV production process by evaluating host cell and transfection parameters. The Viral Production Cell (VPC) 2.0 engineered from parental HEK 293F cells by Gibco, which has larger cell size, faster cell growth, and minimal cell clumping at optimal shaking or agitation condition, was applied and enhanced AAV titer by 5 folds as compared to HEK 293F [114]. Compared to adherent HEK 293AAV or 293A, the VPC-based AAV production process is robust and easy to scale up in bioreactor. Moreover, this host cell showed high resistance to shear force and could directly

inoculate the production medium in bioreactor using the seed cultures from shaker flask without any adaptation.

One of the key parameters in AAV production using VPC was the agitation speed. For instance, low agitation could increase cell clumping, reduce cell growth, and decrease AAV production significantly. The high agitation speed of 210 rpm enabled high AAV production and minimal cell aggregation.

Another important parameter is the high consumption of glucose and GlutMAX due to the fast cell growth and high AAV productivity. In the biomanufacturing process developed in this study, the same basal medium was used from Day -1 when seeding the production bioreactor until the end of AAV harvest without medium exchange or culture dilution. The batch culture of AAV production showed significant cell viability dropping on Day 2 (data not shown). The booster and enhancer added during transfection could extend the culture longevity and maintain high viability. However, it was found that more than 8.2 g/L of glucose was consumed from Day -1 to Day 3. Lack of assay to titrate GlutaMAX in culture broth, we assumed the 1:1 consumption rate of glucose and GlutaMAX and fed 3.5 mM of GlutaMAX together with ~ 3.5 g/L of glucose between Day 1 and Day 2 to avoid nutrient depletion in this study. To further optimize AAV production, a full extracellular and intracellular metabolite analysis is needed to monitor glucose and GlutaMAX consumption and correlate cellular metabolism to cell growth and AAV production.

In the presented AAV bioproduction, we stopped culture at 72 h post triple-plasmid transfection, but AAV-DJ did not reach maximal value at the harvest viability. Therefore, we suspected that AAV titer could be further improved by optimizing the endpoint of production process via evaluating different harvest viabilities.

3.2.8. Further optimization of AAV purification

The challenge in the purification of engineered AAV capsids is the lack of a high specificity of binding resin with high capture rate. The generic IEX column separation developed in this study can be applied to multiple AAV serotypes, but the purity could be lower than the affinity column purification. To further improve the purity of AAV, affinity-based primary capture and purification followed with secondary or polishing strategies could be developed in future to benefit the recovery and purity of multiple AAV serotypes.

In addition, the primary purification using IEX aPrime 4A liquid chromatography column captured 85–95% AAV in one round of sample loading. To achieve higher capture rate, the loading capacity, flow rate of loading buffer, and packing strategy of purification resin should be further optimized. Another strategy is to run serial purification using both aPrime 4A and HPQ columns to improve the binding rate of AAV.

Ultrafiltration could further purify the AAV post IEX purification by removing the impurities with molecular weight of < 100 kDa, and combine desalting, buffer exchange and sample concentration into one step. However, we observed that AAV-DJ had high retention rate in PES membrane but showed high recovery in regenerated cellulose column.

Evaluation and selection of suitable ultrafiltration material might be needed for different serotypes. An alternative strategy is to use G25 desalting column or dialysis in combination with vacuum concentration to process the purified AAV, but the multi-step operation could reduce the recovery rate of AAV.

3.3. Conclusions

AAVs have been widely used to deliver therapeutic genes for disease treatment or deliver the genes of interest for long-term transient expression in basic research due to the advantages of high infection and stable transient expression. This study reported a robust, scalable and suspensive biomanufacturing of multiple AAV serotypes, including stirred-tank bioreactor production and scale up to achieve high productivity, liquid chromatography purification and scale up to get high recovery rate, and post purification handling and evaluation of AAV quality. As compared to previously established AAV bioprocess, this advanced biomanufacturing can be easily adapted to GMP facility for large-scale production and purification. Moreover, this generic biomanufacturing can be used to produce and purify AAVs with different serotypes although fine adjustment or modification is needed. In addition to the high productivity and high recovery, the generated AAV demonstrated high function and quality. In conclusion, the biomanufacturing platform developed in this study could benefit the production, clarification and purification of AAV for basic research, pre-clinical study, translational research or clinical application.

3.4. Materials and methods

3.4.1. Triple plasmids for AAV construction

The AAV2, 5, DJ and DJ8 serotype-specific Rep-Cap plasmids, pHelper plasmid, and AAV-MCS Promoterless Expression Vector were purchased from Cell Biolabs (San Diego, CA, USA). The CMV promoter, luciferase reporter gene (Luc) and synthesized gene of interest (total of 3.9 kb) [114,115] were cloned to construct pAAV expression plasmid following our previous publication [114]. These triple plasmids were used to transfect host cells for AAV production and evaluations in this study.

3.4.2. Cells, media and cultures

All AAV producing host cells, culture media and nutrients were purchased from Gibco (Buffalo, NY, USA) and general supplies were purchased from Fisher Scientific (Waltham, MA, USA) unless otherwise specified. The Viral Production Cells 2.0 (VPC, Gibco, USA) were engineered and cloned from parental cell line HEK 293F, then well adapted to chemically defined Viral Production Medium. The seed train of VPC cells were cultivated in basal production medium supplemented with 4 mM of GlutaMAX in 125 or 250-mL shaker flasks at 125 rpm on an orbital shaker (Thermo Fisher Scientific, Waltham, MA, USA) with 19-mm shaking diameter. HEK 293F cells were grown in FreeStyle 293 Expression Medium with 4 mM of GlutaMAX in shaker flasks at the same conditions of VPC cells. The small-scale (30 or 60 mL) VPC or HEK 293F host cells were maintained at 37 °C, 8% CO2 and 125 rpm in CellXpert™ incubator (Eppendorf, Enfield, CT, USA) for AAV production. The human glioblastoma cell line U251 (MilliporeSigma, Burlington, MA, USA) was cultivated in DMEM/F12 medium with 10% fetal bovine serum, 4 mM L-

glutamine, 1% non-essential amino acids (NEAA), 1 mM sodium pyruvate, and 1% penicillin/streptomycin (100 IU/100 µg/mL) in T-75 flask at 37 °C and 5% CO2 [116]. The U251 cells were used for *in vitro* AAV transduction evaluation, gene expression analysis, and glioblastoma intracranial xenograft mouse model development for *in vivo* evaluations. The cell growth was monitored in terms of viable cell density (VCD) and viability using TC20 automated cell counter (Bio-Rad, Hercules, CA, USA).

3.4.3. AAV production in shaker flask, spinner flask and bioreactor

AAV production using HEK 293F: As described in our previous study [114], HEK 293F host cells were transfected with three plasmids with plasmid DNA: HEK 293F ratio of 1.6 µg:10^6 cells, cationic liposomes as transfection reagent, and VCD of 0.4×10^6 cells/mL. The transfection liposomes were synthesized using 1,2-dioleoyl-sn-glycero-3-phosphoethanolamine and 1,2-dioleoyl-3-trimethylammonium-propane [89]. The suspensive AAV production was carried out in 30 mL of culture using 125-mL shaker flask at 125 rpm, 37 °C and 5% CO2, or 100 mL of culture using 250-mL spinner flask at 210 rpm, 37 °C and 5% CO2. Raw AAV was harvested from the transfected HEK 293F cells at 40–60 h post transfection for further clarification and purification.

AAV production using VPC: The viral production medium supplemented with 6 g/L of glucose and 4 mM of GlutaMAX was inoculated with VPC cells at a seeding VCD of 1.5×10^6 cells/mL and incubated for 24 h to reach a VCD of about 3.0×10^6 cells/mL before transfection. The key optimized transfection parameters include VPC density of 3.0×10^6 cells/mL, pAAV expression plasmid: pAAV Rep-Cap: pHelper of 1:3:1, DNA: cell of 0.5

μg:1 million cells, 10% (v/v) viral-plex buffer, 0.6% AAV-MAX transfection reagent, 0.3% booster, and 1% enhancer (Gibco). Interestingly, the VPC cells showed poor growth in bioreactor at agitation speed of 130 rpm but reached high VCD and viability when the agitation was increased to 210 rpm. The AAV production process was evaluated at different scales: 1) 30 or 60 mL in 125 or 250-mL shaker flask at 37 °C, 125 rpm using shaker with 19-mm shaking diameter and 8% CO2, 2) 60–100 mL in 250-mL spinner flask at 37 °C, 210 rpm and 8% CO2, and 3) 1.2–2.0 L of working volume in 2.5-L stirred-tank bioreactor (Distek, North Brunswick Township, NJ, USA) with process controls of 37 °C, pH 7.0, 210 rpm and DO 40%. VPC cells were harvested at 72 h after transfection using centrifugation at 1,000 g for 10–20 min at 4 °C and cell pellets were stored at -80 °C for further purification and characterization.

3.4.4. AAV clarification

The VPC cells were re-suspended in PBS buffer with 1/30 of the production volume, then raw AAV was released by adding 10% AAV-MAX lysis buffer (Gibco), 2 mM $MgCl_2$ and 90 U/mL benzonase (Millipore Sigma). An alternative strategy was to directly lysis cell culture broth using the same formulation. The lysis mixture was incubated at 37 °C for 2–3 h on an orbital shaker or operated with three cycles of freeze in ethanol/dry ice for 30 min and thaw at 37 °C in water bath for 15 min. After a full cell lysis was confirmed with observation under microscope, the cell lysate was centrifuged at 13,000 g for 10 min or 4,500 g for 30 min at 4 °C. The supernatant containing AAV particles was collected and filtered by 0.45 μm and 0.22 μm regenerated cellulose membrane (serotype of DJ) or PES membrane (serotypes of 2, 5 and DJ8) to remove cell debris for clarification.

3.4.5. AAV purification

Bio-Rad NGC system equipped with four chromatography columns, including EconoFit Nuvia aPrime 4A ion exchange (IEX, anionic) column (Bio-Rad), Foresight Nuvia HPQ anionic column (Bio-Rad), HiTrap Q Sepharose XL anionic column (Cytiva, Marlborough, MA, USA), and HiTrap AVB Sepharose affinity column (Cytiva), for AAV purification. Among these columns, aPrime 4A anionic column achieved high recovery rate and purity for all four serotypes with equilibration buffer A (25 mM Tris–HCl, 20 mM NaCl, pH 9.0) and stepwise (0, 15, 25, 70, 85 and 100%) elution buffers of A and B (25 mM Tris–HCl, 1 M NaCl, pH 9.0) at flow rate of 1.0 mL/min. HPQ anionic column-based purification procedure generated medium level of recovery rate and purity of all four serotypes using equilibration buffer A (25 mM Tris–HCl, 20 mM NaCl, pH 9.0) and gradient (stepwise, 0, 50, 65 and 100%) elution buffers of A and B (25 mM Tris–HCl, 1 M NaCl, pH 9.0) with flow rate of 1.0 mL/min. The equilibration buffer of 20 mM Tris–HCl, 0.5 M NaCl, pH 8.0 and elution buffer of 0.1 M Glycine–HCl, 0.5 M NaCl, pH 2.5 with flow rate of 0.5 mL/min were used for HiTrap AVB Sepharose column. The HiTrap Q Sepharose anionic column was used for AAV purification with loading buffer of 25 mM Tris–HCl, pH 9.0 and elution buffer A of 25 mM Tris–HCl, pH 9.0 and buffer B of 2 M NaCl in 25 mM Tris–HCl, pH 9.0 with flow rate of 1.5 mL/min. The primarily isolated AAV was further purified using 100 kDa MWCO PES ultrafilter (AAV2, 5 or DJ8) or regenerated cellulose ultrafilter (AAV-DJ) to remove the small-size impurities. Then the purified samples were desalted using HiTrap G25 desalting column (Cytiva) with NGC liquid chromatography system (Bio-Rad) or 20 kDa MWCO slide-A-lyzer dialysis cassettes through buffer exchange. Finally, the AAV samples were concentrated using Savant SpeedVac (Fisher), or 10-kDa

regenerated cellulose concentrator for AAV-DJ or PES concentrator for AAV 2, 5 and DJ8. The purified, desalted and concentrated AAV was sterilized using 0.22 μm filter, then stored in a formulation buffer composed of 1 × PBS, 5% Sorbitol, and 350 mmol/L NaCl at -80 °C for long-term storage.

3.4.6. AAV titration

The AAV samples collected from raw cell lysate, post purification using ion exchange columns and ultrafilters, and post desalting and concentration were aliquoted and diluted with PBS for qPCR titration. First, the possible nucleotide contaminant was removed from the single-stranded AAV DNA by mixing 5 μL of AAV sample with 5 μL of DNase I Buffer (10X), 100 U of DNase I (336 U/μL), 1 U of Exonuclease I (20 U/μL), and UltraPure DNase/RNase-free distilled water (Gibco) in a 50-μL mixture. The digestion reaction was processed in a thermal cycler at 37 °C for 60 min, 85 °C for 20 min, and 4 °C until stop. The AAV samples digested with DNase were further processed to remove protein contaminant by adding 1 μL of Proteinase K and 49 μL of Proteinase K buffer (2X), followed with incubation in thermal cycle at 60 °C for 60 min, 95 °C for 10 min, and 4 °C until stop. The extracted ssDNA samples were 1:50 diluted with DNase/RNase-free distilled water. Second, the pAAV expression plasmid containing NLuc was linearized to prepare standard samples by serially diluting it to gene copy of 2×10^8, 10^7, 10^6, 10^5, 10^4 and 10^3 per μL in Eppendorf tubes with DNase/RNase-free distilled water. Third, the qPCR reaction was prepared by mixing PowerUp SYBR Green Master Mix (Applied Biosystems, Waltham, MA, USA), 250 nM of NLuc forward primer (5'-ATTGTCCTGAGCGGTGAAA-3') and reverse primer (5'-

CACAGGGTACACCACCTTAAA-3'), and UltraPure™ DNase/RNase-Free Distilled Water to reach volume of 15 μL each reaction. Fourth, 5 μL of AAV samples or standard samples were added into 96-well plate (Avantor, Radnor, PA, USA), followed with adding 15 μL of qPCR reaction mixture into each well. The 96-well plate was covered with an adhesive film and spin down with centrifugation at 1000 g for 1 min. The qPCR assay was performed in an Azure Cielo 96-well Real-Time PCR instrument (Azure Biosystems, Dublin, CA, USA) at 50 °C for 2 min, 95 °C for 2 min, and 40 cycles at 95 °C for 15 s and 60 °C for 1 min. Finally, the fluorescence was measured at 60 °C and data analysis was implemented by the Azure Cielo manager software (Azure Biosystems) to calculate the copy number of vector genome (vg).

3.4.7. SDS-PAGE and Western blotting

NuPAGE 4–12% Bis–Tris protein gels (Life Technology, Carlsbad, CA, USA) were used to run non-reducing SDS-PAGE to characterize AAV. The gels were stained with Pierce Silver Stain Kit (Fisher) and imaged by Azure 300 biosystems (Azure Biosystems). To confirm the expression of capsid proteins of the produced AAV, the primary rabbit polyclonal anti-VP1/2/3 antibodies ordered from American Research Products Inc (Waltham, MA, USA) and HRP-conjugated secondary anti-rabbit antibody (Abcam, Cambridge, UK) were used for the immunodetection of VP1 (87 kDa), VP2 (73 kDa) and VP3 (62 kDa). The blotted PVDF membrane was treated with Luminata Forte Western HRP substrate (Millipore, Boston, MA, USA) and imaged by Azure 300 biosystems following our previously established protocol [117-119].

3.4.8. Live-cell confocal imaging

The three-color confocal microscope imaging was performed to confirm the transduction capability and biological function of produced AAV following our previously reported procedure [120-122]. Specifically, the purified AAV was stained with Sulfo-cyanine 5.5 (Cy5.5) fluorescent dye (Lumiprobe, Cockeysville, MD, USA) following the manufacturing protocol. The unlabeled free dye was removed using 100 kDa MWCO PES concentrator using PBS with dilution factor of 1:10 for 5 times. The chambered glass coverslip was seeded with glioblastoma U251 cells at cell density of 1×10^5 cells/mL, stained with BacMam GFP (Fisher) for cytoplasm detection, and incubated at CO2 incubator for overnight. The U251-GFP cells were stained with DAPI to image nucleus and transduced with AAV-Cy5.5 at multiplicity of infection (MOI) of 5,000 for 24 h. After washing out the free AAV and dye, the live-cell confocal images of stained U251 were captured using Echo Revolve fluorescent microscope (Echo, Cerritos, CA, USA) with fluorescent light cubes of FITC, DAPI and Cy5 to detect GFP, DAPI, Cy5.5, respectively. The transduction of AAV was evaluated by the overlap of green GFP (U251 cells), blue DAPI (nucleus), and red Cy5.5 (AAV).

3.4.9. Transmission electron microscope (TEM) imaging

TEM images of AAV particles were collected following our previous procedure with modification [123]. Our AAV samples (3 μL) were negatively stained with 2% uranyl acetate on the glow discharged carbon grid purchased from Electronic Microscope Sciences (Hatfield, PA, USA) and incubated at room temperature for 1–2 min, followed with blotting off the stain. Tecnai F20 XT transmission electron microscope (Field Electron and

Ion Company, Hillsboro, OR, USA) equipped with three CCD camera was used to collect images of AAV. Briefly, the AAV samples were loaded in DT rod first. Then both microscope alignment and fine alignment of gun and aperture were performed or confirmed before recording images. Finally, Gatan digital micrograph was captured with the WA-Orius camera.

3.4.10. Xenograft model

The 6-week-old NSG (NOD.Cg-Prkdc < scid > Il2rg < tm1Wjl > /SzJ) mice (Jackson Laboratory, Bar Harbor, ME, USA) were used to generate glioblastoma orthotopic xenografted model following our previously established protocol [116,124] with modification and approved IACUC protocol. Briefly, about 0.5×10^6 U251 cells suspended in 3 µL of sterile saline buffer were intracranially implanted into the frontal region of cerebral cortex (2 mm lateral, 1 mm anterior and 1.5 mm ventricle of bregma) at rate of 0.4 µL per minute using Stoelting Just for Mouse Stereotaxic Instrument (Stoelting, Wood Dale, IL, USA). The burr hole in skull was closed with sterile bone wax deposited by rubbing wax back and forth from the wooden end of a sterile cotton-tipped applicator. The NSG mice received 5 mg/kg of carprofen via subcutaneous (s.v.) injection immediately before surgery and every 12–24 h for 48 h post-surgery. Bupivacaine stock of 2.5–5 mg/mL was topically administered with dosage of 1 mg/kg at the incision site during surgery.

3.4.11. IVIS and bioluminescent imaging

The functional expression of AAV-delivered NLuc gene was tested *in vitro* using U251 cell line and *in vivo* using U251 cell line-derived intracranial xenografted NSG mouse

model, respectively. For *in vitro* evaluation, 5×10^4 cells/mL of U251 cells were used to seed 96-well plates and transduced with AAV at different MOIs, i.e. 1,000 to 7,500. Then 25 μM of substate ViviRen (Fisher) was added to the cells expressing AAV-delviered genes three days after transduction. The bioluminescence generated by the expressed NLuc protein was monitored with In Vivo Imaging System (IVIS) Lumina Series III (PerkinElmer, Waltham, MA, USA) [121]. The 6-well plate was seeded with 5×10^5 cells/mL of U251 cells, transduced with AAV at different MOIs of 0, 1×10^4 and 1×10^6, and induced with 25 μM of substate ViviRen. The dynamic bioluminescence signal was detected with SpectraMax iD3 plate reader (Molecular Devices, San Jose, CA, USA). To detect *in vivo* expression of AAV-delivered NLuc gene, the U251 xenografted NSG mice received 1×10^{10} vg of AAV and 37 μg of ViviRen substrate through intracranial injection at the same coordinate of cells xenograft. The NLuc expression (i.e. bioluminescence) was detected in live animals using IVIS Lumina.

3.4.12. Statistical analysis

All experimental data were presented as average ± standard deviation (STDEV) with replication number of 3. Two-tailed Student's t tests with statistical significance of P value < 0.05 were used to determine the probability of significance between conditions.

Funding

This research was funded by the United State (US) National Institutes of Health under Cooperative Agreement Numbers of R01CA262028-01A1 and NHLBI R01HL156581, issued by National Cancer Institute, American Heart Association under Agreement

Number of 906423, and Department of Defense under Cooperative Agreement Numbers of W81XWH2110066 and W81XWH2110067.

Figures

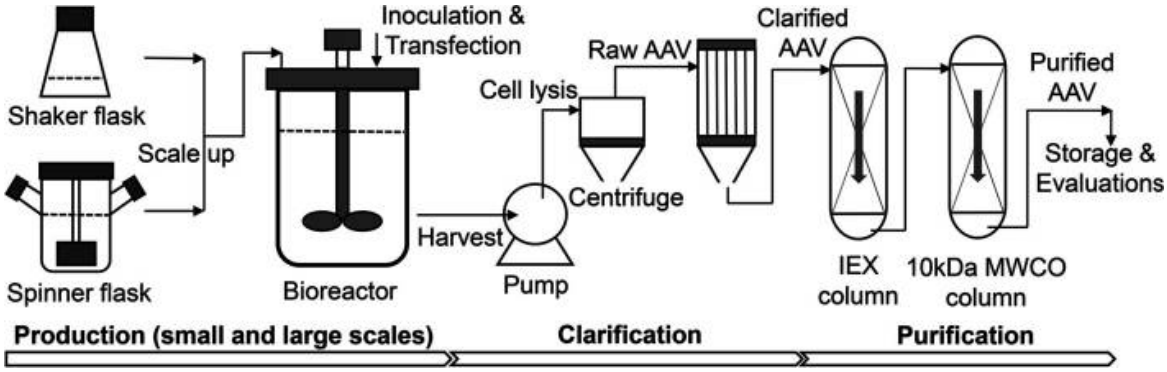

Figure 7. Process flow diagram (PFD) of the advanced AAV biomanufacturing platform.

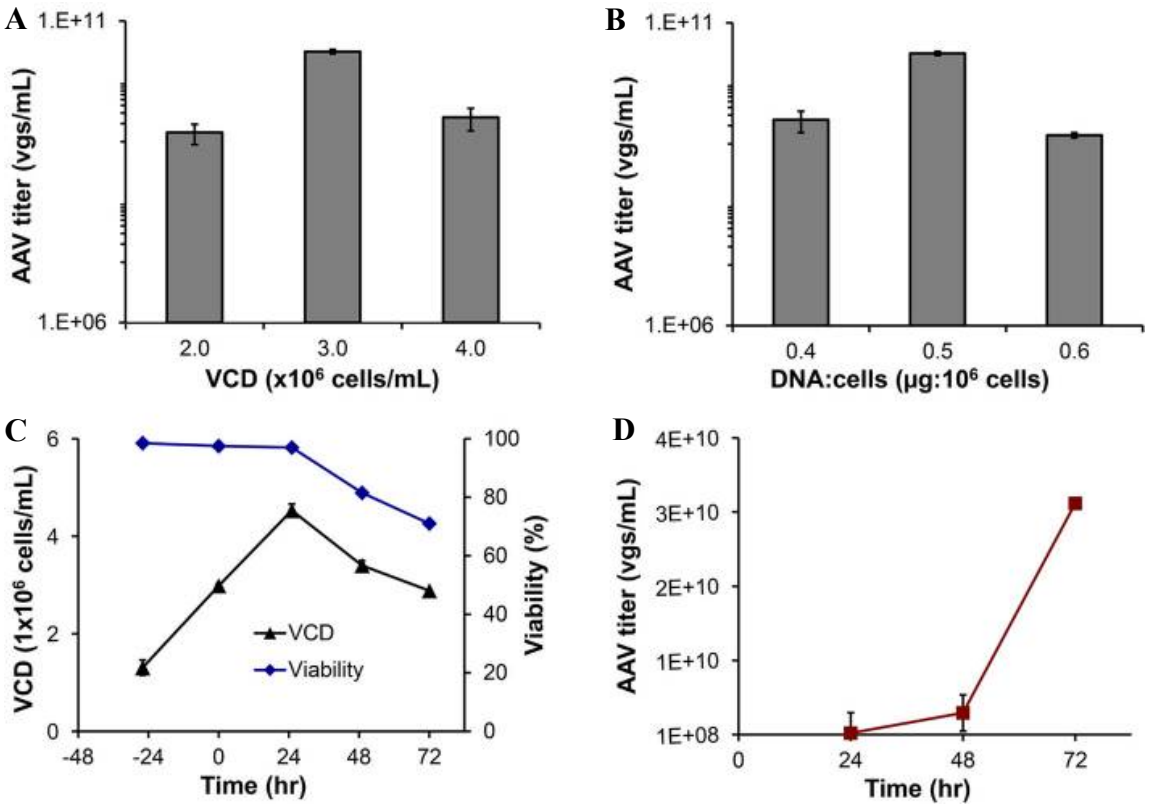

Figure 8. Development of 3-day suspensive AAV production in small-scale shaker flask.

(A) Evaluation of transfection VCD of 2.0, 3.0, and 4.0 × 10^6 cells/mL. **(B)** Evaluation of ratio of plasmid DNA and VPC cells including 0.4, 0.5 and 0.6 µg/1 × 10^6cells. **(C)** Viable cell density and viability of VPC pre- and post-transfection with maximal VCD of 4.53 × 10^6 cells/mL and harvest viability of 71% with optimal transfection conditions. **(D)** Volumetric productivity of AAV with final titer of 3.13 × $10.^{10}$ vg/mL with optimal transfection conditions. VPC cells were cultivated in 30-mL viral production medium supplemented with 6 g/L of glucose and 4 mM of GlutaMax at 37 °C, 8% CO_2, and 130 rpm. The production process could be applied to four serotypes (AAV2, 5, DJ, and DJ/8)

Host cells	Production container	Scale (mL)	AAV serotype	Transfect. reagent	Transfection VCD (c/mL)	DNA:cell (μg:10^6)	Productivity (10^{10} vg/mL)	Purification
HEK 293F	Shaker flask	30–60	AAV-DJ8	Liposomes	0.4×10^6	1.6:1	0.53 ± 0.08	10 kDa ultra
	Spinner flask	60–100	AAV-DJ8	Liposomes	0.4×10^6	1.6:1	0.50 ± 0.08	10 kDa UF
VPC	Shaker flask	30–60	AAV2	AAV-MAX	3×10^6	0.5:1	7.88 ± 0.39	Anion IEX (HPQ)
								HPQ
								Affinity (AVB), Sepharose (IEX)
		30–60	AAV5	AAV-MAX	3×10^6	0.5:1	2.97 ± 0.13	HPQ
		30–60	AAV-DJ8	AAV-MAX	2×10^6	0.5:1	0.14 ± 0.05	HPQ
					4×10^6	0.5:1	0.25 ± 0.13	
					3×10^6	0.4:1	0.25 ± 0.09	
					3×10^6	0.6:1	0.14 ± 0.01	
		30–60	AAV-DJ8	AAV-MAX	3×10^6	0.5:1	2.40 ± 0.06	Anion IEX (aPrime 4A)
								HPQ
								HPQ

All data are presented as mean ± standard error of the mean (SEM). $n = 2–3$

Table 1. Summary of AAV production.

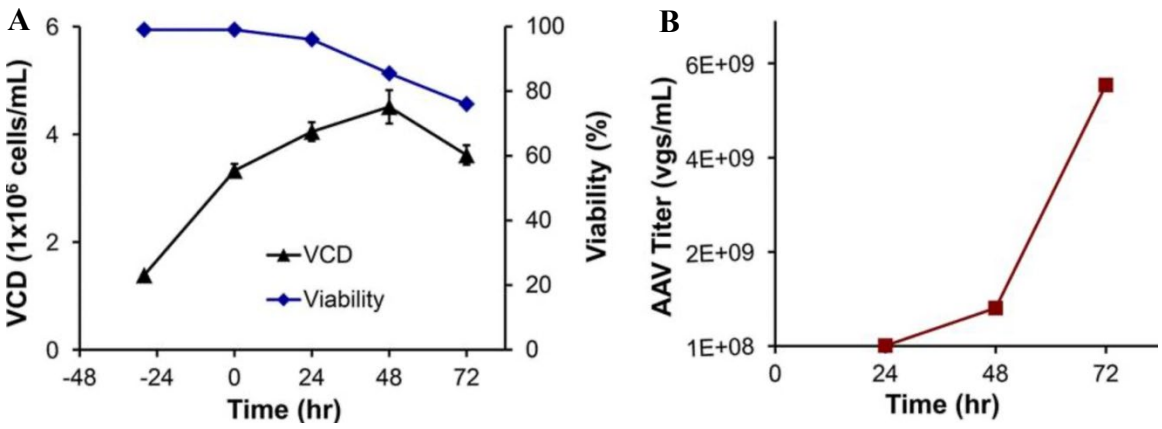

Figure 9. AAV production in spinner flask.

(A) Kinetic profile of VPC cell growth with peak VCD of 4.51×10^6 cells/mL and harvest viability of 76%. **(B)** AAV production with final titer of 0.59×10^{10} vg/mL. Spinner flaks cultures were carried out at 37 °C, 8% CO_2, and 230 rpm using AAV-DJ8 as model virus.

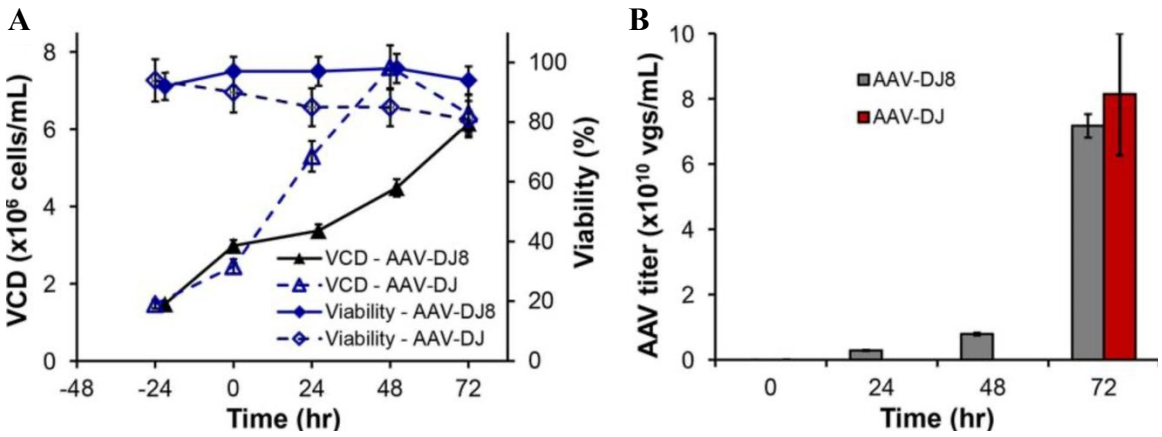

Figure 10. Scaled up AAV production in stirred-tank bioreactor.

(A) VPC cell growth profile with peak VCD of 6.15×10^6 cells/mL (AAV-DJ8) or 7.60×10^6cells/mL (AAV-DJ). VPC had better and healthier cell growth in bioreactor. **(B)** AAV concentration reached 7.17×10^{10} vg/mL (AAV-DJ8) or 8.14×10^{10} vg/mL (AAV-DJ). The 1.2–2.0 L of production cultures were performed in 2.5-L bioreactor with automatically controlled process parameters of 37 °C, pH 7.0, 210 rpm and DO.

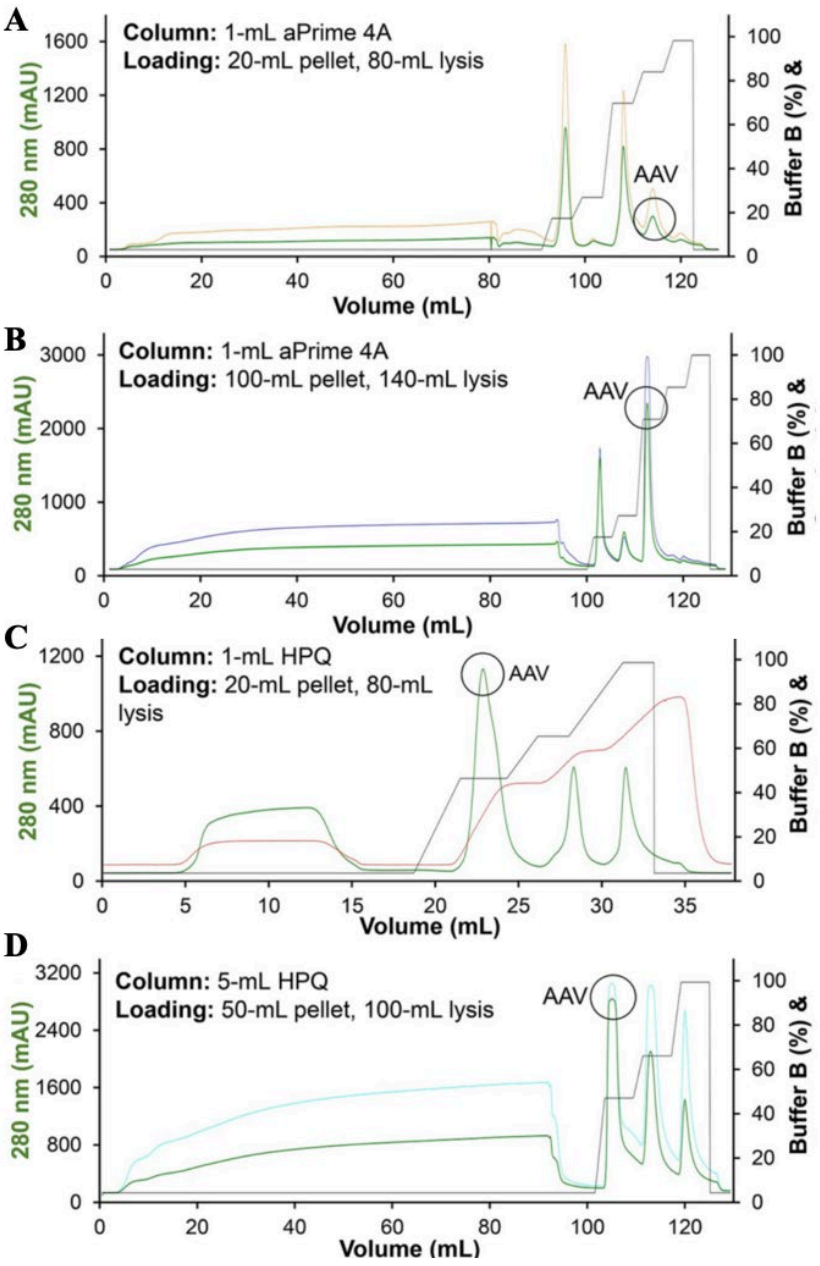

Figure 11. Development and optimization of anion exchange purification using liquid chromatography (LC).

The 80–140 mL of cell lysis from 20–100 mL of VPC pellet was loaded to the 1-mL or 5-mL columns. The representative LC profile of AAV-DJ8 was described here but four serotypes of AAV2, 5, DJ and DJ8 were tested using the developed purification strategy.

Equilibration buffer: 25 mM Tris–HCl, pH 9.0. Elution Buffer A: 25 mM Tris–HCl, 20 mM NaCl, pH 9.0. Elution buffer B: 25 mM Tris–HCl, 1 M NaCl, pH 9.0. Flow rate: 1.0 mL/min. **(A)** Stepwise elution of AAV-DJ8, 80-mL AAV lysis from 20-mL VPC pellet, in 1-mL EconoFit Nuvia aPrime 4A column. **(B)** Stepwise elution of AAV-DJ8, 140-mL AAV lysis from 100-mL VPC pellet, in 1-mL EconoFit Nuvia aPrime 4A column. **(C)** Stepwise elution of AAV-DJ8, 100-mL AAV lysis from 50-mL VPC pellet, using 1-mL Foresight Nuvia HPQ column, which can be scaled up from 1-mL column to 5-mL and 25-mL columns. **(D)** Stepwise elution of AAV-DJ8, 100-mL AAV lysis from 50-mL VPC pellet, using 5-mL Foresight Nuvia HPQ column.

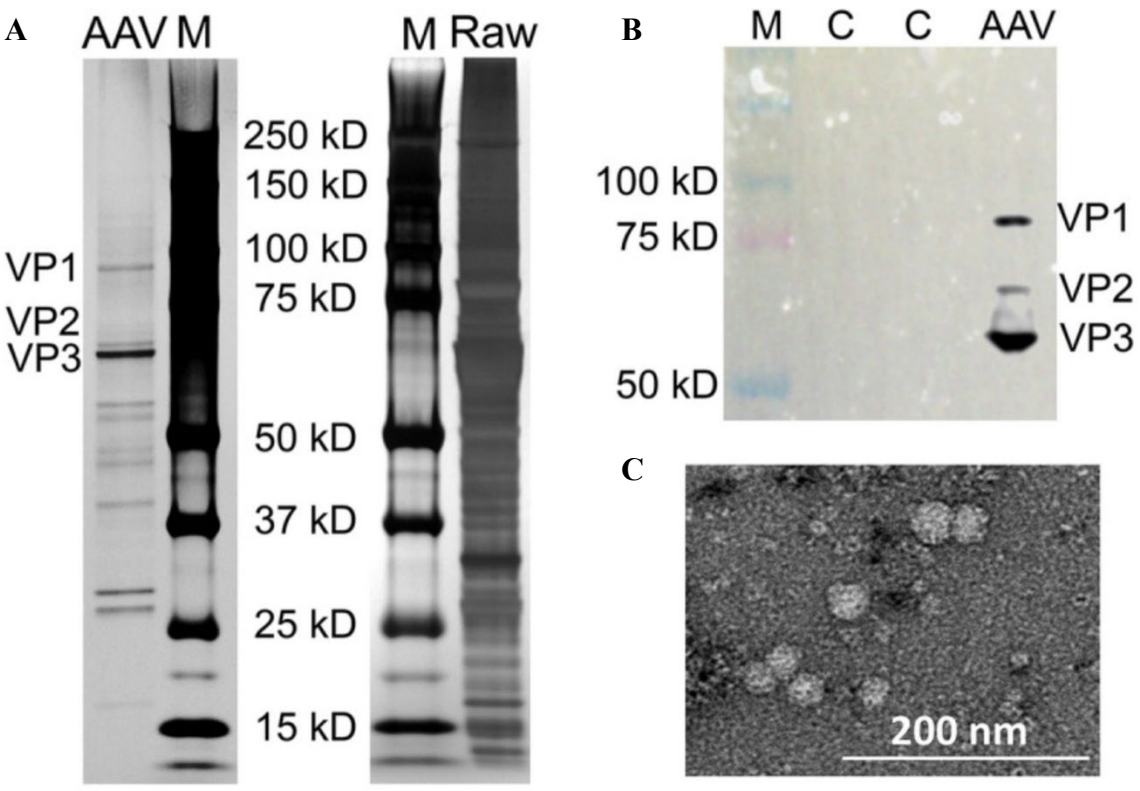

Figure 12. Characterizations of produced AAV.

(A) SDS-PAGE of AAV pre-purification and post anion exchange purification. M: marker, and C: negative control protein. **(B)** Western blot confirmed three AAV capsid proteins: VP1 (87 kDa), VP2 (73 kDa) and VP3 (62 kDa). **(C)** TEM image of purified AAV. Scale bar: 200 nm.

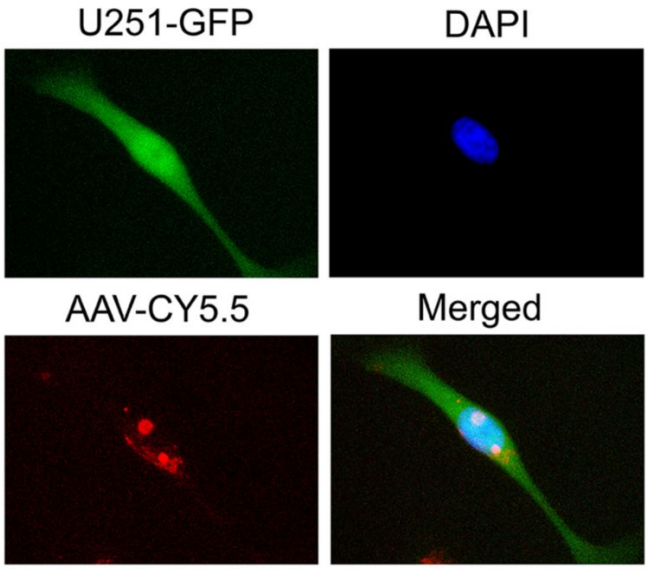

Figure 13. Confocal microscope demonstrating high transduction of AAV.

High transduction of AAV revealed by co-localization of green GFP (U251 cells), blue DAPI (nucleus), and red Sulfo-cyanine 5.5 (AAV). MOI = 5,000.

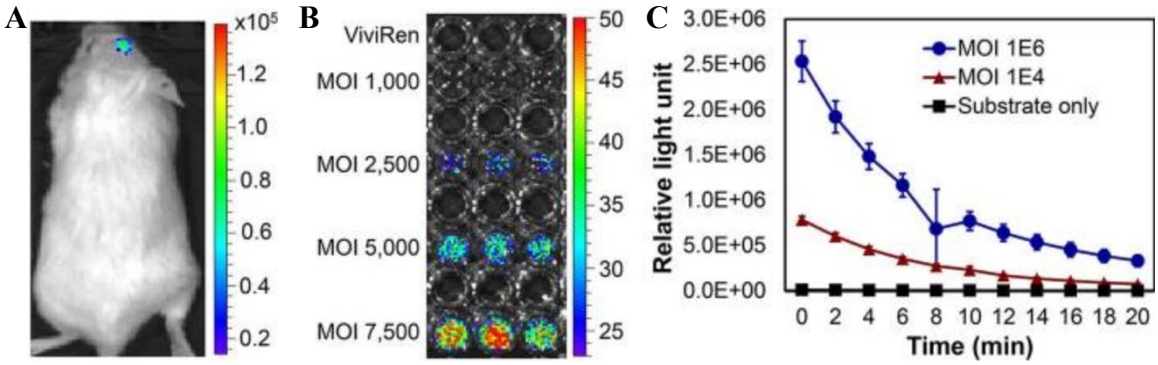

Figure 14. Evaluations of functional gene expression.

(A) Live-animal IVIS imaging showed high *in vivo* expression of AAV-delivered gene. About 0.5×10^6 U251 cells were intracranially injected to NSG mice using stereotactic instrument to develop glioblastoma xenografted models. AAV (1×10^{11} vg) and ViviRen (3.7 µg) were injected. **(B)** In vitro AAV gene expression is dosage (multiplicity of infection, MOI)-dependent. **(C)** AAV gene expression correlates to MOI, as measured by i3x plate reader.

Chapter 4. An Innovative Mitochondrial-targeted Gene Therapy to Treat Glioblastomas

Abstract

Targeting cancer cell mitochondria holds great therapeutic promise, yet current strategies to destroy cancer mitochondria *in vivo* specifically and effectively *in vivo* are limited. Here, we introduce mLumiOpto, an innovative mitochondrial-targeted luminoptogenetics gene therapy designed to directly disrupt the inner mitochondrial membrane (IMM) potential and induce cancer cell death. We synthesized a blue light-gated channelrhodopsin (CoChR) in the IMM and co-expressed a blue bioluminescence-emitting Nanoluciferase (NLuc) in the cytosol of the same cells. The mLumiOpto genes were selectively delivered to cancer cells *in vivo* by using adeno-associated virus (AAV) carrying a cancer-specific promoter. Induction with NLuc luciferin elicited robust endogenous bioluminescence, which activated mitochondrial CoChR, triggering cancer cell IMM permeability disruption, mitochondrial damage, and subsequent cell death. Importantly, mLumiOpto demonstrated remarkable efficacy in reducing tumor burden and killing tumor cells in glioblastoma or triple-negative breast cancer xenografted mouse models. These findings establish mLumiOpto as a novel and promising therapeutic strategy by targeting cancer cell mitochondria *in vivo*.

4.1 Introduction

Mitochondria are the major powerhouses of the cell and vital signaling organelles that regulate key cellular processes essential for maintaining cell growth and function [125]. These processes include ATP production [126], redox regulation [127], metabolite generation [128], thermogenesis [129], cell division [130], and programmed cell death [131]. Importantly, mitochondrial genetics and biochemical metabolisms have been implicated to be associated with various aspects of the cancer cell metastatic cascade, including motility and invasion, modulation of the microenvironment, plasticity, and colonization [132]. Given their crucial role in determining cancer cellular function and fate, mitochondria have emerged as a promising target for cancer treatment [133]. Over the last decades, numerous mitochondrial-targeted therapies, such as mitocans [134], mitochondriotropics [135], and mitochondriotoxics [136], have been developed to destroy mitochondria and induce cancer cell death. However, these therapies typically target specific signaling pathways or proteins, such as hexokinase [137], Bcl-2 family proteins [138], thiol redox [139], and VDAC/ANT [140], which may undergo unpredictive mutations or develop drug resistance during treatment, thus impairing anti-cancer efficacy [141]. More recently, studies reported that butformin [142], a mitochondrial-associated oxidative phosphorylation disruptor, or lonidamine [143], a mitochondrial complex I/II inhibitor, effectively enhanced the anti-tumor efficacy of photodynamic therapy. However, the translation of mitochondrial-targeted therapies to clinics has not yet succeeded.

The mitochondrion is composed of two membranes, a relatively permeable outer membrane and a highly folded and impermeable inner membrane (IMM). Proper

mitochondrial function relies on maintaining the electrical potential gradient across the IMM, known as $\Delta\Psi_m$, and a profound and sustained dissipation of $\Delta\Psi_m$ is considered as a crucial regulatory trigger for cell death [144]. Therefore, targeting IMM integrity and disrupting $\Delta\Psi_m$ has generated substantial interest as a potential strategy for cancer treatment. Chemical uncouplers (e.g., FCCP and CCCP) [145,146] or permeability transition pore (mPTP) activators (e.g., Atr and ployP) [147,148] have been used to depolarize $\Delta\Psi_m$. However, because mitochondrial activity is critical for all cells, the lack of specificity of these pharmacological strategies hinders utility *in vivo*. Genetic methods can modulate mitochondrial function in specific tissues but often cause irreversible side effects and do not directly target $\Delta\Psi_m$. Thus, there is currently a dearth of approaches that can directly and dynamically disrupt cancer cell $\Delta\Psi_m$ with greater specificity. Recently, we developed mitochondrial optogenetics (mOpto) by expressing heterologous light-gated Channelrhodopsin 2 (ChR2) in the IMM with a mitochondrial leading sequence (MLS) [149]. Importantly, sustained blue light illumination led to irreversible $\Delta\Psi_m$ depolarization and substantial cell death in cells expressing mitochondrial ChR2. However, despite its impressive capability to induce cytotoxicity, mOpto requires external light, which is difficult to penetrate deep tissues in the body, and lacks cancer-specific targeting, limiting its *in vivo* utility and future clinical translation for cancer and other diseases.

To achieve *in vivo* manipulation of mitochondria, we have developed a new-generation optogenetic tool called mitochondrial luminoptogenetics (mLumiOpto, patent US20210205475A1 [150]). This innovative approach harnesses intracellular luminescence as an endogenous light source, eliminating the need for external light stimulation.

Specifically, we co-expressed CoChR, a blue light-gated channelrhodopsin from Chloromonas oogama [151] in IMM, and an emission spectrum-matched Nanoluciferase (NLuc), a luciferase protein from the deep-sea shrimp Oplophorus gracilirostris [152], in the cytosol of the same cells. Additionally, we used a cancer- enhanced promoter (cfos) to maximize selective expression of mLumiOpto genes in tumor cells. We hypothesized that the mLumiOpto approach enables optogenetics-mediated GBM mitochondrial depolarization and cytotoxicity with the synthesized intracellular bioluminescence (NLuc). Furthermore, we hypothesized that mLumiOpto could effectively kill various GBM cells, significantly reduces tumor burden, and prolongs survival in intracranially xenograft mouse models *via* inducing irreversible $\Delta\Psi_m$ depolarization, persistent DNA damage and thereby severe apoptotic tumor cell death.

To test these hypotheses, we examined the ability of mLumiOpto to induce mitochondrial depolarization and cytotoxicity across different cancer cell types. Then the cancer-specific surface binding, internalization, transduction efficiency, biodistribution, and tumor-specific expression of mLumiOpto were assessed *in vitro* and *in vivo*. The therapeutic efficacy of mLumiOpto delivered with free AAV, was evaluated in preclinical mouse models carrying GBM xenograft. Our results demonstrated that mLumiOpto effectively induces cancer cell death and significantly reduces tumor burden without impairing normal organs or tissues.

4.2. Results

4.2.1. mLumiOpto development and optimization

We first constructed the mLumiOpto plasmid to co-express light-gated rhodopsin in the IMM and an emission spectrum-matched luciferase in the cytoplasm of the same cancer cells. Specifically, we synthesized the *NLuc-2A-ABCB10-CoChR* expressing plasmids by cloning CoChR (peak λex = 470 nm) and NLuc (peak λem = 460 nm), which were fused through a cleavable 2A linker, into a pcDNA3.0 expression vector (Fig. 15A). We utilized CoChR instead of the more commonly used ChR2 due to its much higher (~10-fold) photocurrent [151] and efficiency in inducing mOpto-mediated ΔΨm depolarization (Fig. 15B). NLuc was chosen for mLumiOpto as it generates much brighter bioluminescence compared to other discovered blue light-emitting luciferases such as *Renilla luciferase* (RLuc) [153] (Fig. 15C) and *Gaussia luciferase* (GLuc) [154] (data not shown) when coupled with ViviRen, an engineered luciferin. We then fused the ABCB10 mitochondrial leading sequence (MLS) [155] to the N-terminal of CoChR to facilitate mitochondrial expression. Consistent with our previous studies [149], ABCB10 MLS led to high-level and mitochondrial-specific CoChR expression across various tumor cell lines, including HeLa (Manders overlap coefficient, M1=0.99±0.03) and TNBC MDA-MB-231 (M1=0.98±0.1) (Fig. 15D), as revealed by the strong overlap between eYFP (green, fused with CoChR) and MitoTracker (red, a mitochondrial indicator). Confocal microscopy imaging also confirmed the co-expression of NLuc (fused with eGFP) and CoChR (fused with mCherry) in the transfected MDA-MB-231 cells (Fig. 15E).

4.2.2. AAV construction and characterization for *in vivo* gene delivery

To deliver the synthesized mLumOpto genes to cancer cells *in vivo*, we constructed an AAV expression vector using a commercial hybrid serotype AAV-DJ/8 with a heparin-binding domain mutation, which has shown high infection efficiency *in vivo* [156-159]. Additionally, we cloned and utilized the cfos promoter [160] to enhance cancer-selective gene expression. AAV was produced in a stirred-tank bioreactor and purified using ion-exchange liquid chromatography as we recently reported [161]. The size (~20 nm) and morphology of purified AAV DJ8 were verified using TEM (Fig. 16A). Western blotting confirmed the expression of three viral capsid proteins, including VP1 (87 kDa), VP2 (73 kDa), and VP3 (62 kDa) (Fig. 16B). Moreover, ViviRen triggered robust luminescence (Fig. 16C), along with substantial mitochondrial depolarization (Fig. 16D) in AAV-transduced human GBM U87 cells, demonstrating functional expression of mLumiopto proteins. Consistent with observed mitochondrial collapse, ViviRen induction caused dramatic cell death in various GMB cell lines transduced with mLumiOpto AAV, including the drug-resistant U251-TMZ cells (Fig. 16E).

4.2.3. AAV delivered mLumiOpto *in vivo*

To test the *in vivo* gene delivery of AAV, we performed and compared the intravenous (i.v.) and intracerebroventricular (i.c.v.) injections of AAV into GBM xenograft model. qRT-PCR analysis of the harvested tumor and important organs (lung, heart, kidney and liver) revealed that i.c.v. injection achieved GBM tumor-specific mLumiOpto gene delivery and remarkably higher levels of NLuc (Fig. 16F) and CoChR (Fig. 16G) expression than i.v. injection. Moreover, live-animal IVIS imaging (Fig. 16H) and *ex vivo*

imaging of the isolated organs (Fig. 16I) confirmed the functional expression of mLumiOpto genes in AAV (*via* i.c.v. injection) transduced GBM xenografts. Consequently, direct intracranial administration was utilized for the following anti-GBM efficacy studies.

4.2.4. *In vivo* Anti-GBM efficacy in U87 xenograft mouse model

To evaluate the *in vivo* GBM treatment efficacy of mLumiOpto, the xenografted mice were randomly divided into four groups (n=8-10/group) and i.c.v. administrated with saline (control), AAV only, mLumiOpto 1 (AAV dose: $0.5x10^{11}$ vg/mouse), and mLumiOpto 2 (AAV dose: $1.0x10^{11}$vg/mouse), respectively, on Days 7 and 14. Mice in the mLumiOpto groups received ViviRen through tail vein injection daily for 3 consecutive days following each AAV administration. Our data showed that mLumiOpto significantly prolonged the survival of GBM xenografted mice compared to control groups (Fig. 17A). Body weight profiles were similar across all groups (Fig. 17B). IVIS imaging performed on Day 28 (i.e., 10 days after the last ViviRen administration) revealed that the GBM tumor volumes in mLumiOpto groups were reduced by >10 folds compared to control groups (Fig. 17C and Fig. 17D). Endpoint MRI imaging on Day 44 (26 days post-treatment) confirmed the reduction of GBM tumor burden in the brain with mLumiOpto treatment compared to controls (Fig. 17E).

The H&E staining of tumor parafilm section slides showed that mLumiOpto treatment significantly reduced GBM tumor burden (Fig. 18A). IHC staining of tumor slides with antibodies of cleaved caspase 3 (cCasp3) and Ki67 indicated mLumiOpto induced

apoptosis and inhibited cell proliferation (Fig. 18B). Moreover, immunofluorescence assay revealed evident cytochrome C release in the treated group, implying mLumiOpto induced GMB mitochondrial depolarization and injury *in vivo* (Fig. 18D and Fig. 18E). No damage in normal organs of the brain, heart, lung, liver, spleen, and kidney was detected (Fig. 18C). The ViviRen only had no effect on GBM tumor and mouse body weight and no toxicity to normal organs (data not shown). It is worth noting that the anti-tumor efficacy is comparable between mLumiOpto 1 and mLumiOpto 2 groups (0.5 vs. $1.0x10^{11}$ vg/mouse), suggesting that AAV dose and administration schedule may need further optimization in the future.

4.2.5. *In vivo* Anti-GBM efficacy in PDX xenograft mouse model

In addition to assessing the efficacy of mLumiOpto in treating aggressive U87 xenografts, we investigated its effectiveness in heterogeneous GBM using PDX models. Firstly, subcutaneous GBM PDX xenografts were generated in mice (n=8/group), followed by i.v. injection of AAV and ViviRen. The PDX tumor weight in the treatment group was 40% lower than that in the saline group (Fig. 19A), while body weight profiles remained similar (Fig. 19B). Histological examination of major organs, including the brain, heart, lung, liver, spleen, pancreas, and kidney, did not reveal any signs of inflammation, apoptosis, or necrosis (Fig. 19C), indicating the tumor specificity and safety of AAV-delivered mLumiOpto.

Secondly, intracranial GBM PDX xenograft mouse models were established (n=4), and mice were treated with i.c.v. injection of AAV and ViviRen. MRI images at the endpoint

(14 weeks post-implantation) showed a significant reduction in GBM PDX tumor burden in the mLumiOpto-treated group compared to the saline group (Fig. 20A). H&E staining did not detect obvious injury or toxicity in normal organs of the treatment group (Fig. 20B). IHC staining of tumor slides with antibodies of cleaved caspase 3 and Ki67 indicated apoptosis-induced cell death and inhibition of proliferation, respectively, post- treatment (Fig. 20C).

4.3. Discussion

Mitochondria have been considered as a potential therapeutic target for cancer treatment, but translating this concept into clinical practice has proven challenging. Although certain drugs targeting mitochondria have demonstrated promise in preclinical studies, their effectiveness in human clinical trials has been limited due to the low treatment efficacy, development of drug resistance in cancer cells and the lack of specificity leading to risk of side-effects. To overcome these limitations, we introduce a novel therapeutic strategy, mLumiOpto, that can specifically and directly destroy cancer mitochondria to induce cancer cell death. Our preclinical mouse xenograft models demonstrate that AAV (i.c.v. administration) delivered mLumiOpto is effective at killing GBM cells and inhibiting tumor growth without causing noticeable side effects, highlighting its potential as a valuable tool for cancer research and targeted cancer therapy.

In recent years, optogenetics has revolutionized the precise and remote manipulation of cell membrane excitability, but its application to control intracellular organelles, particularly mitochondria, has remained limited. In this study, we introduced a novel

approach called mitochondrial-targeted luminoptogenetics (Fig. 21), which enables specific and dynamic manipulation of mitochondria both *in vitro* and *in vivo*. We determined NLuc as the intracellular light source for mLumiOpto technology. NLuc not only emits bright and sustained bioluminescence, even at low ViviRen concentrations, but it is also small (encoded by a 513-bp gene), ATP-independent, non-toxic to cells, and exhibits uniform intracellular distribution [152]. Our *in vitro* studies demonstrate that NLuc-ViviRen pair- generated intracellular bioluminescence is sufficient and effective to activate the mitochondrial CoChR channel, resulting in ViviRen dose-dependent $\Delta\Psi m$ depolarization in the absence of external light stimulation. By harnessing the endogenous bioluminescence, mLumiOpto overcomes the technical challenges associated with delivering external light to deep tissues within the body and minimizes potential side effects on surrounding healthy tissues. The ability to manipulate mitochondrial function in freely moving animals renders mLumiOpto a potent and versatile tool for *in vivo* investigations, ranging from elucidating the mechanistic underpinnings of mitochondrial dysfunction in various diseases to facilitating the development of mitochondrial-targeted therapeutic interventions.

The capability of mLumiOpto in inducing cancer cell death was validated using *in vitro* cell lines and *in vivo* tumor xenograft mouse models. We found that mLumiOpto induced GBM cell death in a ViviRen dose-dependent manner. Dose dependence is vital for optimizing treatment efficacy while minimizing side effects, as different cancer cells may exhibit varying sensitivities to mLumiOpto-mediated cytotoxicity. Determining the optimal mLumiOpto dosing strategy may enhance treatment effectiveness further. Our

animal studies further highlighted the ability of mLumiOpto to eliminate tumor cells *in vivo*. Treatment with mLumiOpto effectively inhibited tumor growth in various xenograft mouse models. Our findings are particularly significant, as there is still a lack of effective treatment options for those highly aggressive and recurrent cancers. It is worth noting that neither ViviRen nor mLumiOpto expression alone exhibited any deleterious effects on cancer mitochondria and cell viability. Altogether, these findings indicate the robust and versatile nature of mLumiOpto as a promising approach for targeted cancer cell death in both preclinical and translational settings. Its ability to effectively combat tumor growth across diverse cancer types of further positions mLumiOpto as a valuable therapeutic strategy for various malignancies.

In summary, our study introduces mLumiOpto, an innovative mitochondrial-targeted luminoptogenetic approach that enables dynamic manipulation of cancer mitochondria and triggers cytotoxicity. These advancements provide valuable insights for the development of novel therapeutic strategies that can address major challenges in cancer treatment, including reduced drug resistance and enhanced efficacy. Finally, mitochondria play an essential role in tumorigenesis, metastasis, and stemness, so its capability of dynamically depolarizing mitochondria renders mLumiOpto a powerful tool in mechanistic studies.

4.4. Methods

4.4.1. Cell lines, seed cultures and media

Viral Production Cells 2.0 (VPC, Gibco, Buffalo, NY) were used to produce AAV. The cervical cancer cell line HeLa (ATCC) was used for the general characterization of

mLumiOpto technology. The human TNBC cell lines MDA-MB-231 (GenTarget, San Diego, CA), and GBM cell lines U251 (MilliporeSigma, Burlington, MA), drug-resistant U251-TMZ (in-house developed), U87 and GL261 (Creative Bioarray, Shirley, NY) were used for *in vitro* cytotoxicity, surface binding, AAV gene delivery, gene expression studies. The U87, U251, and U87-FLuc (ATCC) were used to develop xenograft mouse models for evaluating the *in vivo* anti-tumor efficacy of mLumiOpto.

All cell culture media, supplements and other reagents were purchased from Gibco unless otherwise specified. The seed culture of VPC was maintained in a chemically defined viral production medium supplemented with 4 mM GlutaMAX in shaker flasks on an orbital shaker at 135 rpm. HeLa cells were cultured in DMEM supplemented with 10% (v/v) Fetal Bovine Serum (FBS) and 2 mM L-glutamine in T25 or T75 flasks. The MDA-MB-231 cells were cultured in DMEM/F12 medium supplemented with 10% FBS, 4 g/L glucose, 4 mM L-glutamine, 100 U/mL Penicillin and 100 µg/mL Streptomycin in T-flasks. U251 and U251-TMZ cells were maintained in EMEM with 2 mM L-glutamine, 1% non-essential amino acids (NEAA), 1 mM sodium pyruvate and 10% FBS in T25 or T75 flasks. U87 cells were maintained in EMEM with 10% FBS and 8 µg/mL Blasticidin. All cell lines were maintained between 10% and 80% confluence and kept at 37 °C with 5% CO2 (8% CO2 for VPC cells) in a humidified CO2 incubator (Eppendorf, Enfield, CT). The viable cell density (VCD) and viability were measured using TC20 automated cell counter (Bio-Rad, Hercules, CA) or hemocytometer and trypan blue (Fisher Scientific, Hanover Park, IL).

4.4.2. Plasmid construction

CMV-ABCB-CoChR-eYFP. The ABCB, CoChR and eYFP gene fragments were amplified from CAG-ABCB-ChR2-eYFP, AAV-Syn-CoChR-GFP (Addgene #59090), and pcDNA3.1-PsChR2-eYFP (Addgene #69057), respectively. The PCR primers are ABCB-forward, ABCB-reverse, CoChR-forward, CoChR-reverse, eYFP_1-forward, and eYFP_1-reverse (Table 2). These gene fragments were cloned into pcDNA3.1-PsChR2-eYFP backbone vector using the HiFi Assembly Kit (New England Biolabs, lpswich, MA).

CMV-NLuc-2A-ABCB-CoChR-mCherry. The NLuc, 2A, and ABCB-CoChR-mCherry gene fragments were PCR amplified from *pNL-CMV-NLuc* (Promega #N1091), *pcDNA3.0-Magneto2.0-p2A-mCherry*, and *CMV-ABCB-CoChR-mCherry*, respectively. The amplified genes were cloned into the *CMV-ABCB-CoChR-mCherry* vector using the HiFi Assembly Kit. The PCR primers are NLuc_1-forward, NLuc_1-reverse, 2A-forward, 2A-reserve, ABCB-CoChR_2-forward, and ABCB-CoChR_2-reserve (Table 2).

pAAV-D/J8-cfos-NLuc-2A-ABCB-CoChR. The NLuc-2A-ABCB-CoChR gene fragment was PCR amplified from *CMV-NLuc-2A-ABCB-CoChR-mCherry* and cloned into the pAAV-D/J8 AAV expression vector (Cell Biolabs, San Diego, CA) following the manufacture instruction. The primers are NLuc-CoChR_2-forward and NLuc-CoChR_2-reverse (Table 2). The sequence of the construction was confirmed with sequencing primers forward: 5'- GGATTGACGGGAACAG-3', and reverse: 5'-GGTGTATATCGAGAGC-3'.

4.4.3. AAV production and purification

The small-scale (30 or 60 mL) productions of AAV were performed in 125 or 250-mL shaker flasks using VPC 2.0 in viral production medium at 37 °C, 135 rpm and 8% CO2. The large-scale production was performed in 2-L stirred-tank bioreactor (Disteck, Cedar Falls, IA) at 37 °C, pH 7.0, 210 rpm and DO 40%. VPC cells were co-transfected at VCD of $3x10^6$ cells/mL with three plasmids, i.e., *AAV-D/J8-cfos-NLuc-2A-ABCB-CoChR*, AAV- DJ/8 Rep-Cap and AAV-D/J8 Helper (1:3:1), at plasmid DNA:cell ratio of 0.5 μg:10^6 cells. The formulation of transfection mixture per liter of culture volume was 1.5 mg total plasmid DNA, 10% (v/v) viral-plex complexation buffer, 0.6% AAV-MAX transfection reagent, and 0.3% AAV-MAX transfection booster. The enhancer (1%) was added to the VPC culture immediately before plasmid transfection. Production culture was sampled daily to monitor cell growth using TC20 automated cell counter, glucose level using Glucose 201 DM System (HemoCure, Brea, CA), and AAV titer using qRT-PCR. VPC cells containing AAV were harvested at 72 hrs post-transfection for AAV isolation.

In the end of AAV production, culture broth was centrifuged at 4 °C and 1,000 x g for 20 minutes. VPC cell pellet was re-suspended in 10% AAV-MAX lysis buffer (Gibco), followed by three freeze-thaw cycles (incubation in ethanol/dry ice bath for 30 minutes and in 37 °C water bath for 15 minutes), and further incubated with 2 mM MgCl2 and 90 U/mL benzonase (MilliporeSigma, Burlington, MA) at 37 °C for 60 minutes. After cell lysis was confirmed with microscopy, the lysate was clarified by centrifugation at 4 °C and 4,500 × g for 30 minutes, and the supernatant was filtered using 0.2-μm PES membrane to remove cell debris. The filtrate was partially purified, preconditioned, and concentrated using

Vivaspin Turbo column MWCO 100 kDa (Sartorius, Bohemia, NY) for further AAV purification.

NGC liquid chromatography, equipped with a 5-mL Foresight Nuvia HPQ anion-exchange column prepacked with CHT ceramic hydroxyapatite XT mixed-mode chromatography media (Bio-Rad) or 25-mL column in-house packed with the same CHT media, was used to purify free AAV. HPQ column was equilibrated with buffer A (25 mM Tris-HCl, 20 mM NaCl, pH 8.0), loaded with the buffer A-preconditioned AAV sample, and eluted step wisely using buffers A and B (25 mM Tris- HCl, 1 M NaOH, pH 8.0) at a flow rate of 0.6 mL/minute. The primarily purified AAV was further proceeded with ultrafiltration using 100-kDa MWCO PES membrane column to remove small protein impurities, desalt, exchange with formulation buffer (1x PBS, 5% Sorbitol, and 350 mmol/L NaCl), and concentrate as previously described [123].

4.4.4. Intracranial Xenograft Model

Five-week-old nude (J:NU HOM Homozygous for Foxn1<nu>) mice were purchased from Jackson Lab. After one week of acclimatization, mice were used to generate tumor xenograft models for *in vivo* evaluation of mLumOpto technology. All animal studies conformed to the Laboratory Animals Guideline of the US National Institutes of Health (Publication No. 85 - 23). The animal protocols were approved by the Institutional Animal Care and Use Committee at Ohio State University (IACUC-2022A00000055).

4.4.5. Confocal imaging

Colocalization analysis: Cells cultivated on a 15-mm glass-bottom dish were transfected with *CMV-ABCB-CoChR-eYFP* plasmid. Forty-eight hours after transfection, cells were loaded with MitoTracker Deep Red (250 nM) for 30 minutes. The localization of CoChR-YFP and MitoTracker was simultaneously imaged with 543 nm argon laser and 635 nm laser diode lines using Olympus FV1000 confocal microscope (Olympus America, Center Valley, PA). For NLuc and CoChR co-expression analysis, cells were transfected with *CMV-NLuc-GFP-2A-ABCB-CoChR-mCherry* plasmid. Forty-eight hours later, the expression of NLuc-GFP and CoChR- mCherry was imaged with the 488 and 545 laser lines, respectively. For colocalization analysis, the confocal images were processed offline using ImageJ software (National Institutes of Health, Bethesda, MD). The overlapping was quantified by calculating the Manders coefficient.

Mitochondrial depolarization and $\Delta\Psi_m$ measurement: The mLumiOpto-treated or control cells were stained with fluorescent mitochondrial membrane potential dye TMRM (100 nM) or Mitoview 633 (25 nM). The fluorescence of TMRM and Mitoview 633 was imaged with the 543 nm and 635 nm laser, respectively, and analyzed using ImageJ software.

Analysis of AAV transduction in vitro: As described in our previous studies [119,124], AAV carrying *cfos-NLuc-2A-ABCB-CoChR* genes was labelled with fluorescent dye Cy5.5 and incubated with U251 cells that were stained with DAPI. The transduction of AAV-Cy5.5 was detected with an Olympus FV1000 confocal microscope. The nucleus stained with

DAPI was imaged with the 405 nm laser line and Cy5.5 was imaged with the 640 nm laser line, respectively.

4.4.6. *In vitro* cytotoxicity assay

GBM cells were seeded onto 96-well plates at a density of $5x10^4$ cells/mL and incubated with mLumiOpto AAV (MOI of 100,000) at 37 °C and 5% CO_2 in the incubator for 48 hours. Then ViviRen (0-60 μm) was added to the culture in well plates. Two days later, cell viability was measured using CellTiter-Glo Luminescent Cell Viability Assay (Promega, Madison, MI), as previously described [119].

4.4.7. Bioluminescence imaging

Cells were seeded in clear-bottom black well-plates (Corning, Corning, NY) and cultured with mLumiOpto plasmid or AAV. Forty-eight hours later, the culture medium was replaced with a colorless culture medium containing a varying dose of ViviRen (0- 30 μM). The bioluminescence was detected at 0, 2, 4, 6 and 20 hours using IVIS Lumina Series III (PerkinElmer, Waltham, MA) at 470 nm.

GBM xenograft mice were injected with one dose of AAV mediated mLumiOpto ($1x10^{11}$ vg/ mouse intracranially) and ViviRen (2 μg/g-BW *via* intravenous injection). Twenty-four hours later, mice were imaged with IVIS Lumina Series III to measure the NLuc luminescence. The tumor-specific targeting was determined by 1) analyzing the NLuc luminescence in live-animal IVIS imaging, as previously described [123], 2) *ex vivo* IVIS imaging of the harvested major organs (brain, heart, lung, liver, kidney, spleen) after mice

were sacrificed, and 3) transcript analysis of tumor and organs (heart, brain, lung, kidney, liver) using qRT- PCR.

4.4.8. Magnetic Resonance Imaging (MRI) imaging

The Magnetic Resonance Imaging (MRI) imaging was performed with the BioSpect 94/30USR system (Bruker BioSpin; Billerica, MA) and ParaVision 6.0 software provided by the Ohio State University Small Animal Imaging Core Facility. T2-weighted scans were acquired with flowing parameters of TR/TE: 2500/33 (ms), FA: 180 (degree), NEX: 2, FOV: 20 mm*15.313, matrix: 256*196, 1 mm slice thickness, 1 mm slice distance and 18 slices. Mice were anesthetized and 0.2 mmole/kg Gadolinium-based contrast agent was administrated intraperitoneally before imaging. Then the mice were secured on an animal bed and placed in the MRI scanner for imaging. A rectal thermometer with body contact was used to measure the body temperature. The respiration and heart rate of mice were monitored using the Small Animal Monitoring System (Model 1025, Small Animals Instruments, Inc. Stony Brook, NY) during the imaging session.

4.4.9. Xenograft mouse models

Six-week-old nude (J:NU HOM Homozygous for Foxn1<nu>) mice, with an equal number of males and females, were stereotactically injected with human GBM cells [116,124]. Briefly, $0.5x10^5$ U87 cells were suspended in 3-μL growth medium and implanted into the frontal region of the cerebral cortex at a rate of 0.4 μL/min using Stoelting Just for Mouse Stereotaxic Instrument (Stoelting, Wood Dale, IL). The burr hole in the skull was closed with sterile bone wax and 5 mg/kg of carprofen was provided immediately before surgery

and every 12-24 hours for 48 hours post-surgery. The intracranially xenografted mice were monitored daily for one week and randomized into four groups (n=10/group). Then mice were treated with saline (control), AAV only ($0.5x10^{11}$ vg, control), mLumiOpto at AAV doses of $0.5x10^{11}$ vg and $1.0x10^{11}$ vg on Days 7 and 14 *via* i.c.v. injection, followed by three s.c. injections of ViviRen (37 μg) at 3 days post AAV administration in mLumiOpto treatment groups.

GBM PDX line was provided by Dr. Jann Sarkaria at Mayo Clinic and maintained at low passages (2–4) in NSG mice following our established protocol [116,124]. Fresh frozen PDX tissues were thawed, minced into small fragments (~1 mm3), and subcutaneously (s.c.) implanted into NSG mice. The PDX xenograft mice were randomized into two groups (n=5), treated with AAV ($1x10^{13}$ vg/kg) carrying mLumiOpto genes *via* tail vein with 5 injections from Day 4 to day 8, and followed with four s.c. injections of ViviRen (37 μg) from Day 13 to Day 16. Tumor volume was measured by a caliper and body weight was monitored every two or three days for 35 days. PDX intracranial mouse model was generate following previous describe method.

4.4.10. RNA isolation and transcript expression analysis

Total RNA was extracted and purified from the tumor or organ tissues using the RNeasy mini kit (Qiagen, Germantown, MD). cDNA was synthesized from 500 ng of RNA using QuantiTect Reverse Transcription Kit (Qiagen). Quantitative real-time PCR was performed using Select Master Mix (Thermo Fisher, Asheville, NC) in a BioRad IQ5 detection system (Bio-Rad, Portland, ME). The transcript level of the NLuc and CoChR

genes were normalized to the average levels of Gapdh and Rpl32. PCR primers are listed in Table 3, and their specificity was confirmed with 1% agarose gel electrophoresis and melt curves. The fold difference for the mRNA expression level was calculated using $2^{-\Delta\Delta Ct}$.

4.4.11. Immunofluorescence

The GBM tumor tissue was embedded in paraffin and sectioned at 5 μm on slides. After deparaffinizing, the tumor tissue was treated with citric acid buffer pH 6.0 for antigen retrieval. Then, the tissue was treated with PBS containing 5% goat serum and 0.3% Triton X-100 to block nonspecific staining. The tumor tissue was then incubated overnight at 4°C with anti- TOMM20 (1:200 dilution) and anti-cytochrome C (1:200 dilution) primary antibodies (Abcam, Waltham, MA). Thereafter, the tissue was stained with 1:200 diluted secondary antibodies labeled with AF488 and/or AF647 in 1% BSA, 5% goat serum, and 0.3% Tween 20 in PBS. Finally, coverslips were mounted on slides and imaged using an Olympus FV1000 confocal microscope.

4.4.12. Hematoxylin and eosin (H&E) staining

The tumor tissue and normal organs (heart, brain, lung, liver, spleen, kidney) were embedded in paraffin and sectioned at 5 μm. After deparaffinizing, the slides were stained with hematoxylin and eosin solution and imaged using the high-performance Nikon microscope (Irving, TX) as previously described [119].

4.4.13. Antibodies and chemicals

Mouse primary antibodies and HRP-conjugated secondary anti-mouse antibodies were obtained from Abcam. TOMM20 and cytochrome c antibodies were purchased from Abcam and Cell Signaling Technology (Danvers, MA), respectively. MitoSox and MitoTracker were purchased from Life Technologies. PVDF membrane and T-PER tissue protein extraction reagents were obtained from Thermo Scientific (Waltham, MA). All other reagents were from Millipore Sigma.

4.4.14. Statistical analysis

The experimental data were reported as mean ± standard error of the mean (SEM). Statistical comparisons among groups were performed using the two-way ANOVA Tukey's multiple comparisons test or one-way ANOVA Holm-Sidak's multiple comparisons test. $P<0.05$ was considered statistically significant. The distribution of data was tested using the Shapiro-Wilk normality test.

Founding

This work was supported by DoD BCRP W81XWH2110066/67, NIH NCI 1R01CA262028-01A1, and NIH R01HL156581.

Figures

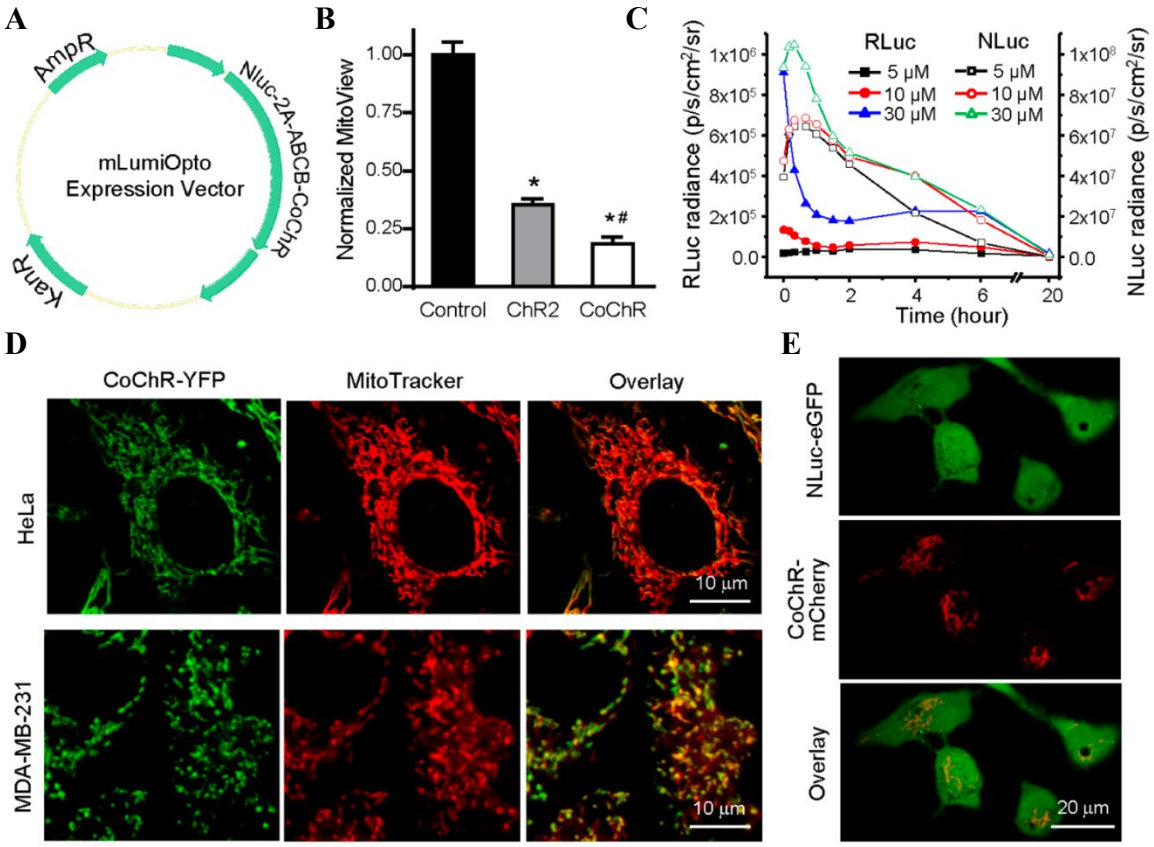

Figure 15. Development of mLumiOpto technology.

(A) Map of mLumiOpto expression vector carrying the luciferase (i.e., NLuc) and mitochondrial rhodopsin (i.e., ABCB-CoChR) genes linked *via* a cleavable 2A linker. **(B)** Photostimulation with LED light (0.5 mW/mm2, 24 hours) caused more severe mitochondrial depolarization (measured by MitoView, a voltage-sensitive fluorescent dye) in cells expressing ABCB-CoChR compared to those expressing ABCB-ChR2. **(C)** IVIS imaging revealed that NLuc emitted much stronger luminescence than RLuc when coupled with luciferin ViviRen. **(D)** ABCB10 mitochondrial leading sequence resulted in high-level, mitochondrial-specific CoChR expression in HeLa and MDA-MB-231 cells, as demonstrated by the strong overlap of eYFP (green, fused to CoChR) and MitoTracker dye

(red, a mitochondrial marker). **(E)** Representative confocal images demonstrated the co-expression of NLuc-GFP and CoChR-mCherry in mLumiOpto plasmid-transfected TNBC MDA-MB-231 cells. *: $P<0.05$ vs. control (mock transfected). #: $P<0.05$ vs. ChR2. n=4/group.

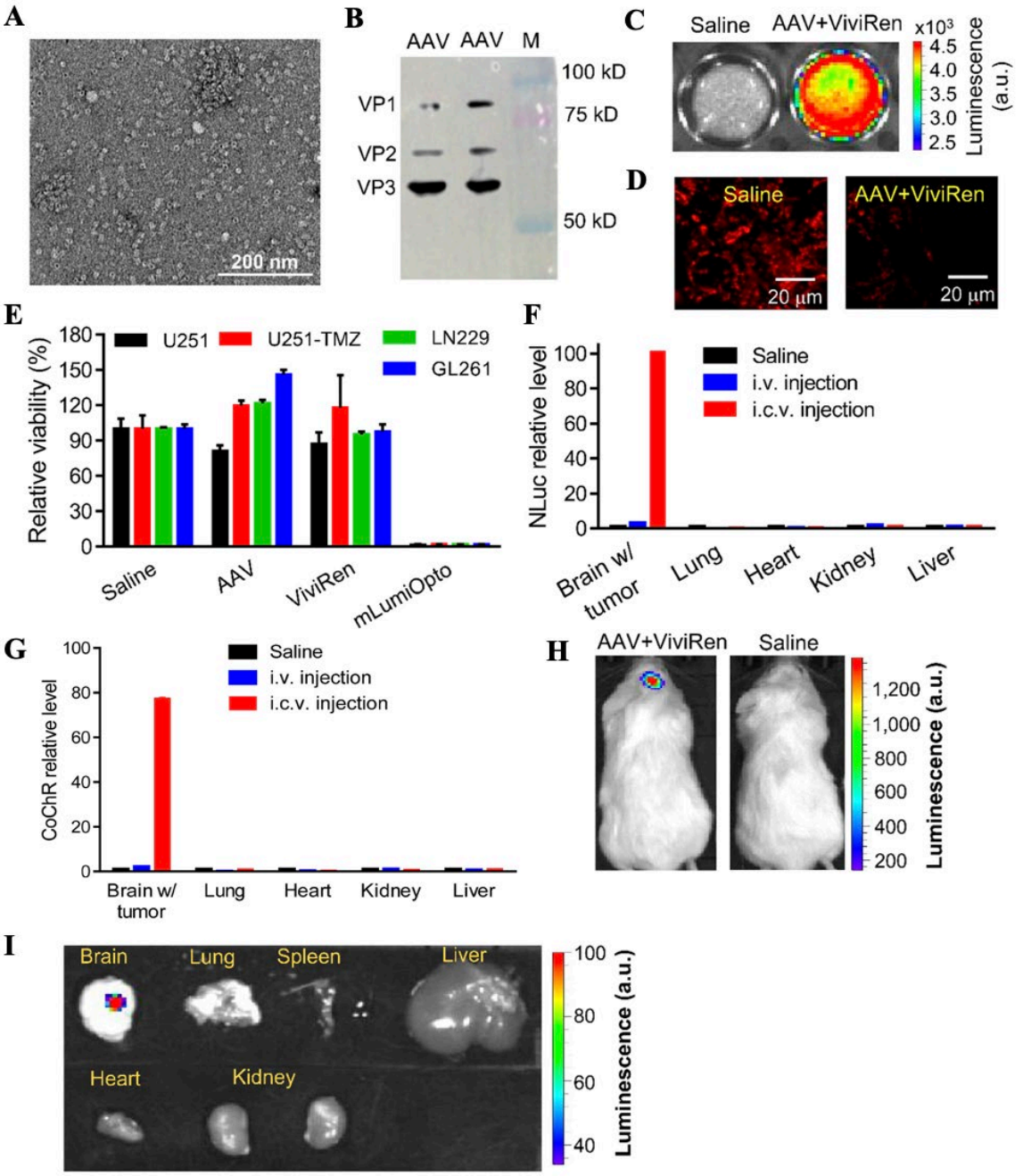

Figure 16. Characterization of mLumiOpto technology.

(A) Transmission electron microscopy imaging showed AAV DJ8 particles with the correct morphology and size (~20 nm). **(B)** Western blotting confirmed the presence of AAV viral capsid proteins VP1 (87 kDa), VP2 (73 kDa), and VP3 (62 kDa). **(C)** ViviRen (30 μM)

induced strong NLuc luminescence in mLumiOpto AAV-transduced GBM U87 cells. **(D)** mLumiOpto (AAV+ViviRen) induced severe mitochondrial depolarization in GBM U87 cells, as measured by MitoView fluorescence. **(E)** mLumiOpto killed 90-99% of GBM U251, U251-TMZ, LN229, and GL261 cells within 72 hours, while AAV or ViviRen alone had no significant cytotoxic effect on these cells. **(F)** Intracerebroventricular (i.c.v.) AAV injection led to remarkably higher (~33-35 folds) mLumiOpto gene (NLuc) expression in GBM tumors compared to intravenous (i.v.) injection. **(G)** Intracerebroventricular (i.c.v.) AAV injection led to remarkably higher CoChR expression in GBM tumors compared to intravenous (i.v.) injection. n=4/group. **(H)** ViviRen elicited strong luminescence in mLumiOpto AAV-transduced intracranial GBM xenografts. **(I)** *Ex vivo* IVIS imaging confirmed mLumiOpto expression in GBM xenografts but not in normal organs. n=4-6/group.

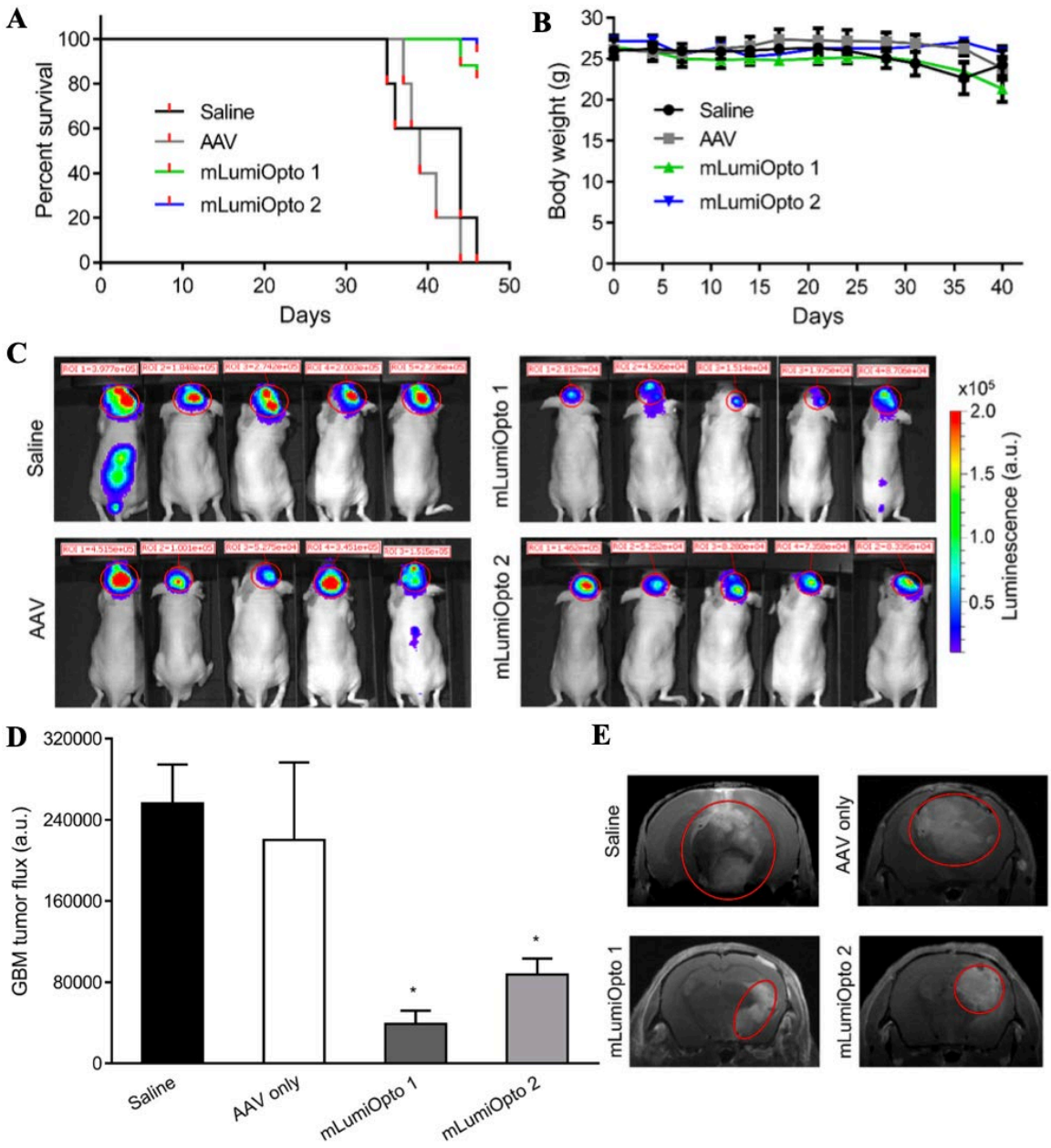

Figure 17. Evaluations of anti-cancer efficacy of AAV-delivered mLumiOpto in GBM xenograft mouse model.

(A) mLumiOpto treatment significantly extended the survival of GBM xenograft mice. **(B)** Body weight trends were similar among the control and treatment groups. **(C)** IVIS imaging revealed >10-fold reduction in GBM tumor size in mLumiOpto treatment groups

compared to control (saline and AAV only) groups. **(D)** Quantification of GBM tumor bioluminescence flux collected in IVIS imaging. n=5/group. **(E)** MRI images taken in the late stage of the survival study (i.e., 44 days post-cell implantation or 23 days after the last ViviRen injection) confirmed a significant reduction of GBM tumor burden in mLumiOpto treatment groups. n=8-10/group.

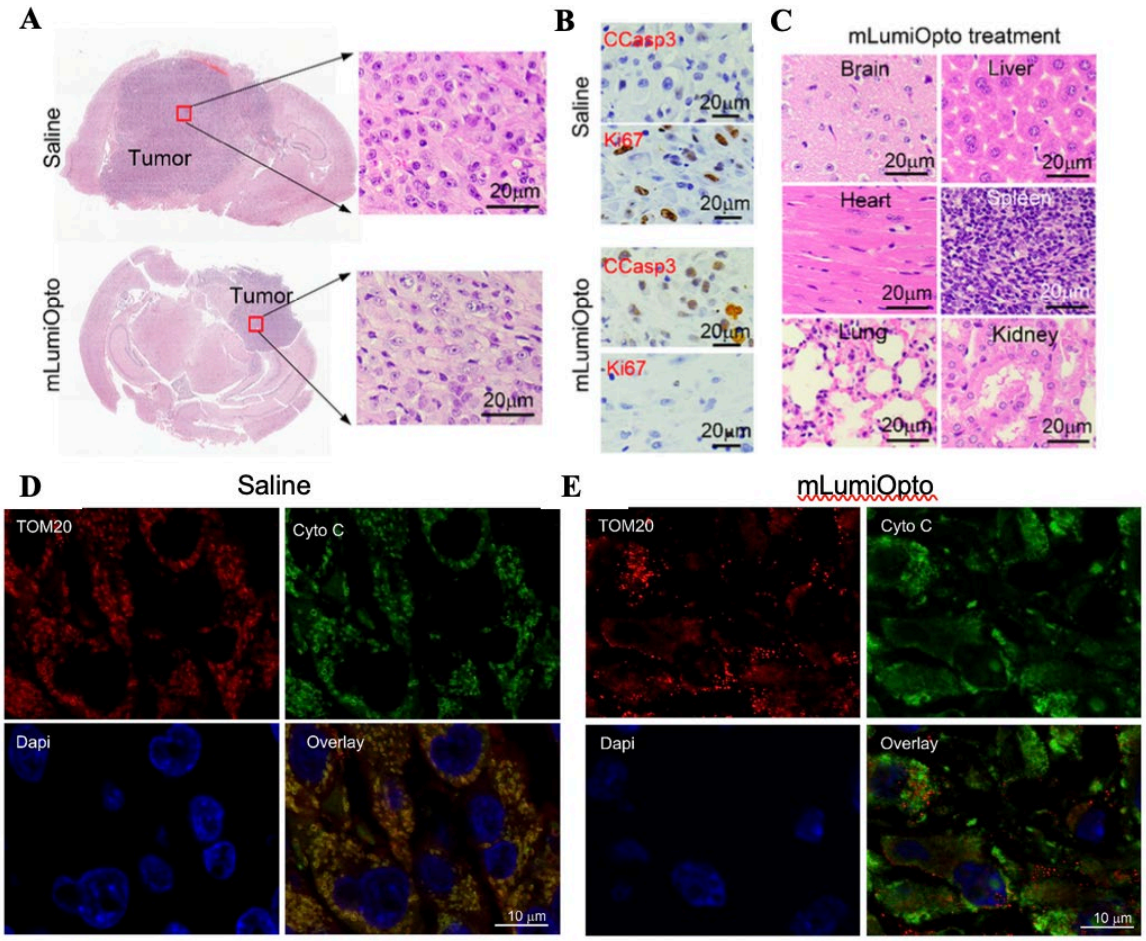

Figure 18. Histology and immunofluorescent analysis in GBM xenograft mouse tissue. **(A)** H&E staining of the parafilm section slides of GBM xenograft demonstrated tumor burden reduction by mLumiOpto. **(B)** IHC staining of tumor slides with antibodies of cleaved caspase 3 and Ki67 indicated apoptosis-induced cell death and inhibition of proliferation, respectively, post- treatment. **(C)** H&E staining did not detect obvious injury or toxicity in normal organs of the treatment group. **(D)** Immunofluorescence assay revealed that TOM20 overlaps with cytochrome C in the control GBM tissue. **(E)** Cytochrome C staining becomes diffusive and TOM20 staining is fragmented in the

mLumiOpto-treated GBM, indicating cytochrome C release and mitochondrial depolarization.

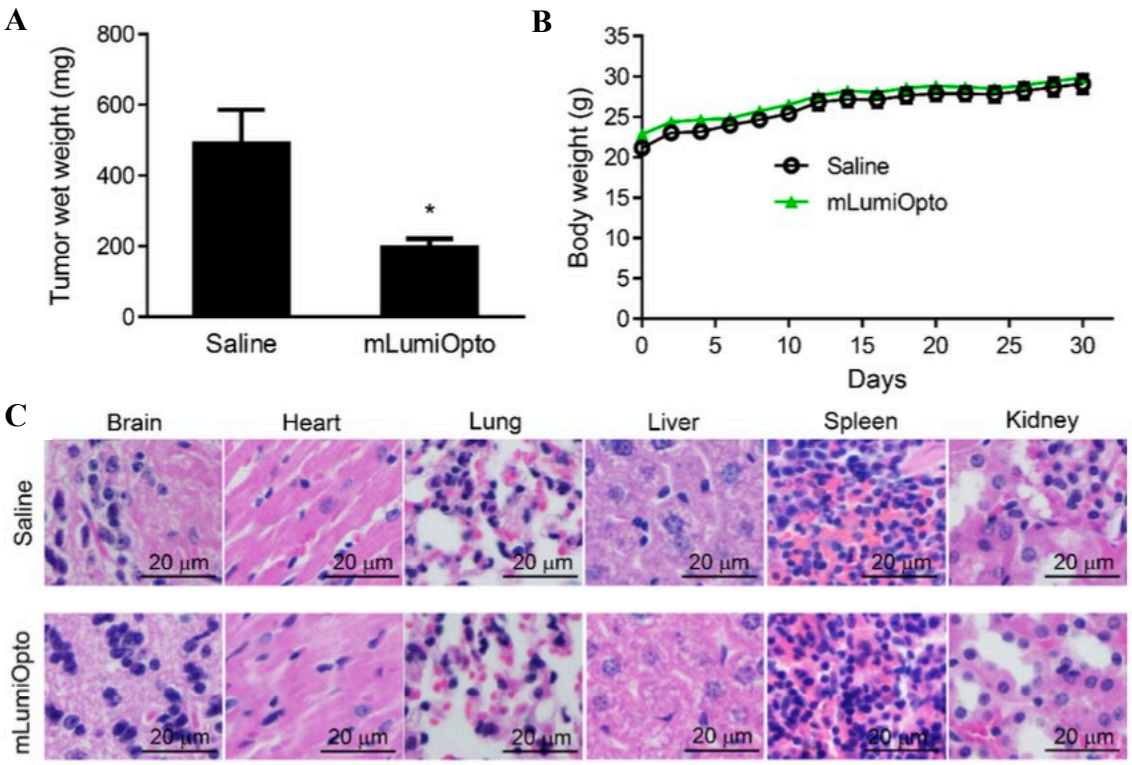

Figure 19. Evaluations of anti-cancer efficacy of mLumiOpto in GBM subcutaneous PDX mouse model.

(A) mLumiOpto treatment caused a significant decrease in tumor wet weight compared to the control group. **(B)** Body weight did not exhibit significant differences between groups. **(C)** H&E staining did not detect any damage in normal organs (brain, heart, lung, liver, spleen, pancreas, kidney) of the treatment group. *: $P<0.05$ vs. Saline. n=5-8/group.

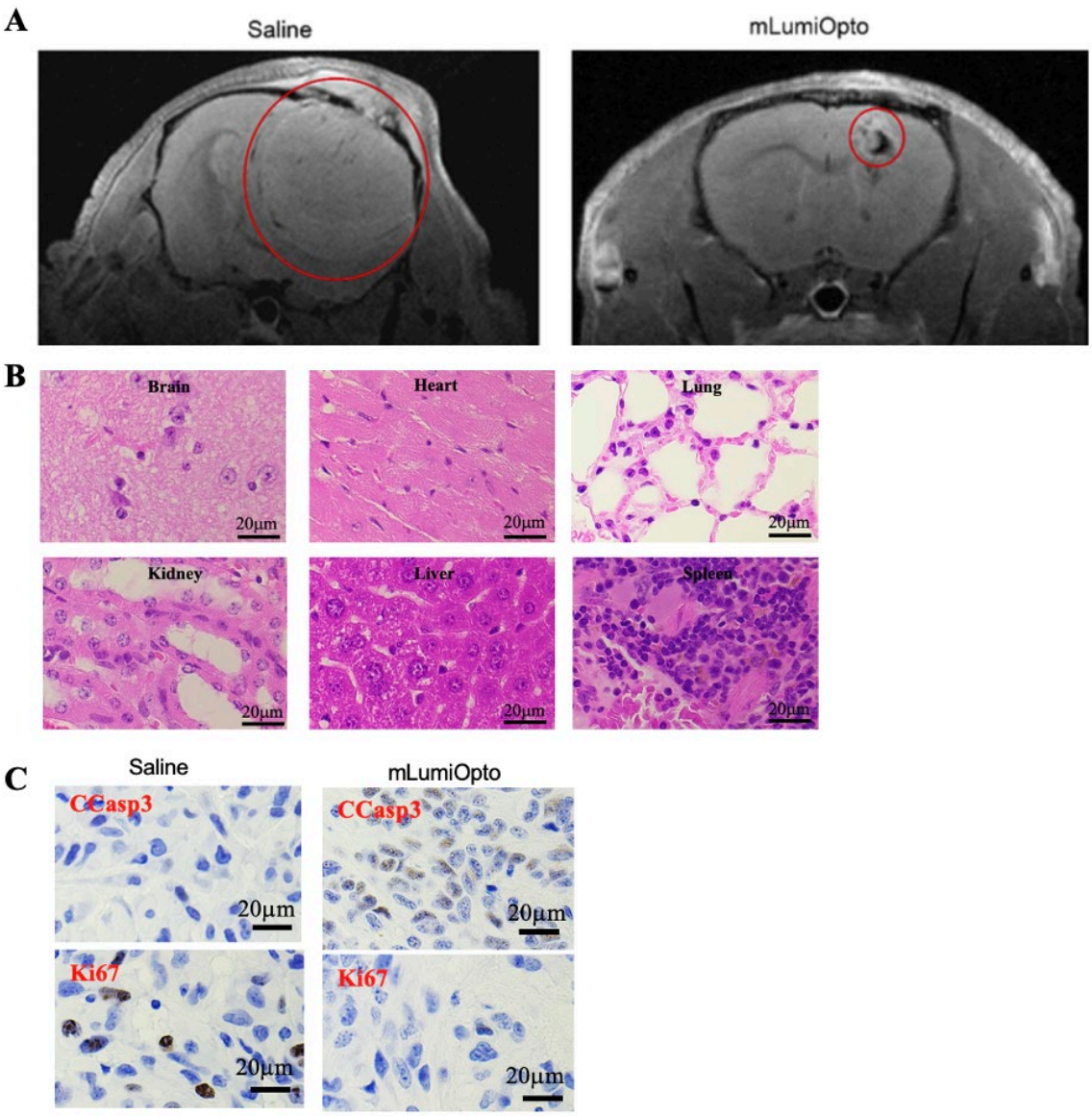

Figure 20. Evaluation of anti-cancer efficacy of mLumiOpto in GBM orthotopic PDX mouse model.

(A) MRI images of intracranially xenografted GBM PDX at the endpoint (14 weeks post PDX xenograft) showed that GBM tumor burden was significantly reduced by mLumiOpto treatment. n=4-5/group. **(B)** H&E staining did not detect obvious injury or toxicity in normal organs of the treatment group. **(C)** IHC staining of tumor slides with antibodies of

cleaved caspase 3 and Ki67 indicated apoptosis-induced cell death and inhibition of proliferation, respectively, post- treatment.

Name	Sequence
ABCB-forward	TAAGCTTGGTACCGAGCTCGGATCCCACCATGCGCGCCCCTTC
ABCB-reverse	TTCCCAGCATAACTGCAGCTGACAGTCTCCC
CoChR-forward	AGCTGCAGTTATGCTGGGAAACGGCAGC
CoChR-reverse	TCACTAGCATTGCTACTACCGGTGCCGC
eYFP_1-forward	GGTAGTAGCAATGCTAGTGAGCAAGGGC
eYFP_1-reverse	ACCTTCGAACCGCGGGCCCTCTAGATTACTTGTACAGCTCGTCC
ABCB-CoChR_1-forward	ACCCAAGCTTGGTACCGGGTCTAGACACCATGCGCGCCCCTTC
ABCB-CoChR_1-reverse	CCTCCTCGCCCTTGCTCACGGATCCCACTGTCTCCTCGTCCTCCTG
NLuc_1-forward	ACTCACTATAGGGAGACCCACACCATGGTCTTCACACTCG
NLuc_1-reverse	TGCCTGATCCCGCCAGAATGCGTTCGCAC
2A-forward	CATTCTGGCGGGATCAGGCAGCGGCGCC
2A-reserve	GGGCGCGCATGGGACCGGGGTTTTCTTCCACG
ABCB-CoChR_2-forward	CCCCGGTCCCATGCGCGCCCCTTCTGCT
ABCB-CoChR_2-reserve	CCTCCTCGCCCTTGCTCACGTGCTACTACCGGTGCCGC
NLuc_2-forward	ACTCACTATAGGGAGACCCACACCATGGTCTTCACACTCG
NLuc_2-reserve	TGCTAGCCATCGCCAGAATGCGTTCGCAC
GFP-forward	CATTCTGGCGATGGCTAGCAAAGGAGAAG
GFP-reserve	CCCTGCCCTCGTAGAGCTCATCCATGCC
2A-ABCB-CoChR-forward	TGAGCTCTACGAGGGCAGGGGAAGTCTTC
2A-ABCB-CoChR-reserve	CCTCCTCGCCCTTGCTCACGCACTGTCTCCTCGTCCTC
NLuc-CoChR_1-forward	GTACCGGGTCTAGAGCCACCATGGCTTCCAAG
NLuc-CoChR_1-reverse	CCTTGCTCACCATTGCTACTACCGGTGC
eYFP_2-forward	GGTAGTAGCAATGGTGAGCAAGGGCGAG
eYFP_2-reverse	TTAGGATCCTTACACCTCGTTCTCG
NLuc-CoChR_2-forward	AATTCCCCGGGGATCCACGCGTAAGCTTTCCTTT
NLuc-CoChR_2-reverse	ATGGTGGCTCTAGAGAGAGATCTGCGCAAAA

Table 2. List of PCR primers for plasmid construction

mRNA	Forward	Reserve
CoChR	CCACCAGCACATCATCATCTA	CATGGTCTCCACTTCCATCTC
NLuc	ATTGTCCTGAGCGGTGAAA	CACAGGGTACACCACCTTAAA
Gapdh	CATGGCCTTCCGTGTTCCTA	CCTGCTTCACCACCTTCTTGAT
Rpl32	CTGGAGGTGCTGCTGATGT	GGGATTGGTGACTCTGATGG

Table 3. List for RT-PCR primers.

Bibliography

1. Louis DN, Ohgaki H, Wiestler OD, et al. The 2007 WHO classification of tumours of the central nervous system. *Acta Neuropathol.* 2007;114(2):97-109.
2. Iacob G, Dinca EB. Current data and strategy in glioblastoma multiforme. *J Med Life.* 2009;2(4):386-393.
3. Felthun J, Reddy R, McDonald KL. How immunotherapies are targeting the glioblastoma immune environment. *J Clin Neurosci.* 2018;47:20-27.
4. Hanif F, Muzaffar K, Perveen K, Malhi SM, Simjee Sh U. Glioblastoma Multiforme: A Review of its Epidemiology and Pathogenesis through Clinical Presentation and Treatment. *Asian Pac J Cancer Prev.* 2017;18(1):3-9.
5. Ali MY, Oliva CR, Noman ASM, et al. Radioresistance in Glioblastoma and the Development of Radiosensitizers. *Cancers (Basel).* 2020;12(9).
6. Singh N, Miner A, Hennis L, Mittal S. Mechanisms of temozolomide resistance in glioblastoma - a comprehensive review. *Cancer Drug Resist.* 2021;4(1):17-43.
7. Barenholz YC. Doxil®—The first FDA-approved nano-drug: Lessons learned. *Journal of controlled release.* 2012;160(2):117-134.
8. Ou J, Si Y, Goh K, et al. Bioprocess development of antibody-drug conjugate production for cancer treatment. *PloS one.* 2018;13(10):e0206246.
9. Si Y, Kim S, Zhang E, et al. Targeted exosomes for drug delivery: biomanufacturing, surface tagging, and validation. *Biotechnology journal.* 2020;15(1):1900163.
10. Si Y, Guan J, Xu Y, et al. Dual-targeted extracellular vesicles to facilitate combined therapies for neuroendocrine cancer treatment. *Pharmaceutics.* 2020;12(11):1079.
11. Chen K, Si Y, Ou J, et al. Antibody–Drug Conjugate to Treat Meningiomas. *Pharmaceuticals.* 2021;14(5):427.
12. Si Y, Kim S, Ou J, et al. Anti-SSTR2 antibody-drug conjugate for neuroendocrine tumor therapy. *Cancer gene therapy.* 2021;28(7):799-812.
13. Si Y, Xu Y, Guan J, et al. Anti‐EGFR antibody‐drug conjugate for triple‐negative breast cancer therapy. *Engineering in Life Sciences.* 2021;21(1-2):37-44.
14. Si Y, Zhang Y, Guan J-S, et al. Anti-CD47 Monoclonal Antibody–Drug Conjugate: A Targeted Therapy to Treat Triple-Negative Breast Cancers. *Vaccines.* 2021;9(8):882.
15. Santiago-Ortiz JL, Schaffer DV. Adeno-associated virus (AAV) vectors in cancer gene therapy. *J Control Release.* 2016;240:287-301.
16. Carter BJ. Adeno-associated virus vectors in clinical trials. *Hum Gene Ther.* 2005;16(5):541-550.

17. Hacker UT, Bentler M, Kaniowska D, Morgan M, Büning H. Towards Clinical Implementation of Adeno-Associated Virus (AAV) Vectors for Cancer Gene Therapy: Current Status and Future Perspectives. *Cancers (Basel).* 2020;12(7).
18. Britten CM, Walter S, Janetzki S. Immunological Monitoring to Rationally Guide AAV Gene Therapy. *Front Immunol.* 2013;4:273.
19. Peng Z, Liu C, Wu M. New insights into long noncoding RNAs and their roles in glioma. *Molecular cancer.* 2018;17:1-10.
20. Han L, Ren Y, Long L, et al. Inhibition of C6 glioma in vivo by combination chemotherapy of implantation of polymer wafer and intracarotid perfusion of transferrin-decorated nanoparticles. *Oncol Rep.* 2012;27(1):121-128.
21. Westphal M, Ram Z, Riddle V, Hilt D, Bortey E, Group ECotGS. Gliadel® wafer in initial surgery for malignant glioma: long-term follow-up of a multicenter controlled trial. *Acta neurochirurgica.* 2006;148:269-275.
22. Felthun J, Reddy R, McDonald KL. How immunotherapies are targeting the glioblastoma immune environment. *Journal of Clinical Neuroscience.* 2018;47:20-27.
23. Chuang DF, Lin X. Targeted therapies for the treatment of glioblastoma in adults. *Current Oncology Reports.* 2019;21:1-12.
24. van den Bent MJ, Brandes AA, Rampling R, et al. Randomized phase II trial of erlotinib versus temozolomide or carmustine in recurrent glioblastoma: EORTC brain tumor group study 26034. *Journal of Clinical Oncology.* 2009;27(8):1268.
25. Hegi ME, Diserens A-C, Bady P, et al. Pathway analysis of glioblastoma tissue after preoperative treatment with the EGFR tyrosine kinase inhibitor gefitinib—a phase II trial. *Molecular cancer therapeutics.* 2011;10(6):1102-1112.
26. Chakraborty S, Filippi CG, Wong T, et al. Superselective intraarterial cerebral infusion of cetuximab after osmotic blood/brain barrier disruption for recurrent malignant glioma: phase I study. *Journal of neuro-oncology.* 2016;128:405-415.
27. Kinsella P, Howley R, Doolan P, et al. Characterization and response of newly developed high-grade glioma cultures to the tyrosine kinase inhibitors, erlotinib, gefitinib and imatinib. *Experimental Cell Research.* 2012;318(5):641-652.
28. Lu J, Hu Y, Qian R, Zhang Y, Yang X, Luo P. Enhanced proliferation inhibition and apoptosis in glioma cells elicited by combination of irinotecan and imatinib. *European Journal of Pharmacology.* 2020;874:173022.
29. Nishio M, Kim D-W, Wu Y-L, et al. Crizotinib versus chemotherapy in Asian patients with ALK-positive advanced non-small cell lung cancer. *Cancer research and treatment: official journal of Korean Cancer Association.* 2018;50(3):691.
30. Chinot OL, Wick W, Mason W, et al. Bevacizumab plus radiotherapy–temozolomide for newly diagnosed glioblastoma. *New England Journal of Medicine.* 2014;370(8):709-722.
31. Kalpathy-Cramer J, Chandra V, Da X, et al. Phase II study of tivozanib, an oral VEGFR inhibitor, in patients with recurrent glioblastoma. *Journal of neuro-oncology.* 2017;131:603-610.
32. Kreisl TN, McNeill KA, Sul J, Iwamoto FM, Shih J, Fine HA. A phase I/II trial of vandetanib for patients with recurrent malignant glioma. *Neuro-oncology.* 2012;14(12):1519-1526.

33. Neyns B, Sadones J, Chaskis C, et al. Phase II study of sunitinib malate in patients with recurrent high-grade glioma. *Journal of neuro-oncology.* 2011;103:491-501.
34. Muhic A, Poulsen HS, Sorensen M, Grunnet K, Lassen U. Phase II open-label study of nintedanib in patients with recurrent glioblastoma multiforme. *Journal of neuro-oncology.* 2013;111:205-212.
35. Pitz MW, Eisenhauer EA, MacNeil MV, et al. Phase II study of PX-866 in recurrent glioblastoma. *Neuro-oncology.* 2015;17(9):1270-1274.
36. Ma DJ, Galanis E, Anderson SK, et al. A phase II trial of everolimus, temozolomide, and radiotherapy in patients with newly diagnosed glioblastoma: NCCTG N057K. *Neuro-oncology.* 2015;17(9):1261-1269.
37. Kane JR, Miska J, Young JS, Kanojia D, Kim JW, Lesniak MS. Sui generis: gene therapy and delivery systems for the treatment of glioblastoma. *Neuro-oncology.* 2015;17(suppl_2):ii24-ii36.
38. Michaud K, Solomon DA, Oermann E, et al. Pharmacologic inhibition of cyclin-dependent kinases 4 and 6 arrests the growth of glioblastoma multiforme intracranial xenografts. *Cancer research.* 2010;70(8):3228-3238.
39. Amagata T, Rath C, Rigot JF, et al. Structures and Cytotoxic Properties of Trichoverroids and Their Macrolide Analogues Produced by Saltwater Culture of Myrothecium v errucaria. *Journal of Medicinal Chemistry.* 2003;46(20):4342-4350.
40. Woldemichael GM, Turbyville TJ, Vasselli JR, Linehan WM, McMahon JB. Lack of a functional VHL gene product sensitizes renal cell carcinoma cells to the apoptotic effects of the protein synthesis inhibitor verrucarin A. *Neoplasia.* 2012;14(8):771-IN728.
41. Yan F, Yu Y, Chow D-C, et al. Identification of verrucarin a as a potent and selective steroid receptor coactivator-3 small molecule inhibitor. *PLoS One.* 2014;9(4):e95243.
42. Oda T, Namikoshi M, Akano K, Kobayashi H, Honma Y, Kasahara T. Verrucarin A inhibition of MAP kinase activation in a PMA-stimulated promyelocytic leukemia cell line. *Marine Drugs.* 2005;3(2):64-73.
43. Shimizu T, O'Connor PM, Kohn KW, Pommier Y. Unscheduled activation of cyclin B1/Cdc2 kinase in human promyelocytic leukemia cell line HL60 cells undergoing apoptosis induced by DNA damage. *Cancer Research.* 1995;55(2):228-231.
44. Palanivel K, Kanimozhi V, Kadalmani B. Verrucarin A alters cell-cycle regulatory proteins and induces apoptosis through reactive oxygen species-dependent p38MAPK activation in the human breast cancer cell line MCF-7. *Tumor Biology.* 2014;35:10159-10167.
45. Deeb D, Gao X, Liu Y, et al. The inhibition of cell proliferation and induction of apoptosis in pancreatic ductal adenocarcinoma cells by verrucarin A, a macrocyclic trichothecene, is associated with the inhibition of Akt/NF-κB/mTOR prosurvival signaling. *International journal of oncology.* 2016;49(3):1139-1147.

46. Šamec N, Zottel A, Videtič Paska A, Jovčevska I. Nanomedicine and immunotherapy: a step further towards precision medicine for glioblastoma. *Molecules.* 2020;25(3):490.
47. Miranda A, Blanco-Prieto MJ, Sousa J, Pais A, Vitorino C. Breaching barriers in glioblastoma. Part II: Targeted drug delivery and lipid nanoparticles. *International journal of pharmaceutics.* 2017;531(1):389-410.
48. Masserini M. Nanoparticles for brain drug delivery. *International Scholarly Research Notices.* 2013;2013.
49. Lopez-Bertoni H, Kozielski KL, Rui Y, et al. Bioreducible polymeric nanoparticles containing multiplexed cancer stem cell regulating miRNAs inhibit glioblastoma growth and prolong survival. *Nano letters.* 2018;18(7):4086-4094.
50. Qu J, Zhang L, Chen Z, et al. Nanostructured lipid carriers, solid lipid nanoparticles, and polymeric nanoparticles: which kind of drug delivery system is better for glioblastoma chemotherapy? *Drug delivery.* 2016;23(9):3408-3416.
51. Sarisozen C, Dhokai S, Tsikudo EG, Luther E, Rachman IM, Torchilin VP. Nanomedicine based curcumin and doxorubicin combination treatment of glioblastoma with scFv-targeted micelles: In vitro evaluation on 2D and 3D tumor models. *European journal of pharmaceutics and biopharmaceutics.* 2016;108:54-67.
52. Jiang Y, Lv L, Shi H, et al. PEGylated Polyamidoamine dendrimer conjugated with tumor homing peptide as a potential targeted delivery system for glioma. *Colloids and Surfaces B: Biointerfaces.* 2016;147:242-249.
53. Ye Z, Zhang T, He W, et al. Methotrexate-loaded extracellular vesicles functionalized with therapeutic and targeted peptides for the treatment of glioblastoma multiforme. *ACS applied materials & interfaces.* 2018;10(15):12341-12350.
54. Ciccocioppo F, Lanuti P, Marchisio M, Miscia S. Extracellular vesicles involvement in the modulation of the glioblastoma environment. *Journal of oncology.* 2020;2020.
55. Li YM, Hall WA. Cell surface receptors in malignant glioma. *Neurosurgery.* 2011;69(4):980-994.
56. Ghosh D, Funk CC, Caballero J, et al. A cell-surface membrane protein signature for glioblastoma. *Cell systems.* 2017;4(5):516-529. e517.
57. Sousa F, Moura RP, Moreira E, Martins C, Sarmento B. Therapeutic monoclonal antibodies delivery for the glioblastoma treatment. *Advances in protein chemistry and structural biology.* 2018;112:61-80.
58. Wang Z, Wang Z, Zhang C, et al. Genetic and clinical characterization of B7‐H3 (CD276) expression and epigenetic regulation in diffuse brain glioma. *Cancer science.* 2018;109(9):2697-2705.
59. do Carmo A, Patricio I, Cruz MT, Carvalheiro H, Oliveira CR, Lopes MC. CXCL12/CXCR4 promotes motility and proliferation of glioma cells. *Cancer Biol Ther.* 2010;9(1):56-65.
60. Liu Y, Gao X, Deeb D, et al. Mycotoxin verrucarin A inhibits proliferation and induces apoptosis in prostate cancer cells by inhibiting prosurvival Akt/NF-

κB/mTOR signaling. *Journal of experimental therapeutics & oncology.* 2016;11(4).
61. Zhao M, van Straten D, Broekman ML, Préat V, Schiffelers RM. Nanocarrier-based drug combination therapy for glioblastoma. *Theranostics.* 2020;10(3):1355.
62. von Achenbach C, Weller M, Szabo E. Epidermal growth factor receptor and ligand family expression and activity in glioblastoma. *Journal of neurochemistry.* 2018;147(1):99-109.
63. Xu H, Zong H, Ma C, et al. Epidermal growth factor receptor in glioblastoma. *Oncology letters.* 2017;14(1):512-516.
64. Saadeh FS, Mahfouz R, Assi HI. EGFR as a clinical marker in glioblastomas and other gliomas. *The International journal of biological markers.* 2018;33(1):22-32.
65. Leung HW, Lang H-C, Wang S-Y, Leung JH, Chan AL. Cost-utility analysis of stereotactic body radiotherapy plus cetuximab in previously irradiated recurrent squamous cell carcinoma of the head and neck. *Expert Review of Pharmacoeconomics & Outcomes Research.* 2021;21(3):489-495.
66. Bonner JA, Harari PM, Giralt J, et al. Radiotherapy plus cetuximab for squamous-cell carcinoma of the head and neck. *New England Journal of Medicine.* 2006;354(6):567-578.
67. Jonker DJ, O'Callaghan CJ, Karapetis CS, et al. Cetuximab for the treatment of colorectal cancer. *New England Journal of Medicine.* 2007;357(20):2040-2048.
68. Guren TK, Thomsen M, Kure EH, et al. Cetuximab in treatment of metastatic colorectal cancer: final survival analyses and extended RAS data from the NORDIC-VII study. *British journal of cancer.* 2017;116(10):1271-1278.
69. Touat M, Idbaih A, Sanson M, Ligon K. Glioblastoma targeted therapy: updated approaches from recent biological insights. *Annals of Oncology.* 2017;28(7):1457-1472.
70. Bastien JI, McNeill KA, Fine HA. Molecular characterizations of glioblastoma, targeted therapy, and clinical results to date. *Cancer.* 2015;121(4):502-516.
71. Festuccia C, Biordi AL, Tombolini V, Hara A, Bailey D. Targeted molecular therapy in glioblastoma. In. Vol 2020: Hindawi; 2020.
72. An Z, Aksoy O, Zheng T, Fan Q-W, Weiss WA. Epidermal growth factor receptor and EGFRvIII in glioblastoma: signaling pathways and targeted therapies. *Oncogene.* 2018;37(12):1561-1575.
73. Gan HK, van den Bent M, Lassman AB, Reardon DA, Scott AM. Antibody–drug conjugates in glioblastoma therapy: the right drugs to the right cells. *Nature reviews Clinical oncology.* 2017;14(11):695-707.
74. Liao W, Fan S, Zheng Y, et al. Recent advances on glioblastoma multiforme and nano-drug carriers: A review. *Current Medicinal Chemistry.* 2019;26(31):5862-5874.
75. Kopylov A, Zavyalova E, Pavlova G, Pronin I. Theranostics for glioblastoma with monoclonal antibodies to the epidermal growth factor receptor. *Zhurnal Voprosy Neirokhirurgii Imeni NN Burdenko.* 2020;84(3):113-118.
76. Patel M, Vogelbaum MA, Barnett GH, Jalali R, Ahluwalia MS. Molecular targeted therapy in recurrent glioblastoma: current challenges and future directions. *Expert opinion on investigational drugs.* 2012;21(9):1247-1266.

77. McGranahan T, Therkelsen KE, Ahmad S, Nagpal S. Current state of immunotherapy for treatment of glioblastoma. *Current treatment options in oncology.* 2019;20:1-15.
78. Salinas RD, Durgin JS, O'Rourke DM. Potential of glioblastoma-targeted chimeric antigen receptor (CAR) T-cell therapy. *CNS drugs.* 2020;34(2):127-145.
79. Li L, Zhu X, Qian Y, et al. Chimeric antigen receptor T-cell therapy in glioblastoma: current and future. *Frontiers in immunology.* 2020;11:594271.
80. Chou C-J, Lin C-F, Chen Y-W, et al. The update of chimeric antigen receptor-T cells therapy in glioblastoma. *Journal of the Chinese Medical Association.* 2020;83(5):442-445.
81. Ishikawa E, Yamamoto T, Matsumura A. Prospect of immunotherapy for glioblastoma: tumor vaccine, immune checkpoint inhibitors and combination therapy. *Neurologia medico-chirurgica.* 2017;57(7):321-330.
82. Kristin Schmitz A, Sorg RV, Stoffels G, et al. Diagnostic impact of additional O-(2-[18F] fluoroethyl)-L-tyrosine (18F-FET) PET following immunotherapy with dendritic cell vaccination in glioblastoma patients. *British journal of neurosurgery.* 2021;35(6):736-742.
83. Kong Z, Wang Y, Ma W. Vaccination in the immunotherapy of glioblastoma. *Human vaccines & immunotherapeutics.* 2018;14(2):255-268.
84. Lee EX, Lam DH, Wu C, et al. Glioma gene therapy using induced pluripotent stem cell derived neural stem cells. *Molecular pharmaceutics.* 2011;8(5):1515-1524.
85. Jin H, Zhang X, Su J, Teng Y, Ren H, Yang L. RNA interference-mediated knockdown of translationally controlled tumor protein induces apoptosis, and inhibits growth and invasion in glioma cells. *Molecular Medicine Reports.* 2015;12(5):6617-6625.
86. Gao S, Tian H, Xing Z, et al. A non-viral suicide gene delivery system traversing the blood brain barrier for non-invasive glioma targeting treatment. *Journal of Controlled Release.* 2016;243:357-369.
87. Yuan Z, Zhao L, Zhang Y, et al. Inhibition of glioma growth by a GOLPH3 siRNA-loaded cationic liposomes. *Journal of Neuro-Oncology.* 2018;140:249-260.
88. Caffery B, Lee JS, Alexander-Bryant AA. Vectors for glioblastoma gene therapy: viral & non-viral delivery strategies. *Nanomaterials.* 2019;9(1):105.
89. Si Y, Zhang Y, Ngo HG, et al. Targeted liposomal chemotherapies to treat triple-negative breast cancer. *Cancers.* 2021;13(15):3749.
90. Li C, Samulski RJ. Engineering adeno-associated virus vectors for gene therapy. *Nature Reviews Genetics.* 2020;21(4):255-272.
91. Wu Z, Asokan A, Samulski RJ. Adeno-associated virus serotypes: vector toolkit for human gene therapy. *Molecular therapy.* 2006;14(3):316-327.
92. Baruteau J, Waddington S, Alexander I, Gissen P. Delivering efficient liver-directed AAV-mediated gene therapy. *Gene Therapy.* 2017;24(5):263-264.
93. Brunetti-Pierri N, Newsome PN. AAV-mediated liver-directed gene therapy for Acute Intermittent Porphyria: It is safe but is it effective? *Journal of Hepatology.* 2016;65(4):666-667.

94. Srivastava A, Lusby E, Berns KI. Nucleotide sequence and organization of the adeno-associated virus 2 genome. *Journal of virology.* 1983;45(2):555-564.
95. Samulski RJ, Chang L-S, Shenk T. A recombinant plasmid from which an infectious adeno-associated virus genome can be excised in vitro and its use to study viral replication. *Journal of virology.* 1987;61(10):3096-3101.
96. Wang D, Tai PW, Gao G. Adeno-associated virus vector as a platform for gene therapy delivery. *Nature reviews Drug discovery.* 2019;18(5):358-378.
97. Walsh CE, Liu JM, Xiao X, Young NS, Nienhuis AW, Samulski RJ. Regulated high level expression of a human gamma-globin gene introduced into erythroid cells by an adeno-associated virus vector. *Proceedings of the National Academy of Sciences.* 1992;89(15):7257-7261.
98. Grimm D, Lee JS, Wang L, et al. In vitro and in vivo gene therapy vector evolution via multispecies interbreeding and retargeting of adeno-associated viruses. *Journal of virology.* 2008;82(12):5887-5911.
99. Li W, Asokan A, Wu Z, et al. Engineering and selection of shuffled AAV genomes: a new strategy for producing targeted biological nanoparticles. *Molecular Therapy.* 2008;16(7):1252-1260.
100. Koerber JT, Jang J-H, Schaffer DV. DNA shuffling of adeno-associated virus yields functionally diverse viral progeny. *Molecular Therapy.* 2008;16(10):1703-1709.
101. Ameri H. Prospect of retinal gene therapy following commercialization of voretigene neparvovec-rzyl for retinal dystrophy mediated by RPE65 mutation. *Journal of current ophthalmology.* 2018;30(1):1.
102. Chilcott EM, Muiruri EW, Hirst TC, Yáñez-Muñoz RJ. Systematic review and meta-analysis determining the benefits of in vivo genetic therapy in spinal muscular atrophy rodent models. *Gene Therapy.* 2022;29(9):498-512.
103. Gonçalves MA. Adeno-associated virus: from defective virus to effective vector. *Virology journal.* 2005;2:1-17.
104. Sehara Y, Fujimoto K-i, Ikeguchi K, et al. Persistent expression of dopamine-synthesizing enzymes 15 years after gene transfer in a primate model of Parkinson's disease. *Human gene therapy Clinical development.* 2017;28(2):74-79.
105. Au HKE, Isalan M, Mielcarek M. Gene therapy advances: a meta-analysis of AAV usage in clinical settings. *Frontiers in medicine.* 2022;8:809118.
106. Carter BJ. Adeno-associated virus vectors in clinical trials. *Human gene therapy.* 2005;16(5):541-550.
107. Mietzsch M, Grasse S, Zurawski C, et al. OneBac: platform for scalable and high-titer production of adeno-associated virus serotype 1–12 vectors for gene therapy. *Human gene therapy.* 2014;25(3):212-222.
108. Urabe M, Nakakura T, Xin K-Q, et al. Scalable generation of high-titer recombinant adeno-associated virus type 5 in insect cells. *Journal of Virology.* 2006;80(4):1874-1885.
109. Chahal PS, Schulze E, Tran R, Montes J, Kamen AA. Production of adeno-associated virus (AAV) serotypes by transient transfection of HEK293 cell

suspension cultures for gene delivery. *Journal of virological methods.* 2014;196:163-173.
110. Clément N, Grieger JC. Manufacturing of recombinant adeno-associated viral vectors for clinical trials. *Molecular therapy Methods & clinical development.* 2016;3.
111. Blessing D, Vachey G, Pythoud C, et al. Scalable production of AAV vectors in orbitally shaken HEK293 cells. *Molecular Therapy-Methods & Clinical Development.* 2019;13:14-26.
112. Grieger JC, Soltys SM, Samulski RJ. Production of recombinant adeno-associated virus vectors using suspension HEK293 cells and continuous harvest of vector from the culture media for GMP FIX and FLT1 clinical vector. *Molecular Therapy.* 2016;24(2):287-297.
113. Zhao H, Lee K-J, Daris M, et al. Creation of a high-yield AAV vector production platform in suspension cells using a design-of-experiment approach. *Molecular Therapy Methods & Clinical Development.* 2020;18:312-320.
114. Guan J-S, Chen K, Si Y, et al. Process improvement of adeno-associated virus production. *Frontiers in chemical engineering.* 2022;4:1.
115. Ernst P, Xu N, Qu J, et al. Precisely control mitochondria with light to manipulate cell fate decision. *Biophysical journal.* 2019;117(4):631-645.
116. Chen K, Si Y, Guan J-S, et al. Targeted extracellular vesicles delivered verrucarin A to treat glioblastoma. *Biomedicines.* 2022;10(1):130.
117. Si Y, Chen K, Ngo HG, et al. Targeted EV to Deliver Chemotherapy to Treat Triple-Negative Breast Cancers. *Pharmaceutics.* 2022;14(1).
118. Si Y, Zhang Y, Guan JS, et al. Anti-CD47 Monoclonal Antibody-Drug Conjugate: A Targeted Therapy to Treat Triple-Negative Breast Cancers. *Vaccines (Basel).* 2021;9(8).
119. Si Y, Kim S, Ou J, et al. Anti-SSTR2 antibody-drug conjugate for neuroendocrine tumor therapy. *Cancer Gene Ther.* 2021;28(7-8):799-812.
120. Si Y, Guan J, Xu Y, et al. Dual-Targeted Extracellular Vesicles to Facilitate Combined Therapies for Neuroendocrine Cancer Treatment. *Pharmaceutics.* 2020;12(11).
121. Si Y, Xu Y, Guan J, et al. Anti-EGFR antibody-drug conjugate for triple-negative breast cancer therapy. *Eng Life Sci.* 2021;21(1-2):37-44.
122. Ou J, Si Y, Goh K, et al. Bioprocess development of antibody-drug conjugate production for cancer treatment. *PLoS One.* 2018;13(10):e0206246.
123. Si Y, Kim S, Zhang E, et al. Targeted Exosomes for Drug Delivery: Biomanufacturing, Surface Tagging, and Validation. *Biotechnol J.* 2020;15(1):e1900163.
124. Chen K, Si Y, Ou J, et al. Antibody-Drug Conjugate to Treat Meningiomas. *Pharmaceuticals (Basel).* 2021;14(5).
125. Stanley WC, Recchia FA, Lopaschuk GD. Myocardial substrate metabolism in the normal and failing heart. *Physiol Rev.* 2005;85(3):1093-1129.
126. Scheibye-Knudsen M, Fang EF, Croteau DL, Wilson DM, 3rd, Bohr VA. Protecting the mitochondrial powerhouse. *Trends Cell Biol.* 2015;25(3):158-170.

127. Collins Y, Chouchani ET, James AM, Menger KE, Cochemé HM, Murphy MP. Mitochondrial redox signalling at a glance. *J Cell Sci.* 2012;125(Pt 4):801-806.
128. Singh KK. Mitochondria damage checkpoint in apoptosis and genome stability. *FEMS Yeast Res.* 2004;5(2):127-132.
129. Chouchani ET, Kazak L, Jedrychowski MP, et al. Mitochondrial ROS regulate thermogenic energy expenditure and sulfenylation of UCP1. *Nature.* 2016;532(7597):112-116.
130. Antico Arciuch VG, Elguero ME, Poderoso JJ, Carreras MC. Mitochondrial regulation of cell cycle and proliferation. *Antioxid Redox Signal.* 2012;16(10):1150-1180.
131. Chen LB. Mitochondrial membrane potential in living cells. *Annu Rev Cell Biol.* 1988;4:155-181.
132. Scheid AD, Beadnell TC, Welch DR. Roles of mitochondria in the hallmarks of metastasis. *Br J Cancer.* 2021;124(1):124-135.
133. Armstrong JS. Mitochondria: a target for cancer therapy. *Br J Pharmacol.* 2006;147(3):239-248.
134. Neuzil J, Wang XF, Dong LF, Low P, Ralph SJ. Molecular mechanism of 'mitocan'-induced apoptosis in cancer cells epitomizes the multiple roles of reactive oxygen species and Bcl-2 family proteins. *FEBS Lett.* 2006;580(22):5125-5129.
135. Horobin RW, Trapp S, Weissig V. Mitochondriotropics: a review of their mode of action, and their applications for drug and DNA delivery to mammalian mitochondria. *J Control Release.* 2007;121(3):125-136.
136. Fantin VR, Leder P. Mitochondriotoxic compounds for cancer therapy. *Oncogene.* 2006;25(34):4787-4797.
137. Patra KC, Wang Q, Bhaskar PT, et al. Hexokinase 2 is required for tumor initiation and maintenance and its systemic deletion is therapeutic in mouse models of cancer. *Cancer Cell.* 2013;24(2):213-228.
138. Perini GF, Ribeiro GN, Pinto Neto JV, Campos LT, Hamerschlak N. BCL-2 as therapeutic target for hematological malignancies. *J Hematol Oncol.* 2018;11(1):65.
139. Chaiswing L, St Clair WH, St Clair DK. Redox Paradox: A Novel Approach to Therapeutics-Resistant Cancer. *Antioxid Redox Signal.* 2018;29(13):1237-1272.
140. Rohlena J, Dong LF, Ralph SJ, Neuzil J. Anticancer drugs targeting the mitochondrial electron transport chain. *Antioxid Redox Signal.* 2011;15(12):2951-2974.
141. Fulda S, Galluzzi L, Kroemer G. Targeting mitochondria for cancer therapy. *Nat Rev Drug Discov.* 2010;9(6):447-464.
142. Zhou Z, Liu Y, Song W, et al. Metabolic reprogramming mediated PD-L1 depression and hypoxia reversion to reactivate tumor therapy. *J Control Release.* 2022;352:793-812.
143. Liu Y, Zhou Z, Hou J, et al. Tumor Selective Metabolic Reprogramming as a Prospective PD-L1 Depression Strategy to Reactivate Immunotherapy. *Adv Mater.* 2022;34(41):e2206121.

144. Honda HM, Korge P, Weiss JN. Mitochondria and ischemia/reperfusion injury. *Ann N Y Acad Sci.* 2005;1047:248-258.
145. Brennan JP, Southworth R, Medina RA, Davidson SM, Duchen MR, Shattock MJ. Mitochondrial uncoupling, with low concentration FCCP, induces ROS-dependent cardioprotection independent of KATP channel activation. *Cardiovasc Res.* 2006;72(2):313-321.
146. Weisová P, Anilkumar U, Ryan C, Concannon CG, Prehn JH, Ward MW. 'Mild mitochondrial uncoupling' induced protection against neuronal excitotoxicity requires AMPK activity. *Biochim Biophys Acta.* 2012;1817(5):744-753.
147. Hausenloy DJ, Maddock HL, Baxter GF, Yellon DM. Inhibiting mitochondrial permeability transition pore opening: a new paradigm for myocardial preconditioning? *Cardiovasc Res.* 2002;55(3):534-543.
148. Solesio ME, Elustondo PA, Zakharian E, Pavlov EV. Inorganic polyphosphate (polyP) as an activator and structural component of the mitochondrial permeability transition pore. *Biochem Soc Trans.* 2016;44(1):7-12.
149. Ernst P, Xu N, Qu J, et al. Precisely Control Mitochondria with Light to Manipulate Cell Fate Decision. *Biophys J.* 2019;117(4):631-645.
150. Liu X ZL, Zhang J, Ernst P, Xu N., Inventor. Mitochondrial optogenetics-based gene therapy to treat multiple cancers. 2019.
151. Klapoetke NC, Murata Y, Kim SS, et al. Independent optical excitation of distinct neural populations. *Nat Methods.* 2014;11(3):338-346.
152. Hall MP, Unch J, Binkowski BF, et al. Engineered luciferase reporter from a deep sea shrimp utilizing a novel imidazopyrazinone substrate. *ACS Chem Biol.* 2012;7(11):1848-1857.
153. Loening AM, Dragulescu-Andrasi A, Gambhir SS. A red-shifted Renilla luciferase for transient reporter-gene expression. *Nat Methods.* 2010;7(1):5-6.
154. Tannous BA. Gaussia luciferase reporter assay for monitoring biological processes in culture and in vivo. *Nat Protoc.* 2009;4(4):582-591.
155. Graf SA, Haigh SE, Corson ED, Shirihai OS. Targeting, import, and dimerization of a mammalian mitochondrial ATP binding cassette (ABC) transporter, ABCB10 (ABC-me). *J Biol Chem.* 2004;279(41):42954-42963.
156. Hashimoto H, Mizushima T, Chijiwa T, Nakamura M, Suemizu H. Efficient production of recombinant adeno-associated viral vector, serotype DJ/8, carrying the GFP gene. *Virus Res.* 2017;238:63-68.
157. Grimm D, Lee JS, Wang L, et al. In vitro and in vivo gene therapy vector evolution via multispecies interbreeding and retargeting of adeno-associated viruses. *J Virol.* 2008;82(12):5887-5911.
158. Yin C, Zhang T, Qu X, et al. In Vivo Excision of HIV-1 Provirus by saCas9 and Multiplex Single-Guide RNAs in Animal Models. *Mol Ther.* 2017;25(5):1168-1186.
159. Bornfeldt KE, Kramer F, Batorsky A, et al. A Novel Type 2 Diabetes Mouse Model of Combined Diabetic Kidney Disease and Atherosclerosis. *Am J Pathol.* 2018;188(2):343-352.
160. Yang F, Tu J, Pan JQ, et al. Light-controlled inhibition of malignant glioma by opsin gene transfer. *Cell Death Dis.* 2013;4(10):e893.

161. Chen K, Kim S, Yang S, et al. Advanced biomanufacturing and evaluation of adeno-associated virus. *J Biol Eng.* 2024;18(1):15.